Validating dark energy models using CMB polarization due to reionization and galaxy clusters

宇宙再電離期と銀河団で生成されるCMB偏光観測を用いたダークエネルギーモデルの検証

Hiroto Kondo

近藤　寛人

A Doctor Thesis

the Graduate School of Nagoya University

on February 27th, 2023

ABSTRACT

With the recent discovery of the Accelerating Expansion of the Universe, dark energy, the unknown energy that drives cosmic expansion, has been widely accepted and its nature has been constrained by a combination of various observational methods. In the cosmic microwave background radiation (CMB), the nature of dark energy is strongly reflected to the integrated Sachs-Wolfe (ISW) effect caused by the time variation of the gravitational potential during propagation. However, the direct measurement of this effect is difficult due to the cosmic variance caused by the statistical error in estimating the variance of the initial fluctuations of the universe. Using polarized CMB photons produced by Thomson scattering by free electrons in a galaxy cluster, it is possible to obtain information of the same initial fluctuation at different times, thus constraining the dark energy model through the ISW effect without suffering from the cosmic variance. In this thesis, we propose a method that combines temperature and E-mode polarization anisotropy in CMB all-sky observations with the known method using polarization observations of clusters of galaxies. To validate the method, we calculate the temperature anisotropy and E-mode polarization anisotropy of the CMB all-sky survey and the polarization of a cluster of galaxies from the initial fluctuations in simulations, and reconstruct the initial fluctuations assuming several dark energy equation of state parameters from them. The difference between the CMB in the all-sky temperature quadrupole anisotropy estimated from the reconstructed initial fluctuations, and the quadrupole calculated in the previous step, provides the statistical power in estimating the equation of state parameters. We found from simulations that the statistical power is improved by about 18% in the case that we add the temperature and E-mode polarization anisotropies of the CMB in the all-sky observations, compared to the case that the reconstruction is performed only with polarization observations of clusters of galaxies.

Acknowledgements

First of all, I would like to express my sincere thanks to my supervisor, associate Prof. Kiyotomo Ichiki, for his great support and encouragement in research.
I am grateful to associate Prof. Hiroyuki Tashiro with many discussions in research and your daily concern.
I would thank staff members and students of the Nagoya university cosmology group.
Finally, I would like to thank my family for their great daily support.
This work was financially supported by JST SPRING, Grant Number JPMJSP2125.

Contents

Chapter 1

Introduction

1.1 Accelerated expansion and dark energy

The factor that drives the expansion of the universe was first introduced by Einstein as the cosmological constant [56]. However, since the cosmological constant was conceived to realize a static universe at that time, its existence was later withdrawn when Hubble and Lemaitre discovered the expansion of the universe [31][37].

However, as recent improvements in observational technology have made it possible to accurately measure the distance and age of the universe, observational facts that cannot be explained by a matter-dominated universe have come to attract attention. In particular, distance measurements from type Ia supernova explosions in the 1990s have conclusively shown that the current universe is undergoing accelerated expansion [53] [56][47]. As shown in Fig.1.1, recent observations of supernova explosion also fit the ΛCDM model, in which the cosmological constant is the dominant energy component today and ΛCDM model has been the standard cosmology [46].

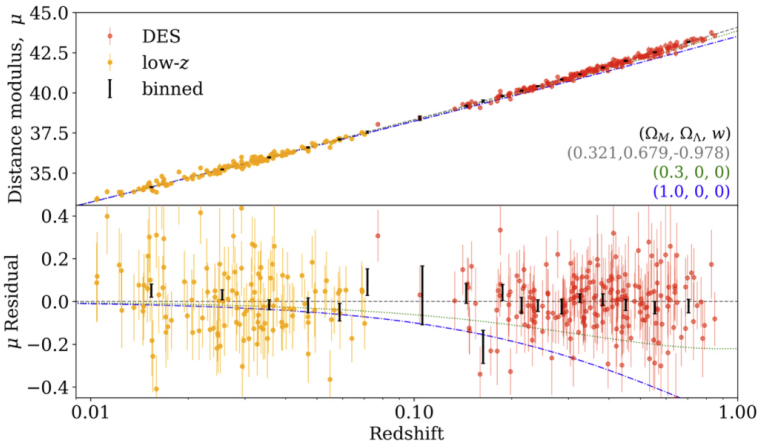

Figure 1.1: Hubble diagram for the Dark Energy Survey Supernova Program (DES-SN) sample. Top figure: distance modulus for each SN (red, orange circles). The dashed lines show models. Bottom figure: residuals to the best fit model. (figure taken from ref [2]).

The cosmological constant has the relation between energy density and pressure, $p_\Lambda = -\rho_\Lambda$, and the energy density is constant regardless of the expansion of the universe. The energy component that causes accelerated expansion must have negative pressure, and such an energy component with negative pressure is called dark energy [32]. The relationship between the energy density and pressure

of dark energy is generally expressed as $p_{\rm DE} = w\rho_{\rm DE}$ with the equation of state parameter w. As an extension, the parameterization $w(a) = w_0 + w_a(1-a)$ is also often used [39], and it varies with the expansion of the universe.

The nature of dark energy has a strong influence on the evolution of the universe and has been explored using a variety of observations, including the Cosmic Microwave Background (CMB), Type Ia Supernovae (SNIa), Baryon Acoustic Oscillations (BAO), the Weak Gravitational Lensing (WL), and Redshift-Space Distortions (RSD).

The CMB is one of the most powerful probes in cosmology. In particular, much of the information about the early universe is obtained from the CMB, which measures the curvature of the universe, the amount of matter, and photon counts with a high degree of accuracy. In addition, CMB measurements provide the most accurate measurement of the peak of the sound horizon at the time of recombination, which is also important in the measurement of matter and baryon density in the late universe. On the other hand, since the CMB is an instantaneous snapshot of recombination, it is difficult to put a direct limit on the dark energy that will be a major component in the late universe. However, in combination with other measurements at low redshifts, it also contributes to constraining the dark energy, as shown in Fig.1.2.

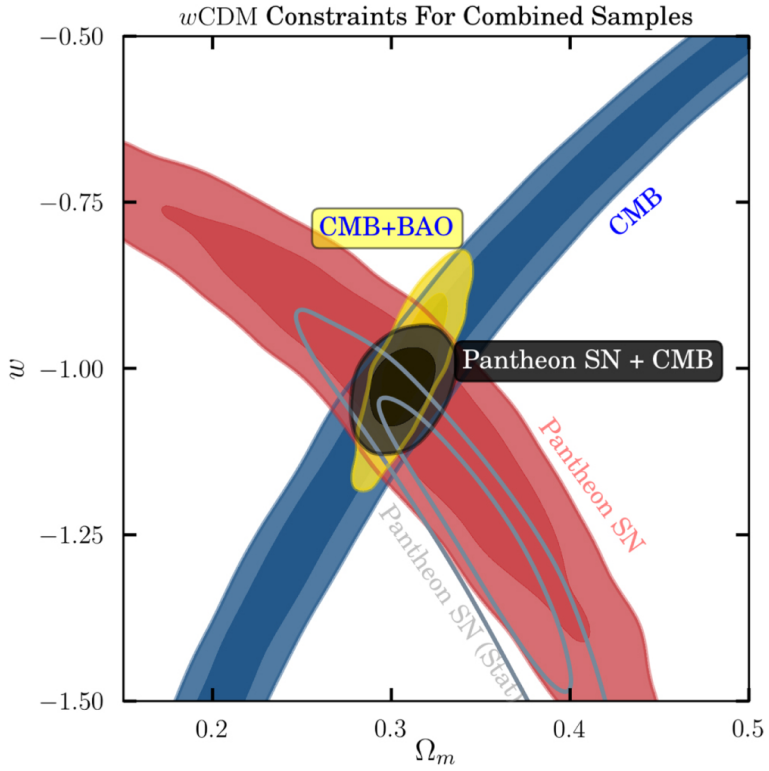

Figure 1.2: Confidence contours for matter density parameter and dark energy equation of state parameter. Each contour shows constraint from CMB (blue), Pantheon SN with systematic uncertainties (red), Pantheon SN with only statistical uncertainties (gray line), and Pantheon SN + CMB (black). (figure taken from ref [57]).

SNIa is extremely bright and can be observed far in the distance ($z > 1$), and its luminosity curve and its peaks are well known. Therefore, it can be used as a standard candle in the universe to measure luminosity distances. Since the expansion rate of the universe can be directly determined from the relationship

between the redshift and distance for each event, it is possible to constrain on dark energy equation of state parameters w based on observations of supernova explosions alone.

Acoustic oscillations of the photon-baryon fluid in the early universe have left a characteristic pattern, called the BAO scale, in the post-recombination era [20]. At low redshifts ($z < 1$), their magnitudes can be measured from galaxy correlations from large-scale galaxy surveys [24][12]. The BAO scale can also be measured at higher redshifts by using hydrogen absorption line observations.In addition, a method using 21cm hydrogen absorption line observations has been developed and is expected to provide all-sky measurements over a wide range of redshifts.

Distortion of light path due to the gravitational field distorts the observed galaxy shape, and this effect is called the gravitational lensing effect [1][27]. Spatially coherent effects produced by large-scale structures are called weak gravitational lensing (WL) effects in particular, and it is possible to obtain histories of structure growth. Since the evolution of large-scale structures is sensitive to cosmic expansion,detailed measurement within small redshift bins can strongly constrain on dark energy model, but they have difficulty with the large uncertainties.

The power spectrum in redshift space has anisotropy due to the effect of the RSD caused by the peculiar velocity of the galaxies [34][6]. As in the continuity equation, velocity can be described from the time variation of density fluctuations. Therefore, information of structure growth can be obtained from RSD, which allows us to probe the nature of dark energy.

As described above, a number of methods can be used to study the nature of the dark energy, and their combination imposes strong constraints on dark energy.

1.2 Cosmic Microwave Background Radiation(CMB)

The CMB is the emission at recombination and is the most distant electromagnetic wave we can observe. It has been observed over the entire sky and its average temperature is consistent with blackbody radiation at 2.725 K [21]. Although its temperature fluctuation is extremely small, it is an important key in cosmology, and both new observations and precise measurements down to small scales are in progress [42][30][48]. Figure 1.3 shows the temperature fluctuations observed by the Planck satellite, and its angular correlation function (power spectrum) is shown in Fig.1.4. The large dispersion at large angular scales (small l) is due to the fact that the observable region is limited on the final scattering plane and is called the cosmic variance [45]. The processes that generate such temperature fluctuations on large scales are mainly due to the Sachs-Wolfe effect (SW) and the integral Sachs-Wolfe effect (ISW) [54]. Both effects arise due to the change of energy by the gravitational potential: it gains energy as it falls into the gravitational potential and loses energy as it escapes. The SW effect arises with gravitational potential at observers and the surface of last scattering shown as Fig.1.5. The ISW effect arises because of the variation with time of the cosmic gravitational potential between observers and the surface of last scattering shown as Fig.1.6. The potential can be traced by Large Scale Structure surveys [15], and the ISW effect can be therefore a probe that links the CMB with the low redshift matter distribution.

The contributions of each effect are shown in the Fig.1.7, where the SW effect is dominant and the ISW effect is generally difficult to extract.

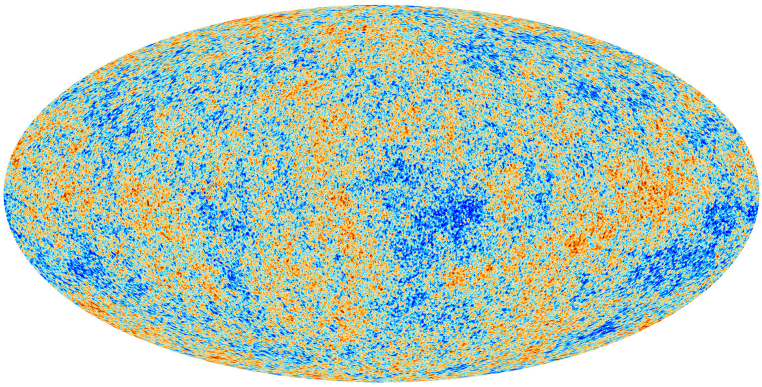

Figure 1.3: Temperature fluctuation map of cosmic microwave background radiation, observed by the Planck satellite. (figure taken from ref [49]).

.

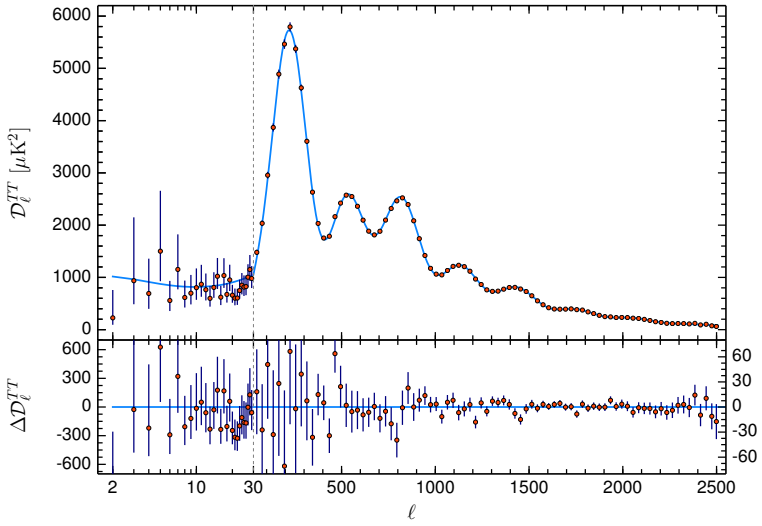

Figure 1.4: Angular correlation function of temperature fluctuation of CMB from the Planck observation. (figure taken from ref [49]).

.

In fact, the first measurement of the ISW effect using COBE data failed to detect it [9], and WMAP made it possible to detect it [10].

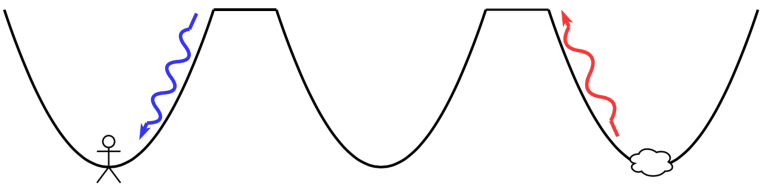

Figure 1.5: The solid black line shows the gravitational potential of the path taken by the photons emitted from the last scattering surface. The blue arrows represent falling to the gravitational potential, and the red arrows represent escaping from the gravitational potential.

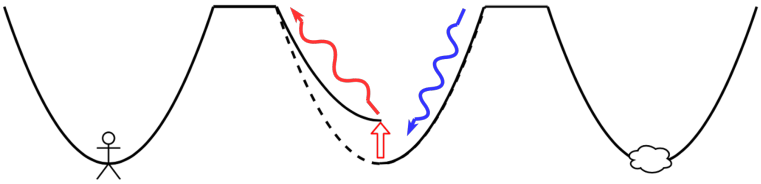

Figure 1.6: Rough sketch of ISW effect. The solid black line shows the gravitational potential of the path taken by the photons emitted from the last scattering surface. The step is the change in gravitational potential during the photon's passage. The blue arrows represent falling to the gravitational potential, and the red arrows represent escaping from the gravitational potential.

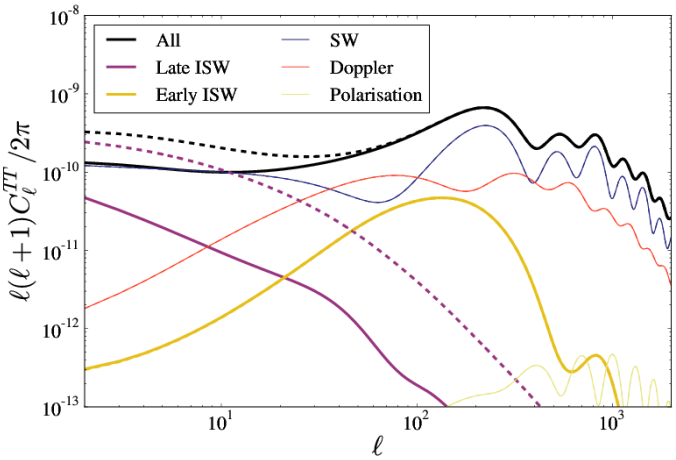

Figure 1.7: The single contributions to the CMB temperature spectrum. The solid line indicates the lCDM model. The solid black line is the sum of all effects, the solid blue line represents the SW effect, the solid yellow line the early ISW effect, and the solid purple line the late ISW effect (figure taken from ref [5]).

.

1.3 Cosmic mirror

If we can place a mirror in space, we can observe the same point at different times. We can apply this to the CMB and use scattering from galaxy clusters instead of mirrors to reduce the cosmic variance [35]. This is based on the phenomenon that when light of different intensity is incident perpendicularly on the scattering target, as shown in Fig.1.8, Thomson scattering produces linear polarization in the reflected light [55]. However, the information obtained by this method is limited to the inside of our optical cone and is correlated with each other, so it's not enough improvement to resolve cosmic variance [50][11]. On the other hand, multiple observations of the same initial fluctuation at different epochs can be used to fix the SW effect and to obtain information on the integral Sachs-Wolfe effect at each redshift. The information on the ISW effect can be retrieved for each redshift, and the method of restricting the equation of state parameters for the dark energy is verified using simulations [33][59]. This simulation reconstructs the fluctuations at the recombination epoch by using the CMB polarization of many clusters of galaxies, and evaluates the reconstruction of the fluctuations through the quadrupole temperature fluctuations that we directly observe. As shown in Fig.1.9, the polarization of a galaxy cluster reflects infor-

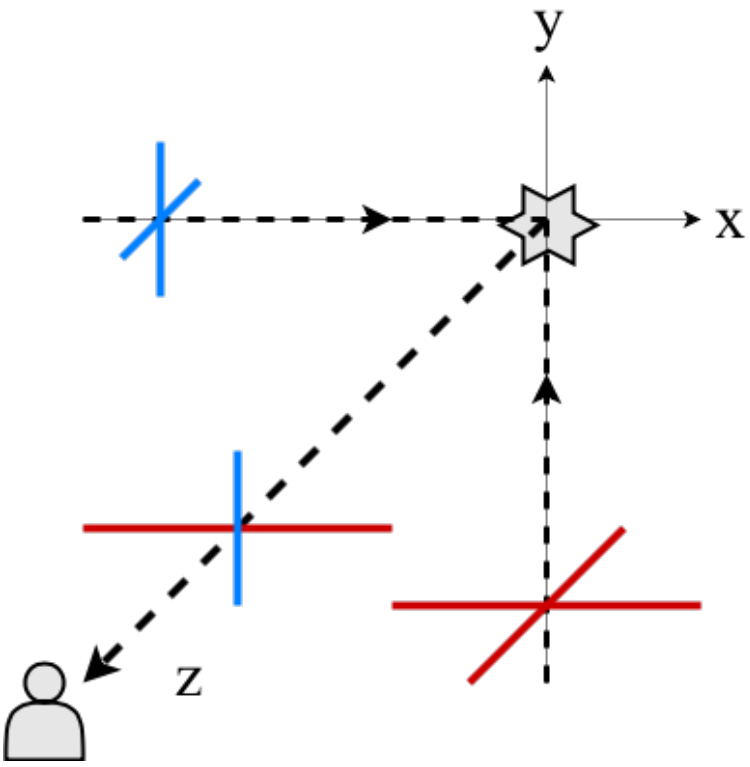

Figure 1.8: The process of producing linearly polarized light in a galaxy cluster. A red cross represents strong intensity and a blue cross weak intensity. The observer measures the ratio as the polarization intensity.

mation from a smaller last scattering surface than our last scattering surface, and that region creates a lot of overlap given the large number of clusters.

1.4 Aim and structure of the thesis

Since the ISW effect is caused by changes in the gravitational potential along the path of propagating CMB photons, the effect is enhanced by accelerated expansion. Typical measurements of the ISW effect cannot effectively constrain the dark energy model very much because the ISW effect is small compared to the cosmic variance from the variance of the initial fluctuations at recombination so called the SW effect. However, by using the linear CMB polarization generated by clusters of galaxies due to the past CMB quadrupoles, it is possible to obtain information on the quadrupoles at different times with the same initial fluctuations. In [33], a method is proposed to predict the quadrupole of the CMB that we directly observe from the quadrupole of galaxy clusters and to constrain the dark energy model by comparison with actual observations. Such distant quadrupoles also correlate with polarization anisotropy and other temperature anisotropies than the quadrupoles in our direct all-sky observations. Therefore, in this thesis, we propose a new method of constraining the dark energy model using the polarization of galaxy clusters, combining polarization and temperature anisotropy from all-sky observations of the CMB, and test the improvement of constraints on the dark energy model using simulations by this method.

The thesis is structured as follows. In Chapter 2 I introduce the foundations of standard cosmology. In chapter 3 I describe the temperature anisotropy of the CMB in clusters of galaxies, and after that I explain the process of polarization

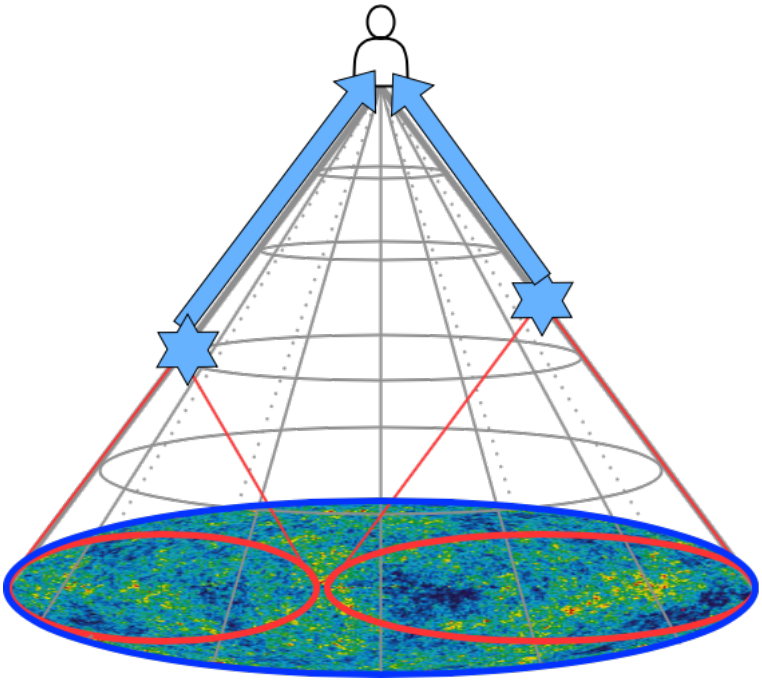

Figure 1.9: Rough sketch of the simulation. This figure shows the light corn of the observer. The bottom panel represents the temperature fluctuations at the last scattering time. The star-shaped objects represent galaxy clusters, and the CMB that each sees is represented by a red circle.

production in clusters of galaxies. In chapter 4 I introduce the simulations for validation and show the results obtained. In addition I discuss the reconstruction of the initial fluctuations in the validation process. Finally, I summarize my thesis in Chapter 5.

Chapter 2

Standard cosmology

In this thesis, we adopt a natural unit system with the following physical constants.

$$c = \hbar = k_{\rm B} = 1 \tag{2.1}$$

The following notation is used in this thesis.
Here $\vec{x}$ represents the coordinates in any inertial system, and each component is represented as follows, 0 represents time and 1,2,3 represents spatial components. For example, in Cartesian coordinates

$$x^0 = t,\ x^1 = x,\ x^2 = y,\ x^3 = z \tag{2.2}$$

The Roman letters $i, j, ...$ in the subscripts represent three-dimensional spatial components, and the Greek letters $\mu, \nu, ...$ represent time and spatial components. An over-dot indicates a derivative by proper time, and a prime maker indicates a derivative by conformal time.

$$\frac{dX}{dt} \equiv \dot{X}, \qquad \frac{dX}{d\tau} \equiv X' \tag{2.3}$$

In derivatives that include spatial components, partial derivatives and covariate derivatives are denoted by commas and semicolons, respectively. In addition, the covariate derivative of the spatial component only is indicated by a vertical bar.

$$A^{\mu}{}_{\nu,\lambda} \equiv \partial_\lambda A^{\mu}{}_{\nu} = \frac{\partial A^{\mu}{}_{\nu}}{\partial x^\lambda} \tag{2.4}$$

$$A^{\mu}{}_{\nu;\lambda} \equiv \nabla_\lambda A^{\mu}{}_{\nu} = \partial_\lambda A^{\mu}{}_{\nu} + \Gamma^{\mu}_{\lambda\alpha} A^{\alpha}{}_{\nu} - \Gamma^{\alpha}_{\lambda\nu} A^{\mu}{}_{\alpha} \tag{2.5}$$

$$B_{i|j} \equiv {}^{(3)}\nabla_j B_i \tag{2.6}$$

The symmetrized and symmetrized tensors for sign reversal from a second-order tensor $C^{\mu\nu}$ are written as follows.

$$C^{(\mu\nu)} = \frac{1}{2}(C^{\mu\nu} + C^{\nu\mu}), \qquad C^{[\mu\nu]} = \frac{1}{2}(C^{\mu\nu} - C^{\nu\mu}) \tag{2.7}$$

2.1 Friedmann-Robertson-Walker metric

Modern cosmology is built on a concept called the cosmological principle. Take inertial systems that can observe the universe isotropically in multiple spatial coordinates. In this case, each inertial system is static each other. The proper time synchronized in any coordinates is defined as cosmic time. Then, the same universe is observed in each coordinate at the same proper time. Under these conditions, we can establish spatial coordinates that do not change with the expansion of the universe, called co-moving coordinates. By adding cosmic time to the space coordinate, it is defined as a four-dimensional coordinate, and its line element is shown as

$$ds^2 = g_{\mu\nu}dx^\mu dx^\nu = g_{00}dt^2 + 2cg_{0i}dtdx^i + g_{ij}dx^i dx^j \tag{2.8}$$

In the spatially static case, the spatial component is zero $dx^i = 0$. Then by the definition of line elements, the time component $g_0 0$ is -1. In order to observe the universe isotropically, the metric has no special direction $g_{0i} = g_{i0} = 0$.

$$ds^2 = -dt^2 + g_{ij}dx^i dx^j \tag{2.9}$$

Denote by γ_{ij} the metric of three-dimensional space at any given time t_0 in a given spatial coordinate $\vec{x}$.

$$\gamma_{ij}(\vec{x}) = g_{ij}(t_0, \vec{x}) \tag{2.10}$$

The distance between two points separated by a microscopic distance dx^i is

$$dl(t_0) = \sqrt{\gamma_{ij}dx^i dx^j} \tag{2.11}$$

Consider equal expansion or shrinkage in all coordinates in space, depending on time. Therefore, the change in the micro vector can be expressed as a time only function $a(t)$. The distance dl at a general time t is

$$dl(t) = \sqrt{\gamma_{ij}a(t)dx^i a(t)dx^j} = a(t)dl(t_0) \tag{2.12}$$

The proportionality constant $a(t)$ that represents the degree of expansion or shrinkage of the universe is called the scale factor. Normalizing so that $a(t_0)dl(t_0) = dl(t_0)$ when $t = t_0$, we obtain

$$a(t_0) = 1 \tag{2.13}$$

In the following, the time t_0 is taken as the current time, and the current scale factor is set to 1.
In order to obtain the actual form of the metric γ_{ij}, we introduce a two-dimensional plane on a sphere in polar coordinate form. First, we take the radial coordinate $\vec{r}$ so that the area of the two-dimensional sphere at a constant distance from the origin is $4\pi r^2$. In this case, the line element is given by $r^2(d\theta^2 + \sin^2\theta d\phi^2)$. Since the radial direction is orthogonal to the line element on the sphere, the line element in 3-dimensional space can be defined by adding the radial component.

$$\gamma_{ij}dx^i dx^j = F(r)dr^2 + r^2(d\theta^2 + \sin^2\theta d\phi^2) \tag{2.14}$$

Christoffel symbol showing space distortion from the metric is

$$\Gamma^\mu{}_{\lambda\nu} = \frac{1}{2}g^{\mu\rho}\left(\partial_\nu g_{\rho\lambda} + \partial_\lambda g_{\rho\nu} - \partial_\rho g_{\lambda\nu}\right) \tag{2.15}$$

In addition, the curvature tensor is

$$R^{\mu}{}_{\nu\alpha\beta} = \partial_{\alpha}\Gamma^{\mu}{}_{\beta\nu} - \partial_{\beta}\Gamma^{\mu}{}_{\alpha\nu} + \Gamma^{\mu}{}_{\alpha\lambda}\Gamma^{\lambda}{}_{\beta\nu} - \Gamma^{\mu}{}_{\beta\lambda}\Gamma^{\lambda}{}_{\alpha\nu} \tag{2.16}$$

Its summation is the Ricci tensor $R_{\mu\nu}$.

$$R_{\mu\nu} = R^{\lambda}{}_{\mu\lambda\nu} \tag{2.17}$$

A further summation yields the scalar curvature R.

$$R = R^{\mu}{}_{\mu} \tag{2.18}$$

Calculating the three-dimensional scalar curvature $R^{i}{}_{i}$ from the metric in Eq.(2.14)

$${}^{(3)}R = \frac{2}{r^2}\frac{d}{dr}\left[r\left(1 - \frac{1}{F}\right)\right] \tag{2.19}$$

As the space is uniform, ${}^{(3)}R$ is independent of the spatial coordinates. Using the constant K and setting ${}^{(3)}R = 6K$, the metric of space is

$$\gamma_{ij}dx^{i}dx^{j} = \frac{1}{1 - Kr^2}dr^2 + r^2(d\theta^2 + \sin^2\theta d\phi^2) \tag{2.20}$$

Taken together, it is called Friedmann-Robertson-Walker metric (FRW metric), a general metric for a homogeneous and isotropic universe.

$$ds^2 = -dt^2 + a^2(t)\left[\frac{dr^2}{1 - Kr^2} + r^2\left(d\theta^2 + \sin^2\theta d\phi^2\right)\right] \tag{2.21}$$

It has two degrees of freedom: a scale factor$a(t)$ representing the expansion or contraction of the universe due to time variation and the curvature of space$K$. Now consider matching the radial coordinates with the physical distance. The geodesic micro distance on radial direction dx from the FRW metric of Eq.(2.21) is

$$dx = \frac{dr}{\sqrt{1 - Kr^2}} \tag{2.22}$$

Integrating this in the radial direction yields the geodesic distance. The integrated function is summarized as $S_K(x)$, since it varies with the sign of the curvature K.

$$r = S_K(x) \tag{2.23}$$

$$S_K(x) = \begin{cases} \dfrac{\sinh\left(\sqrt{-K}x\right)}{\sqrt{-K}} & (K < 0) \\ x & (K = 0) \\ \dfrac{\sin(\sqrt{K}x)}{\sqrt{K}} & (K > 0) \end{cases} \tag{2.24}$$

Using x-coordinate as a radial coordinate, FRW metric becomes

$$ds^2 = -dt^2 + a^2(t)\left[dx^2 + S_K^2(x)\left(d\theta^2 + \sin^2\theta d\phi^2\right)\right] \tag{2.25}$$

The distance x used here is equal to the physical distance from the origin at the current time $a(t_0) = 1$. Also, the distance x does not have time-dependence,

but the physical distance changes with the expansion and contraction of the universe. Therefore, the physical distance from the origin to the coordinate x at any given time is $a(t)x$ multiplied by a scale factor. Such coordinates independent of the expansion and contraction of the universe are called co-moving coordinates, and the distance x defined in a time-independent format is called the co-moving distance.
In addition, consider a metric in which the time component, like the space, varies with the scale factor$a(t)$.

$$ds^2 = -a^2(t)d\tau^2 + a^2(t)\left[dx^2 + S_K^2(x)\left(d\theta^2 + \sin^2\theta d\phi^2\right)\right] \tag{2.26}$$

Then, the new time component τ is called conformal time and represented with using the proper time t

$$\tau = \int_0^t \frac{dt'}{a(t')} \tag{2.27}$$

In summary, the FRW metric is represented

$$ds^2 = a^2(\tau)\left[-d\tau^2 + dx^2 + S_K^2(x)\left(d\theta^2 + \sin^2\theta d\phi^2\right)\right] \tag{2.28}$$

Light from distant objects is affected by the expansion of the universe as it propagates to the observer. If the cosmic expansion is uniform, the physical distance between the observer and the object is elongated in proportion to the co-moving distance. Therefore, the spectrum of light emitted from astronomical objects is also shifted toward longer wavelengths, which is called redshift.
Consider that the object to be observed in FRW metric Eq.(2.25) emits light from position (x_1, θ_1, ϕ_1) at time t_1, and the observer observes at time t_0 at the origin $x = 0$. The light ray travels along the null geodesic $ds = 0$. Also, since space is isotropic, $d\theta = d\phi = 0$ for a geodesic connecting the origin and a celestial body. Therefore, the time on the ray and the minute distance in the radial direction are

$$dt = -a(t)dx \tag{2.29}$$

Integrating this yields

$$\int_{t_1}^{t_0} \frac{dt}{a(t)} = x_1 \tag{2.30}$$

he x_1 is the co-moving distance between the observer and the object, so it does not change with time. Consider light propagating as a wave: the first wave peak starts at time t_1 and the second peak starts at time $t_1 + \delta t_1$. Let t_0 be the time when the first peak reaches the observer at the origin, and $t_0 + \delta t_0$ be the time when the next peak arrives. Since the propagating co-moving distance x_1 is constant,

$$\int_{t_1}^{t_0} \frac{dt}{a(t)} = \int_{t_1+\delta t_1}^{t_0+\delta t_0} \frac{dt}{a(t)} = x_1 \tag{2.31}$$

The wave period $\delta t_0, \delta t_1$ is sufficiently short compared to the time-varying scale of the scale factor, so the Taylor expansion

$$\frac{\delta t_1}{a(t_1)} = \frac{\delta t_0}{a(t_0)} \tag{2.32}$$

By multiplying δt_0, δt_1 by the speed of light c, we can obtain each wavelength.

$$\lambda_0 = c\delta t_0, \qquad \lambda_1 = c\delta t_1 \tag{2.33}$$

Redshift is defined as the change in wavelength during emission and observation.

$$z \equiv \frac{\lambda_0 - \lambda_1}{\lambda_1} \tag{2.34}$$

From Eq.(2.32) and Eq.(2.34), the relationship between redshift and scale factor is derived.

$$1 + z = \frac{\lambda_0}{\lambda_1} = \frac{a(t_0)}{a(t_1)} \tag{2.35}$$

From the normalization of $a(t_0) = 1$, when the observed time is taken to be the present

$$1 + z = \frac{1}{a(t_1)} \tag{2.36}$$

In the expanding universe, the scale factor $a(t)$ is a monotonically increasing function of time, and the scale factor $a(t)$ and redshift $z(t)$ correspond one-to-one to time t. This means that the co-moving coordinate x can be described not only as an integral of the cosmological time t, as in Eq.(2.30), but also as an integral of the scale factor a and redshift z.

$$x = \int_t^{t_0} \frac{dt}{a} = \int_a^1 \frac{cda}{a^2 H} = \int_0^z \frac{cdz}{H} \tag{2.37}$$

The $H(t)$ used here is a function of time t, the expansion rate of the universe, and is called the Hubble parameter.

$$H(t) \equiv \frac{\dot{a}(t)}{a(t)} \tag{2.38}$$

hus, the cosmological redshift caused by the effect of cosmic expansion can be calculated. However, in the actual universe, objects such as galaxy has proper motion in random directions. Therefore, in addition to the cosmological redshift, the Doppler effect also produces redshifts. Therefore, it is impossible to determine the complete cosmological redshift of a galaxy, and thus its distance to the galaxy, from the measurement of the redshift.
Here γ_{ij} is a time-independent uniformly isotropic 3-dimensional space metric given by Eq.(2.20), and the 4-dimensional space-time metric $g_{\mu\nu}$ and its inverse $g^{\mu\nu}$ are divided into time and space components.

$$ds^2 = -dt^2 + a^2(t)\gamma_{ij}dx^i dx^j \tag{2.39}$$

$$g_{00} = -1, \qquad g_{0i} = g_{i0} = 0, \qquad g_{ij} = a^2\gamma_{ij} \tag{2.40}$$

$$g^{00} = -1, \qquad g^{0i} = g^{i0} = 0, \qquad g_{ij} = \frac{1}{a^2}\gamma^{ij} \tag{2.41}$$

The Christoffel symbol is obtained from Eq.(2.40) and Eq.(2.41) with three-dimensional metric γ_{ij}, γ^{ij}.

$$\begin{aligned}
&\Gamma^0{}_{00} = \Gamma^0{}_{0i} = \Gamma^0{}_{i0} = \Gamma^i{}_{00} = 0 \\
&\Gamma^0{}_{ij} = \frac{a\dot{a}}{c}\gamma_{ij}, \qquad \Gamma^i{}_{0j} = \Gamma^i{}_{j0} = \frac{\dot{a}}{ca}\delta^i{}_j \\
&{}^{(3)}\Gamma^i{}_{jk} \equiv \Gamma^i{}_{jk} = \frac{1}{2}\gamma^{il}(\gamma_{lk,j} + \gamma_{jl,k} - \gamma_{jk,l})
\end{aligned} \tag{2.42}$$

Then, we obtain the three-dimensional curvature tensor ${}^{(3)}R_{ijkl}$.

$${}^{(3)}R_{ijkl} = (\gamma_{ik}\gamma_{jl} - \gamma_{il}\gamma_{jk}) \tag{2.43}$$

The curvature tensor, including a time component, is

$$\begin{aligned}
&R^0{}_{00i} = R^0{}_{0ij} = R^0{}_{ijk} = R^i{}_{0jk} = R^i{}_{j0k} = 0 \\
&R^0{}_{i0j} = a\ddot{a}\gamma_{ij}, \qquad R^i{}_{00j} = \frac{\ddot{a}}{a}\delta^i{}_j \\
&R^i{}_{jkl} = \left(\dot{a}^2 + K\right)(\delta^i{}_k\gamma_{jl} - \delta^i{}_l\gamma_{jk})
\end{aligned} \tag{2.44}$$

From this, Rich Tensor is

$$\begin{aligned}
&R^0{}_0 = \frac{3\ddot{a}}{a} \\
&R^i{}_0 = R^0{}_i = 0 \\
&R^i{}_j = \left[\frac{\ddot{a}}{a} + 2\left(\frac{\dot{a}}{a}\right)^2 + \frac{2}{a^2}K\right]\delta^i{}_j
\end{aligned} \tag{2.45}$$

Further contraction yields a scalar curvature of

$$R = 6\left[\frac{\ddot{a}}{a} + \left(\frac{\dot{a}}{a}\right)^2 + \frac{1}{a^2}K\right] \tag{2.46}$$

2.2 Einstein's equations and Friedmann equation

In Newtonian mechanics, where matter does not bend space-time, the Poisson equation $\Delta\phi = 4\pi G\rho$ exists as the equation describing the gravitational field. It links the gravitational potential ϕ to the mass density ρ. The Einstein equation, which is an extension of this equation, is the most important basic formula that gives the relationship between matter, energy, and gravity in the general theory of relativity.

$$G^\mu{}_\nu = \frac{8\pi G}{}T^\mu{}_\nu \tag{2.47}$$

where $T^\mu{}_\nu$ is the energy-momentum tensor. Also, $G^\mu{}_\nu$ on the left side is described by the Ricci tensor, scalar curvature, and metric $g^\mu{}_\nu$.

$$G^\mu{}_\nu \equiv R^\mu{}_\nu - \frac{1}{2}g^\mu{}_\nu R \tag{2.48}$$

This is the Einstein tensor. With using Eq.(2.45) and Eq.(2.46)

$$\begin{aligned} G^0{}_0 &= -3\left[\left(\frac{\dot{a}}{a}\right)^2 + \frac{K}{a^2}\right] \\ G^i{}_0 &= G^0{}_i = 0 \\ G^i{}_j &= -\frac{1}{c}\left[2\frac{\ddot{a}}{a} + \left(\frac{\dot{a}}{a}\right)^2 + \frac{K}{a^2}\right]\delta^i{}_j \end{aligned} \tag{2.49}$$

Due to the isotropy of space, the spatial component of the Einstein tensor also has no off-diagonal component from $\delta^i{}_j$. The Bianchi identity for the curvature tensor is

$$R^\lambda{}_{\mu\nu\rho;\sigma} + R^\lambda{}_{\mu\sigma\nu;\rho} + R^\lambda{}_{\mu\rho\sigma;\nu} = 0 \tag{2.50}$$

From here, the energy-momentum tensor satisfies the energy-momentum conservation law as follows.

$$T^\mu{}_{\nu,\mu} = 0 \tag{2.51}$$

Comparing the Einstein equation in Eq.(2.47) with the Einstein tensor in Eq.(2.49), the energy-momentum tensor T^μ_ν is determined as

$$(T^\mu{}_\nu) = \begin{pmatrix} -\rho & 0 & 0 & 0 \\ 0 & p & 0 & 0 \\ 0 & 0 & p & 0 \\ 0 & 0 & 0 & p \end{pmatrix} \tag{2.52}$$

The ρ and p correspond to the energy density and pressure, respectively. These energy densities and pressure are allowed to change only in time due to the uniform isotropy of the universe. Two equations are obtained from the diagonal components of Einstein's equations for uniformly isotropic spacetime.

$$\left(\frac{\dot{a}}{a}\right)^2 = \frac{8\pi G}{3}\rho - \frac{K}{a^2} \tag{2.53}$$

$$\frac{\ddot{a}}{a} = -\frac{4\pi G}{3}(\rho + 3p) \tag{2.54}$$

These are called the Friedman equations, which describe the expansion and contraction of the universe in terms of its components, such as energy density and pressure, and curvature. Also, from Eq.(2.53) and Eq.(2.54)

$$\dot{\rho} + 3\frac{\dot{a}}{a}(\rho + p) = 0 \tag{2.55}$$

This equation represents energy conservation.

2.3 Cosmological constant and dark energy

Looking at Eq.(2.54), the second-order derivative of the scale factor $\ddot{a}$, which is the acceleration of the expansion rate of the universe, is determined by the energy density ρ and pressure p. For ordinary matter, both the energy density and pressure are positive, so according to Eq.(2.54), the expansion rate of the universe is always negative. This is due to the fact that gravity works as an attractive force between matter, an effect that contracts space-time. In such a universe, the cosmic expansion always continues to decelerate and eventually begins to shrink. In order to realize a stationary universe in which the scale factor a is a constant independent of time, Einstein modified the Einstein equation by adding the cosmological term $\Lambda\delta^{\mu}_{\ \nu}$ to Einstein's equation Eq.(2.47).

$$G^{\mu}_{\ \nu} + \Lambda\delta^{\mu}_{\ \nu} = 8\pi G T^{\mu}_{\ \nu} \tag{2.56}$$

The Λ introduced here is a constant and is called the cosmological constant. Since the cosmological term is a constant, the conservation law of energy and momentum in Eq.(2.55) remains unchanged. On the other hand, Eq.(2.53) and Eq.(2.54), which include the Friedman equation, can be rewritten to include the cosmological constant Λ.

$$\left(\frac{\dot{a}}{a}\right)^2 = \frac{8\pi G}{3}\rho - \frac{K}{a^2} + \frac{\Lambda}{3} \tag{2.57}$$

$$\frac{\ddot{a}}{a} = -\frac{4\pi G}{3}(\rho + 3p) + \frac{\Lambda}{3} \tag{2.58}$$

When the cosmological constant Λ is positive, it behaves as if it is driving the expansion of the universe, and a stationary universe can be realized by tuning it together with the curvature K. However, the stationary universe is theoretically unstable. In recent years, Perlmutter, Schmidt, and Ries have discovered that the present universe is accelerating expansion based on observations of distant Type 1a supernova explosions. The cosmological term is widely accepted because the accelerated expansion of the universe, $\dot{a} > 0$, can be explained by a cosmological term more positive than Eq.(2.58). Consider the existence of the cosmological term as some kind of energy component. Matching the form to the energy density and pressure of Eq.(2.57) and Eq.(2.58), we obtain

$$\rho_\Lambda = \frac{\Lambda}{8\pi G}, \qquad p_\Lambda = -\frac{\Lambda}{8\pi G} \tag{2.59}$$

The equation of state linking the pressure and energy in the cosmological term is

$$p_\Lambda = -\rho_\Lambda \tag{2.60}$$

Unlike ordinary matter, the energy density exerts a negative pressure, indicating that it is also driving cosmic expansion.
However, the necessary condition for explaining the accelerating expansion of the cosmological term is Eq.(2.58), which means that the energy density and pressure do not necessarily have to be constants, since $\rho + 3p < 0$ from Eq.(2.58). Therefore, all unknown energy components that cause the accelerated expansion of the universe are generally referred to as dark energy. Since dark energy can be included in the energy density ρ and pressure p by considering it as an energy

component, Eq.(2.57) and Eq.(2.58) can be returned to the form of Eq.(2.53) and Eq.(2.54). The contribution of dark energy to cosmic expansion can also be calculated once the relationship between energy density and pressure is determined. The energy density ρ_{DE} and pressure p_{DE} of dark energy are

$$p_{\mathrm{DE}} = w_{\mathrm{DE}}\rho_{\mathrm{DE}} \tag{2.61}$$

2.4 Cosmological parameters

Parameters that cannot be determined solely from the theoretical structure and must be determined by observation in solving the evolution of the universe as a whole are called cosmological parameters. Here, we define the parameters for a uniformly isotropic universe. The expansion rate of the universe is defined as the Hubble parameter as a function of each time t in Eq.(2.38). As the expansion rate at the current time t_0, the Hubble constant is

$$H_0 = \left.\frac{\dot{a}}{a}\right|_{t=t_0} \tag{2.62}$$

The subscript 0 indicates the value at the current time t_0. Generally, current Hubble constant divided by 100 is also expressed using the lowercase letter h.

$$h \equiv \frac{H_0}{100} \tag{2.63}$$

With the Hubble constant, the Friedman equation becomes

$$H_0^2 = \frac{8\pi G}{3}\rho_0 - K \tag{2.64}$$

where ρ_0 is the current total energy density. Dark energy is also included as well as the radiative and material components.

$$\rho_0 = \sum_A \rho_{A0} \tag{2.65}$$

As can be seen from Eq.(2.64), the Hubble constant is a cosmological parameter because it is given by the curvature and the current energy density. In the flat universe model with zero curvature $K = 0$, the current total energy density from Eq.(2.64) is

$$\rho_{c0} = \frac{3H_0^2}{8\pi G} \tag{2.66}$$

This energy density at zero curvature ρ_{c0} is called the critical energy density. If this is converted to a mass density,

$$\varrho_{c0} \equiv \rho_{c0} = \frac{3H_0^2}{8\pi G} \tag{2.67}$$

The ϱ_{c0} is called the critical mass density and is a cosmological parameter determined together with the Hubble constant. The dimensionless quantity that normalizes the current energy density of each component by the critical energy density is called the density parameter. The density parameter for component A is

$$\Omega_{A0} = \frac{\rho_{A0}}{\rho_{c0}} = \frac{8\pi G\rho_{A0}}{3H_0^2} \tag{2.68}$$

The total energy density is given by the addition of all components.

$$\Omega_0 = \frac{\rho_0}{\rho_{c0}} = \frac{8\pi G\rho_0}{3H_0^2} = \sum_A \Omega_{A0} \tag{2.69}$$

The density parameter of the cosmological term, a kind of the dark energy, is from Eq.(2.59)

$$\Omega_{d0} = \frac{\rho_\Lambda}{\rho_{c0}} = \frac{\Lambda}{3H_0^2} \tag{2.70}$$

The energy density of the cosmological constant ρ_Λ is a constant value that does not change with time. With the density parameter, the Friedman equation can be written in terms of the curvature K with the density parameter

$$\frac{K}{H_0^2} = \Omega_0 - 1 \tag{2.71}$$

The sign of $\Omega_0 - 1$ and the sign of the curvature K coincide, which means that the space has positive curvature when the total density of the universe is larger than the critical density and negative curvature when it is smaller. To remain the universe being flat, the sum of matter, radiation and dark energy must equal the critical density. The curvature parameter is obtained by non-dimensionalizing the curvature from the table expression in Eq.(2.71).

$$\Omega_{K0} = -\frac{K}{H_0} \tag{2.72}$$

By introducing a curvature parameter, Eq.(2.71) The density parameter can be rewritten to add up to 1.

$$\Omega_0 + \Omega_{K0} = \sum_A \Omega_{A0} + \Omega_{K0} = 1 \tag{2.73}$$

The density parameter is defined from the density of each component at the current time. This is due to the fact that the density parameter is a cosmological parameter determined by observation. However, in general, most of the cosmological parameters are scale factor dependent, and time variation must be taken into account when considering a sufficiently distant, high-redshift universe. The time-dependent cosmological parameters are defined as follows.

$$H = \frac{\dot{a}}{a}, \qquad \rho_c = \frac{3H^2}{8\pi G} \tag{2.74}$$

$$\Omega_A = \frac{\rho_A}{\rho_c} = \frac{8\pi G\rho_A}{3H^2}, \qquad \Omega_K = -\frac{K}{a^2H^2} \tag{2.75}$$

Writing Eq.(2.73) also in a time-dependent form

$$\Omega \equiv \sum_A \Omega_A = 1 - \Omega_K \tag{2.76}$$

Time-dependent cosmology expressed in terms of current cosmological parameters

$$\Omega_A = \frac{H_0^2}{H^2}\frac{\rho_A\Omega_{A0}}{\rho_{A0}}, \qquad \Omega_K = \frac{H_0^2}{H^2}\frac{\Omega_{K0}}{a^2} \tag{2.77}$$

With these, we rewrite Eq.(2.76) to obtain an expression for the Friedman equation with density parameters.

$$\frac{H^2}{H_0^2} = \sum_A \frac{\rho_A \Omega_{A0}}{\rho_{A0}} + \frac{\Omega_{K0}}{a^2} \tag{2.78}$$

From these equations, the time-dependent density parameter is expressed as

$$\Omega_A = \frac{\rho_A \Omega_{A0}/\rho_{A0}}{\sum_B \rho_B \Omega_{B0}/\rho_{B0} + \Omega_{K0}/a^2}, \qquad \Omega_K = \frac{\Omega_{K0}/a^2}{\sum_B \rho_B \Omega_{B0}/\rho_{B0} + \Omega_{K0}/a^2} \tag{2.79}$$

From these, given the time variation ρ_A/ρ_{A0} by the scale factor of each component, the variation of the ratio of each component to the critical density can be calculated as shown in Fig.2.1.

$$(\Omega_r, \Omega_m, \Omega_d) = \frac{\left(\Omega_{r0}, \Omega_{m0} a, \Omega_{d0} a^4\right)}{\Omega_{r0} + \Omega_{m0} a + \Omega_{d0} a^4} \tag{2.80}$$

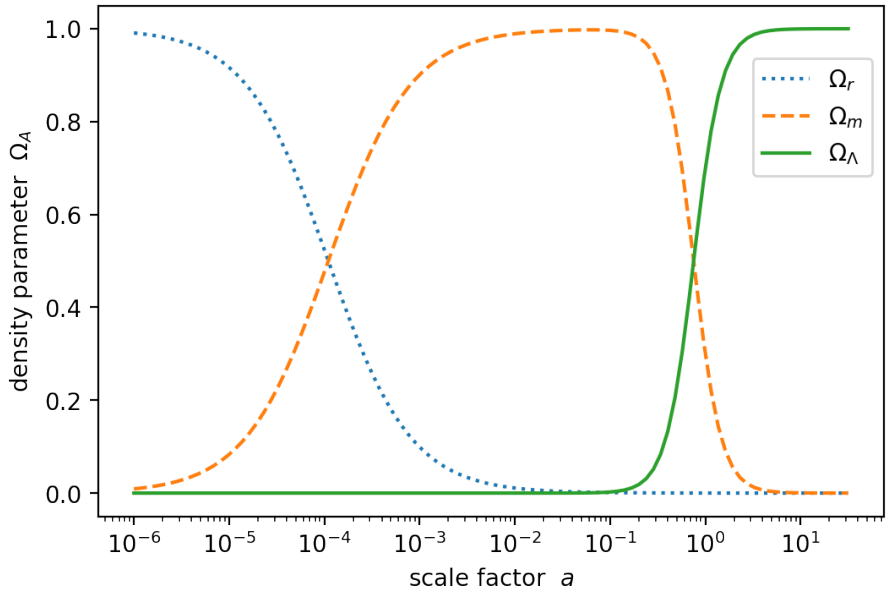

Figure 2.1: Evolution of each energy component along scale factor. The dotted line shows the radiative component, the dashed line shows the material component, and the solid line shows the dark energy component as a percentage of the energy density. The curvature component is omitted here because its value is small and it is not the primary component at any time. The current time is $a = 10^0$, and the dark energy component will rapidly increase its share even more in the future.

Fig.2.2 shows the ratio of each energy component to the total energy along the redshift based on observations of the current energy density. In the early universe, the radiative component dominates, and then with expansion, the main energy component switches to matter such as dark matter around $z \sim 3000$. Furthermore, at redshift $z \sim$0.3, the dark energy exceeds the energy density of matter, and an accelerated expanding universe starts. Assume that there is no energy exchange across radiation, matter, and dark energy in the entire universe. Then the energy density of each will change only due to the expansion of space. The energy density of matter is inversely proportional to the volume of space($\propto$

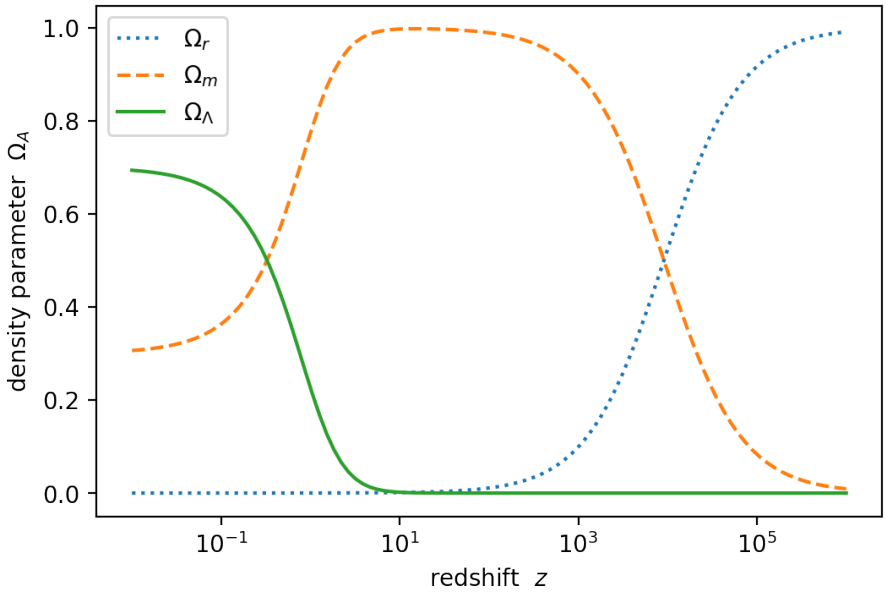

Figure 2.2: Evolution of each energy component along redshift. The dotted line shows the radiative component, the dashed line shows the material component, and the solid line shows the dark energy component as a percentage of the energy density. The curvature component is omitted here because its value is small and it is not the primary component at any time. In the current standard cosmological ΛCDM model, the energy densities of matter and dark energy are equal at redshift $z \sim 0.3$.

a^{-3}) and the energy density of radiation is further inversely proportional to the scale factor($\propto a^{-4}$) due to the further wavelength extension effect. Considering the variation of each component with the scale factor a, the energy density can be calculated from the current respective energy densities (radiation:ρ_{r0}, matter:ρ_{m0}, dark energy:ρ_{d0}) to

$$\rho_r = \frac{\rho_{r0}}{a^4}, \qquad \rho_m = \frac{\rho_{m0}}{a^3}, \qquad \rho_d = \rho_{d0} \exp\left[3\int_a^1 (1+w_{\mathrm{DE}})\frac{da}{a}\right] \tag{2.81}$$

The energy density of the entire universe is

$$\rho = \frac{\rho_{r0}}{a^4} + \frac{\rho_{m0}}{a^3} + \rho_{d0} \exp\left[3\int_a^1 (1+w_{\mathrm{DE}})\frac{da}{a}\right] \tag{2.82}$$

Rewrite Eq.(2.78) by adding the density parameter of curvature from Eq.(2.77).

$$\dot{a}^2 = H_0^2 \left\{ \frac{\Omega_{r0}}{a^2} + \frac{\Omega_{m0}}{a} + \Omega_{K0} + \Omega_{d0} a^2 \exp\left[3\int_a^1 (1+w_{\mathrm{DE}})\frac{da}{a}\right] \right\} \tag{2.83}$$

This describes the Friedman equation by the current density parameter. It represents the cosmic expansion $\dot{a}$ as determined for each period by the component that accounts for the largest fraction of the right-hand side. This is converted to a form describing the Hubble parameter in terms of the Hubble constant using

the redshift z.

$$H(z) = H_0 \Bigg[(1+z)^4 \Omega_{r0} + (1+z)^3 \Omega_{m0} + (1+z)^2 \Omega_{K0} + \Omega_{d0} \exp\left(3 \int_0^z \frac{1+w_{\mathrm{DE}}}{1+z} dz \right) \Bigg]^{1/2} \tag{2.84}$$

By integrating this $H(z)$ as Eq.(2.37), we can calculate the co-moving distance x to the source at redshift z. Thus, the density parameter determines the relationship between redshift and distance.

2.5 Einstein's equations in liner perturbation

In a homogeneous and isotropic universe, the metric can be determined as in Eq.(2.26). However, if it is not perfectly uniformly isotropic, it becomes a function of space-time. The general metric tensor is divided into uniform $\bar{g}_{\mu\nu}$ and non-uniform $h_{\mu\nu}$ components.

$$g_{\mu\nu} = \bar{g}_{\mu\nu} + h_{\mu\nu} \tag{2.85}$$

In the following, conformal time is adopted as the time coordinate, and homogeneous isotropic background space-time is represented as follows.

$$ds^2 = a^2(\tau) \left(-d\tau^2 + \gamma_{ij} dx^i dx^j \right) \tag{2.86}$$

The homogeneous isotropic background space-time metric is a solution to Einstein's equations. Consider that the non-uniform component is sufficiently small relative to the uniform component. Then $h_{\mu\nu}$ can be regarded as a perturbation, and the solution of Einstein's equations in the universe including the nonuniform component can be obtained using a linear approximation.
Three variables, A, B_i, and C_{ij}, are introduced for the perturbed components, which are deviations from the homogeneous and isotropic universe.

$$h_{00} = -2a^2 A, \qquad h_{0i} = -a^2 B_i, \qquad h_{ij} = 2a^2 C_{ij} \tag{2.87}$$

$$B^i \equiv \gamma^{ij} B_j, \qquad C^i{}_j \equiv \gamma^{ik} C_{kj}, \qquad C_i{}^j \equiv \gamma^{jk} C_{ik}, \qquad C^{ij} \equiv \gamma^{ik} \gamma^{jl} C_{kl} \tag{2.88}$$

The metric of the perturbed universe is

$$ds^2 = a^2(\tau) \left[-(1+2A) d\tau^2 - 2B_i d\tau dx^i + (\gamma_{ij} + 2C_{ij}) dx^i dx^j \right] \tag{2.89}$$

The specific metric is

$$g_{00} = -a^2(1+2A), \qquad g_{0i} = -a^2 B_i, \qquad g_{\mu\nu} = a^2(\gamma_{ij} + 2C_{ij}) \tag{2.90}$$

The inverse of the metric under linear approximation is

$$g^{00} = -\frac{1}{a^2}(1+2A), \qquad g^{0i} = -\frac{1}{a^2} B^i, \qquad g^{ij} = \frac{1}{a^2}(\gamma^{ij} - 2C^{ij}) \tag{2.91}$$

In the following, $\mathscr{H}$ is used instead of the Hubble parameter$H$, including the derivative in conformal time expressed as a prime.

$$\mathscr{H} \equiv \frac{1}{a} \frac{da}{d\tau} = \frac{a'}{a} = aH \tag{2.92}$$

Christoffel symbols containing perturbation variables are

$$\Gamma^0{}_{00} = \mathscr{H} + A' \tag{2.93}$$
$$\Gamma^0{}_{0i} = \Gamma^0{}_{i0} = A_{|i} - \mathscr{H} B_i \tag{2.94}$$
$$\Gamma^0{}_{ij} = \mathscr{H}(1-2A)\gamma_{ij} + \frac{1}{2}(B_{i|j} + B_{j|i}) + C^i{}_j{}' + 2\mathscr{H} C_{ij} \tag{2.95}$$
$$\Gamma^i{}_{00} = A^{|i} - (B^i)' - \mathscr{H} B^i \tag{2.96}$$
$$\Gamma^i{}_{0j} = \Gamma^i{}_{j0} = \mathscr{H}\delta^i{}_j + \frac{1}{2}(B_j{}^{|i} - B^i{}_{|j}) + C^i{}_j{}' \tag{2.97}$$
$$\Gamma^i{}_{jk} = {}^{(3)}\Gamma^i{}_{jk} + \mathscr{H} B^i \gamma_{jk} + C^i{}_{j|k} + C^i{}_{k|j} - C_{jk}{}^{|i} \tag{2.98}$$

The curvature tensor in background spacetime is the same as in Eq.(2.41)–Eq.(2.43). Similarly, we obtain a linear approximate form for the energy-momentum tensor.

$$T^\mu_{\ \nu} = (\rho + p) u^\mu u_\nu + p\delta^\mu_{\ \nu} + \sigma^\mu_{\ \nu} \tag{2.99}$$

where u^μ is the quaternary velocity of the fluid element and $\sigma^\mu{}_\nu$ is the non-stress tensor. The non-stress tensor is a symmetric tensor that is traceless and has only a spatial component.

$$\sigma^{\mu\nu} u_\nu = 0, \qquad g_{\mu\nu}\sigma^{\mu\nu} = 0, \qquad \sigma^{\mu\nu} = \sigma^{\nu\mu} \tag{2.100}$$

Spatial velocity is chosen independently from the quaternionic velocity.

$$v_i \equiv \frac{u^i}{u^0} \tag{2.101}$$

Background spacetime is homogeneous and isotropic and thus has no spatial velocity. Writing the quaternionic velocity in the linear approximation using the spatial velocity,

$$u^\mu = a^{-1}(1 - A, v^i) \tag{2.102}$$
$$u_\mu = a(-1 - A, v_i - B_i) \tag{2.103}$$

The unstress tensor likewise has no value in background spacetime, so it is only a perturbative component. Therefore, in a linear approximation, the metric in Eq.(2.100) remains only the background spacetime component.

$$\sigma^{00} = \sigma^{0i} = \sigma^{i0} = 0, \qquad \gamma_{ij}\sigma^{ij} = 0, \qquad \sigma^{ij} = \sigma^{ji} \tag{2.104}$$
$$\sigma^0{}_0 = \sigma^0{}_i = \sigma^i{}_0 = 0, \qquad \sigma^i{}_i = 0, \qquad \sigma^i{}_j = \sigma_j{}^i \tag{2.105}$$

In summary, each component of the energy-momentum tensor is obtained from Eq.(2.99)

$$T^0_{\ 0} = -\rho \tag{2.106}$$
$$T^0_{\ i} = (\rho + p)(v_i - B_i) \tag{2.107}$$
$$T^i_{\ 0} = -(\rho + p) v^i \tag{2.108}$$
$$T^i_{\ j} = p\delta^i{}_j + \sigma^i{}_j \tag{2.109}$$

We now define dimensionless energy density fluctuations δ and pressure fluctuations δp.

$$\delta \equiv \frac{\rho - \bar{\rho}}{\bar{\rho}}, \qquad \delta p \equiv p - \bar{p} \tag{2.110}$$

A dimensionless quantity is also defined for the non-stress tensor$\sigma^i{}_j$.

$$\Pi^i{}_j \equiv \frac{\sigma^i{}_j}{p} \tag{2.111}$$

Using these perturbation quantities, the energy-momentum tensor can be rewritten as

$$T^0{}_0 = -\bar{\rho} - \bar{\rho}\delta \tag{2.112}$$
$$T^0{}_i = (\bar{\rho} + \bar{p})(v_i - B_i) \tag{2.113}$$
$$T^i{}_0 = -(\bar{\rho} + \bar{p})v^i \tag{2.114}$$
$$T^i{}_j = \bar{p}\delta^i{}_j + \delta p\delta^i{}_j + \bar{p}\Pi^i{}_j \tag{2.115}$$

The Einstein tensor $G^\mu{}_\nu$ and energy-momentum tensor$T^\mu{}_\nu$ contained in the Einstein equation Eq.(2.56) with the cosmological term are divided into a background component and a perturbative component.

$$G^\mu{}_\nu = \bar{G}^\mu{}_\nu + \delta G^\mu{}_\nu, \qquad T^\mu{}_\nu = \bar{T}^\mu{}_\nu + \delta T^\mu{}_\nu \tag{2.116}$$

The background component satisfies the Einstein equation as Eq.(2.56).

$$\bar{G}^\mu{}_\nu + \Lambda\delta^\mu{}_\nu = 8\pi G\bar{T}^\mu{}_\nu \tag{2.117}$$

Subtract the background component to obtain the Einstein equation in the perturbed component.

$$\delta G^\mu{}_\nu = 8\pi G\delta T^\mu{}_\nu \tag{2.118}$$

The Einstein tensor of the background component is

$$\begin{aligned}\bar{G}^0{}_0 &= -\frac{4}{a^2}(\mathscr{H}^2 + K), \qquad \bar{G}^i{}_0 = \bar{G}^0{}_i = 0, \\ \bar{G}^i{}_j &= -\frac{1}{a^2}(2\mathscr{H}' + \mathscr{H}^2 + K)\delta^i{}_j\end{aligned} \tag{2.119}$$

Similarly, the energy-momentum tensor is

$$\bar{T}^0{}_0 = -\bar{\rho}, \qquad \bar{T}^i{}_0 = \bar{T}^0{}_i = 0, \qquad \bar{T}^i{}_j = \bar{p}\delta^i{}_j \tag{2.120}$$

Equations corresponding to the Friedman equation are derived from the Einstein equation using the components of background spacetime.

$$\mathscr{H}^2 = \frac{8\pi G}{3}a^2\bar{\rho} + \frac{\Lambda}{3}a^2 - K \tag{2.121}$$
$$\mathscr{H}' = \frac{4\pi G}{3}a^2(\bar{\rho} + 3\bar{p}) + \frac{\Lambda}{3}a^2 \tag{2.122}$$

Similarly, the energy-momentum conservation law is

$$\bar{\rho}' = -3\mathscr{H}(\bar{\rho} + \bar{p}) \tag{2.123}$$

The density parameter, state parameter, and sound velocity are also redefined using background space-time variables.

$$\Omega \equiv \frac{8\pi G a^2\bar{\rho}}{3\mathscr{H}^2}, \qquad w \equiv \frac{\bar{p}}{\bar{\rho}}, \qquad {c_s}^2 = \frac{\bar{p}'}{\bar{\rho}'} \tag{2.124}$$

Rewrite Eq.(2.122)–Eq.(2.123)using the time-dependent parameters of the background time component.

$$\mathscr{H}^2 = \mathscr{H}^2\Omega + \frac{\Lambda}{3}a^2 - K \tag{2.125}$$

$$\mathscr{H}' = -\frac{1}{2}\mathscr{H}^2\Omega(1+3w) + \frac{\Lambda}{3}a^2 \tag{2.126}$$

$$w' = -3\mathscr{H}(a+w)\left({c_s}^2 - w\right) \tag{2.127}$$

From these equations, we obtain

$$\mathscr{H}^2 + K - \mathscr{H}' = 4\pi G a^2(\bar{\rho}+\bar{p}) = \frac{3}{2}\mathscr{H}^2\Omega(1+w) \tag{2.128}$$

$$\mathscr{H}'' - \mathscr{H}\left(\mathscr{H}^2 + K + \mathscr{H}'\right) = -4\pi G a^2\bar{p}' = \frac{9}{2}\mathscr{H}^3\Omega(1+w){c_s}^2 \tag{2.129}$$

The spatial components of the Einstein equation for perturbations are divided into trace and non-trace components.

$$\delta G^i{}_i = 8'D\delta T^i{}_i, \qquad \delta G^i{}_j - \frac{1}{3}\delta^i{}_j G^k{}_k = 8\pi G\left(\delta T^i{}_j - \frac{1}{3}\delta^i{}_j\delta T^k{}_k\right) \tag{2.130}$$

For the perturbation component, the independent expressions derived from the Einstein equations are

$$3\mathscr{H}^2 A - \mathscr{H}B^i{}_{|i} - \mathscr{H}{C^i}_i{}' + K{C^i}_i - \frac{1}{2}C^{ij}{}_{|ij} + \frac{1}{2}C^i{}_{i|j}{}^{|j} = 4\pi G a^2\bar{\rho}\delta \tag{2.131}$$

$$\mathscr{H}A_{|i} + KB_i + \frac{1}{4}B_{i|j}{}^{|j} - \frac{1}{4}B^j{}_{|ij} + C^{j\prime}{}_{[i|j]} = -4\pi G a^2(\bar{\rho}+\bar{p})(v_i - B_i) \tag{2.132}$$

$$\begin{aligned} &3\mathscr{H}A' + 3\left(\mathscr{H}^2 + 2\mathscr{H}'\right)A + \triangle A - B^i{}_{|i}{}' - 2\mathscr{H}B^i{}_{|i} \\ &\quad -{C^i}_i{}'' - 2\mathscr{H}{C^i}_i{}' + K{C^i}_i - \frac{1}{2}C^{ij}{}_{|ji} + \frac{1}{2}C^i{}_{i|j}{}^{|j} = 12\pi G a^2\delta p \end{aligned} \tag{2.133}$$

$$\begin{aligned} &\left(\delta^i{}_k - \frac{1}{3}\gamma_{kl}\gamma^{ij}\right)\left(A_{|ij} - B_{(i|j)}{}' - 2\mathscr{H}B_{(i|j)} - C_{ij}{}'' - 2\mathscr{H}C_{ij}{}'' - 2\mathscr{H}C_{ij}{}'\right. \\ &\quad \left. +4KC_{ij} + C_{ij|m}{}^{|m} + C^m{}_{m|ij} - 2C_{m(i|j)}{}^{|m}\right) = -8\pi G a^2\bar{p}\Pi_{kl} \end{aligned} \tag{2.134}$$

Next, consider the covariant derivative of the energy-momentum tensor.

$$T^\mu{}_{\nu;\mu} = T^\mu{}_{\nu,\mu} + \Gamma^\mu{}_{\mu\lambda}T^\lambda{}_\nu - \Gamma^\lambda{}_{\mu\nu}T^\mu{}_\lambda \tag{2.135}$$

Under the linear approximation, the time and space components are respectively

$$T^\mu{}_{0;\mu} = -\bar{\rho}' - 3\mathscr{H}(\bar{\rho}+\bar{p}) - (\bar{\rho}\bar{p}) - 3\mathscr{H}(\bar{\rho}\delta + \delta p) - (\bar{\rho}+\bar{p})\left(v^i{}_{|i} + C^i{}_i{}'\right) \tag{2.136}$$

$$T^\mu{}_{i;\mu} = [(\bar{\rho}+\bar{p})(v_i - B_i)]' + 4\mathscr{H}(\bar{\rho}+\bar{p})(v_i - B_i) + (\bar{\rho}+\bar{p})A_{|i} + \delta p_{|i} + \bar{p}\Pi^j{}_{i|j} \tag{2.137}$$

Assuming that pressure is a function of energy density and entropy, pressure fluctuations can be expressed using entropy fluctuations as

$$\delta p = \left(\frac{\partial p}{\partial \rho}\right)\bigg|_S \delta\rho + \left(\frac{\partial p}{\partial S}\right)\bigg|_\rho \delta S = {c_s}^2\bar{\rho}\delta + \left(\frac{\partial p}{\partial S}\right)\bigg|_\rho \delta S \tag{2.138}$$

In addition, we define dimensionless entropy fluctuations.

$$\Gamma = \frac{\delta p - {c_s}^2\bar{\rho}\delta}{\bar{p}} = \frac{\delta p}{\bar{p}} - \frac{{c_s}^2}{w}\delta \tag{2.139}$$

Using entropy fluctuations, the following can be derived from the energy-momentum conservation law

$$\delta' + 3\mathscr{H}\left({c_s}^2 - w\right)\delta + (1+w)\left(v^i{}_{|i} + C^i{}_i{}'\right) + 3\mathscr{H}w\Gamma = 0 \tag{2.140}$$

$$(v_i - B_i)' + \mathscr{H}\left(1 - 3{c_s}^2\right)(v_i - B_i) + \frac{{c_s}^2}{1+w}\delta_{|i} + A_{|i} + \frac{w}{1+w}\left(\Gamma_{|i} + \Pi^j{}_{i|j}\right) = 0 \tag{2.141}$$

2.6 Gauge conversion and scalar mode

Consider minute coordinate transformations in perturbed spacetime.

$$x^\mu \to \tilde{x}^\mu = x^\mu + \xi^\mu \tag{2.142}$$

The metric conversion is

$$g_{\mu\nu}(x) \to \tilde{g}_{\mu\nu}(\tilde{x}) = \frac{\partial x^\alpha}{\partial \tilde{x}^\mu}\frac{\partial x^\beta}{\partial \tilde{x}^\nu} g_{\alpha\beta}(x) \tag{2.143}$$

Using a linear approximation, given the change in the metric tensor

$$\begin{aligned}\tilde{g}_{\mu\nu}(x) - g_{\mu\nu}(x) &= \tilde{g}_{\mu\nu}(\tilde{x}) - g_{\mu\nu}(x) - g_{\mu\nu,\alpha}(x)\xi^\alpha \\ &= -g_{\mu\alpha}(x)\xi^\alpha{}_{,\nu} - g_{\nu\alpha}(x)\xi^\alpha{}_{,\mu} - g_{\mu\nu,\alpha}(x)\xi^\alpha\end{aligned} \tag{2.144}$$

The change in coordinates is also a perturbation quantity, and the spatial and temporal components are calculated respectively

$$A \to \tilde{A} = A - T' - \mathscr{H}T \tag{2.145}$$

$$B_i \to \tilde{B}_i = B_i + L_i{}' - T_{|i} \tag{2.146}$$

$$C_{ij} \to \tilde{C}_{ij} - \mathscr{H}T\gamma_{ij} - L_{(i|j)} \tag{2.147}$$

where we divide the coordinate transformation vector into time component T and space component L^i.
For the energy-momentum tensor, the transformation also yields

$$\tilde{T}^\mu{}_\nu(x) - T^\mu{}_\nu(x) = T^\alpha{}_\nu(x)\xi^\mu{}_{,\alpha} - T^\mu{}_\beta(X)\xi^\beta{}_{,\nu} - T^\mu{}_{\nu,\alpha}(X)\xi^\alpha \tag{2.148}$$

Calculating the energy-momentum tensor component-by-component, we find that each element is transformed as follows.

$$\delta \to \tilde{\delta} - \delta - \frac{\bar{\rho}'}{\bar{\rho}}T \tag{2.149}$$

$$v_i \to \tilde{v}_i = v_i + L_i' \tag{2.150}$$

$$\delta p \to \tilde{\delta p} = \delta p - \bar{p}'T \tag{2.151}$$

$$\Pi^i{}_j \to \tilde{\Pi}^i{}_j = \Pi^i{}_j \tag{2.152}$$

$$\Gamma \to \tilde{\Gamma} = \Gamma \tag{2.153}$$

Consider the scalar, vector, and tensor decomposition of the perturbed component A, B_i, C_{ij}. Only the scalar components that are ultimately needed are shown here. Since A has only a scalar component, no decomposition is performed. B_i is divided into a covariate differential component of the scalar field $B^{(\mathrm{S})}$ and other components.

$$B_i = B^{(\mathrm{S})}{}_{|i} + B^{(\mathrm{V})}{}_i \tag{2.154}$$

Since $B^{(\mathrm{S})}$ satisfies $\triangle B^{(\mathrm{S})} = B_i{}^{|i}$,

$$B^{(\mathrm{S})} = \triangle^{-1}\nabla^i B_i \tag{2.155}$$

Since C is a tensor, it is decomposed into four components, including two scalar fields D, $E^{(\mathrm{S})}$

$$C_{ij} = \gamma_{ij}D + E^{(\mathrm{S})}{}_{|ij} + E^{(\mathrm{V})}{}_{(i|j)} + E^{(\mathrm{T})}{}_{ij} \tag{2.156}$$

The contraction and covariant derivative of C_{ij} is

$$C_i{}^i = 3D + \triangle E^{(\mathrm{S})} \tag{2.157}$$

$$C_{ij}{}^{|j} = D_{|i} + \left[(\triangle + 2K)E^{(\mathrm{S})}\right]_{|i} + \frac{1}{2}E^{(\mathrm{V})}{}_{i|j}{}^{|j} + KE^{(\mathrm{V})}{}_i \tag{2.158}$$

$$C_{ij}{}^{|ji} = \triangle\left(D + \triangle E^{(\mathrm{S})} + 2KE^{(\mathrm{S})}\right) \tag{2.159}$$

From Eq.(2.157) and Eq.(2.159),

$$D = \frac{1}{3}C_i{}^i - \frac{1}{2}\triangle(\triangle + 3K)^{-1}\left(\triangle^{-1}\nabla^i\nabla^j C_{ij} - \frac{1}{3}C_i{}^i\right) \tag{2.160}$$

$$E^{(\mathrm{S})} = \frac{3}{2}(\triangle + 3K)^{-1}\left(\triangle^{-1}\nabla^i\nabla^j C_{ij} - \frac{1}{3}C_i{}^i\right) \tag{2.161}$$

The variable L_i in the gauge transformation is decomposed in the same way,

$$L_i = L^{(\mathrm{S})}{}_{|i} + L^{(\mathrm{V})}{}_i \tag{2.162}$$

In summary, the gauge transformation of the scalar component of perturbation component of background spacetime are written as

$$A \to \tilde{A} = A - T' - \mathscr{H}T \tag{2.163}$$

$$B^{(\mathrm{S})} \to \tilde{B}^{(\mathrm{S})} = B^{(\mathrm{S})} + L^{(\mathrm{S})\prime} - T \tag{2.164}$$

$$D \to \tilde{D} = D - \mathscr{H}T \tag{2.165}$$

$$E^{(\mathrm{S})} \to \tilde{E}^{(\mathrm{S})} = E^{(\mathrm{S})} - L^{(\mathrm{S})} \tag{2.166}$$

Similarly, we perform SVT decompositions for perturbations of the energy-momentum tensor.

$$v_i = v^{(\mathrm{S})}{}_{|i} + v^{(\mathrm{V})}{}_i \tag{2.167}$$

Since the non-stress tensor has no trace component.

$$\Pi_{ij} = \Pi^{(\mathrm{S})}{}_{|ij} - \ 13\gamma_{ij}\triangle\Pi^{(\mathrm{S})} + \Pi^{(\mathrm{V})}{}_{(i|j)} + \Pi^{(\mathrm{T})}{}_{ij} \tag{2.168}$$

Thus, for the scalar components of perturbations of the energy-momentum tensor,

$$\delta \to \tilde{\delta} = \delta - \frac{\bar{\rho}'}{\bar{\rho}}T \tag{2.169}$$

$$v^{(\mathrm{S})} \to \tilde{v}^{(\mathrm{S})} = v^{(\mathrm{S})} + L^{(\mathrm{S})\prime} \tag{2.170}$$

$$\delta p \to \tilde{\delta p} = \delta p - \bar{p}'T \tag{2.171}$$

$$\Pi^{(\mathrm{S})} \to \tilde{\Pi}^{(\mathrm{S})} = \Pi^{(\mathrm{S})} \tag{2.172}$$

In gauge conversion, the scalar, vector, and tensor components are transformed independently. The linear Einstein equation in the scalar component is written as

$$3\mathscr{H}^2A - \mathscr{H}\triangle B^{(\mathrm{S})} - 3\mathscr{H}D' + (\triangle + 3K)D - \mathscr{H}\triangle E^{(\mathrm{S})\prime} = -4\pi Ga^2\bar{\rho}\delta \tag{2.173}$$

$$\mathscr{H}A + KB^{(\mathrm{S})} - D' + KE^{(\mathrm{S})\prime} = -4\pi Ga^2(\bar{\rho} + \bar{p})\left(v^{(\mathrm{S})} - B^{(\mathrm{S})}\right) \tag{2.174}$$

$$3\mathscr{H}A' + \left(\mathscr{H}^2 + 2\mathscr{H}'\right)A + \triangle A - \triangle B77^{(\mathrm{S})\prime} - 2\mathscr{H}\triangle B^{(\mathrm{S})} - 3D'' - 6\mathscr{H}D' + (\triangle + 3K)D - \triangle E^{(\mathrm{S})\prime\prime} - 2\mathscr{H}\triangle E^{(\mathrm{S})\prime} = 12\pi Ga^2\delta p \tag{2.175}$$

$$A - B^{(\mathrm{S})\prime} - 2\mathscr{H}B^{(\mathrm{S})} + D - E^{(\mathrm{S})\prime\prime} - 2\mathscr{H}E^{(\mathrm{S})\prime} = -8\pi Ga^2\bar{p}\Pi^{(\mathrm{S})} \tag{2.176}$$

In the following, we will find the gauge invariants in scalar-type perturbations. The following two relations are adopted from the gauge transformation equation for scalar-type perturbations.

$$\tilde{B}^{(\mathrm{S})} + \tilde{E}^{(\mathrm{S})\prime} = B^{(\mathrm{S})} + E^{(\mathrm{S})\prime} - T \tag{2.177}$$

$$\tilde{E}^{(\mathrm{S})} = E^{(\mathrm{S})} - L^{(\mathrm{S})} \tag{2.178}$$

Using these equations, we remove the variables of the gauge transformation and define two variables that are not changed by the gauge transformation.

$$\Phi = A - \left(B^{(\mathrm{S})} + E^{(\mathrm{S})\prime}\right)' - \mathscr{H}\left(B^{(\mathrm{S})} + E^{(\mathrm{S})\prime}\right) \tag{2.179}$$

$$\Psi = D - \mathscr{H}\left(B^{(\mathrm{S})} + E^{(\mathrm{S})\prime}\right) \tag{2.180}$$

Also, since the perturbation variables for the energy component are not gauge invariants, we construct gauge-invariant variables using Eq.(2.177) and Eq.(2.178).

$$\delta^{(\mathrm{GI})}\delta + 3\mathscr{H}(1+w)\left(B^{(\mathrm{S})} + E^{(\mathrm{S})\prime}\right) \tag{2.181}$$

$$v^{(\mathrm{GI})} = v^{(\mathrm{S})} + E^{(\mathrm{S})\prime} \tag{2.182}$$

$$\delta p^{(\mathrm{GI})} = \delta p + 3\mathscr{H}\bar{\rho}{c_s}^2(1+w)\left(B^{(\mathrm{S})} + E^{(\mathrm{S})\prime}\right) \tag{2.183}$$

The linear Einstein equations for the scalar-type components are expressed in terms of these gauge-invariant perturbation variables as

$$3\mathscr{H}(\mathscr{H}\Phi - \Psi') + (\triangle + 3K)\Psi = -4\pi G a^2 \bar{\rho}\delta^{(\mathrm{GI})} \tag{2.184}$$

$$\mathscr{H}\Phi - \Psi' = 4\pi G a^2(\bar{\rho} + \bar{p})v^{(\mathrm{GI})} \tag{2.185}$$

$$\triangle\Phi + (\triangle + 3K)\Psi + 3\left(\mathscr{H}^2 + 2\mathscr{H}'\right)\Phi + 3\mathscr{H}\Phi' - 6\mathscr{H}\Psi' - 3\Psi'' = 12\pi G a^2 \delta p^{(\mathrm{GI})} \tag{2.186}$$

$$\Phi + \Psi = -8\pi G a^2 \bar{p}\Pi^{(\mathrm{S})} \tag{2.187}$$

We adopt the Newtonian conformal gauge. Its conditions are

$$B^{(\mathrm{S})} = E^{(\mathrm{S})} = 0 \tag{2.188}$$

Then the gauge invariants in the background spacetime are

$$\Phi = A, \qquad \Psi = D \tag{2.189}$$

And the line element is written as

$$ds^2 = a^2(\tau)\left[-(1+2\Phi)d\tau^2 + (1+2\Psi)\gamma_{ij}dx^i dx^j)\right] \tag{2.190}$$

In the Newtonian conformal gauge, Gauge invariants of energy components are consistent with those before making them gauge-invariant.

$$\delta^{(\mathrm{GI})} = \delta, \qquad v^{(\mathrm{GI})} = v^{(\mathrm{S})}, \qquad \delta p^{(\mathrm{GI})} = \delta p \tag{2.191}$$

Although we defined gauge invariants earlier, one of the other variables that are gauge invariants is called the Bardeen's variable. In the Bardeen's variable, gauge-invariant density fluctuation is defined as

$$\Delta \equiv \delta^{(\mathrm{GI})} - 3\mathscr{H}(1+w)v^{(\mathrm{GI})} = \delta + \frac{\bar{\rho}'}{\bar{\rho}}\left(v^{(\mathrm{S})} - B^{(\mathrm{S})}\right) \tag{2.192}$$

Rewriting with the Bardeen's variable

$$\Delta' - 3\mathscr{H}w\Delta = -(\triangle + 3K)\left[(1+w)V - 2\mathscr{H}w\Pi\right] \tag{2.193}$$

$$V' + \mathscr{H}V = -\frac{{c_s}^2}{1+w}\Delta - \Phi - \frac{w}{1+w}\left[\Gamma + \frac{2}{3}(\triangle + 3K)\Pi\right] \tag{2.194}$$

$$(\triangle + 3K)\Psi = 4\pi G a^2 \bar{\rho}\Delta \tag{2.195}$$

$$\Phi + \Psi = -8\pi G a^2 \bar{p}\Pi \tag{2.196}$$

where we describe $v^{(\mathrm{GI})}$ as V and $\Pi^{(\mathrm{S})}$ as Π. The Einstein equation for scalar-type perturbations also yields an equation called the Bardeen equation.

$$\Psi'' + 3\mathscr{H}\left(1 + {c_s}^2\right)\Psi' - {c_s}^2 \triangle \Psi \tag{2.197}$$

$$+ \left[8\pi G a^2 \bar{\rho}\left({c_s}^2 - w\right) + \Lambda a^2\left(1 + {c_s}^2\right) - 2K\left(1 + 3{c_s}^2\right)\right]\Psi \tag{2.198}$$

$$= -8\pi G a^2 \bar{\rho}\left\{\frac{1}{2}w\Gamma + \mathscr{H}w\Pi' + \frac{1}{3}w \triangle \Pi + \left[\frac{8\pi G}{3}a^2\bar{\rho}\left(2w - 3w^2 - 3{c_s}^2\right)\right. \right. \tag{2.199}$$

$$\left. \left. + \frac{\Lambda}{3}a^2\left(5w - 3{c_s}^2\right) + 3K\left({c_s}^2 - w\right)\right]\Pi\right\} \tag{2.200}$$

Solving these for each variable yields

$$\Delta = -\frac{(\triangle + 3K)\Psi}{4\pi G a^2 \bar{\rho}} \tag{2.201}$$

$$\Phi = -\Psi - 8\pi G a^2 \bar{p}\Pi \tag{2.202}$$

$$V = \frac{\Psi' - \mathscr{H}\Phi}{4\pi G a^2(\bar{\rho} + \bar{p})} \tag{2.203}$$

2.7 Evolution of potential in each dominant era

In the universe after the radiation-dominated period, the equation of state parameters are equal to the speed of sound, and the non-stress tensor and entropy fluctuations can be approximately neglected.

$$w = {c_s}^2, \qquad \gamma = \Pi = 0 \tag{2.204}$$

Since the non-stress tensor is negligible,

$$\Psi = -\Phi \tag{2.205}$$

Also, by mode decomposition of the Bardeen equation, the following equation is obtained.

$$\Phi'' + 3\mathscr{H}\left(1 + {c_s}^2\right)\Phi' + {c_s}^2 k^2 \Phi + \left[\Lambda a^2\left(1 + {c_s}^2\right) - 2K\left(1 + 3{c_s}^2\right)\right]\Phi = 0 \tag{2.206}$$

Similarly, an expression describing a Bardeen variable can be mode decomposed to

$$\Delta = -\frac{k^2 - 3K}{4\pi G a^2 \bar{\rho}}\Phi, \qquad V = -\frac{(a\Phi)'}{4\pi G a^2 \bar{\rho}(1+w)} \tag{2.207}$$

First, consider the radiation-dominated phase, which is the earliest time in this condition. Since the radiative component is dominant

$$w = {c_s}^2 = \frac{1}{3}, \qquad \Lambda = K = 0 \tag{2.208}$$

The time dependence of the scale factor is

$$a \propto \tau, \qquad \tau, \qquad \mathscr{H} = \frac{1}{\tau}, \qquad \mathscr{H}' = -\frac{1}{\tau^2} \tag{2.209}$$

Using these, the Bardeen equation can be expressed as a simple differential equation of potential.

$$\Phi'' + \frac{4}{\tau}\Phi' + \frac{k^2}{3}\Phi = 0 \tag{2.210}$$

The potential that is the solution of the equation is found to be

$$\Phi = \frac{9\phi_{\mathrm{ini}}}{k^2\tau^2}\left(\frac{\sqrt{3}}{k\tau}\sin\frac{k\tau}{\sqrt{3}} - \cos\frac{k\tau}{\sqrt{3}}\right) \tag{2.211}$$

where ϕ_{ini} is derived from the integration constant and is determined by the initial conditions. From the obtained potentials, the other Bardeen variables are

$$\Delta = -6\phi_{\mathrm{ini}}\left(\frac{\sqrt{3}}{k\tau}\sin\frac{k\tau}{\sqrt{3}} - \cos\frac{k\tau}{\sqrt{3}}\right) \tag{2.212}$$

$$V = \frac{9\sqrt{3}\phi_{\mathrm{ini}}}{k^3\tau^2}\left[\left(1 - \frac{k^2\tau^2}{6}\right)\sin\frac{k\tau}{\sqrt{3}} - \frac{k\tau}{\sqrt{3}}\cos\frac{k\tau}{\sqrt{3}}\right] \tag{2.213}$$

Next, consider the material dominance period. In matter, the pressure is sufficiently small.

$$w = {c_s}^2 = 0, \qquad \Lambda = K = 0 \tag{2.214}$$

The time dependence of the scale factor and the expansion rate is described as

$$a \propto \tau^2, \qquad \mathscr{H} = \frac{2}{\tau}, \qquad \mathscr{H}' = -\frac{2}{\tau^2} \tag{2.215}$$

The Bardeen equation can be expressed as a differential equation of potential.

$$\Phi'' + \frac{6}{\tau}\Phi' = 0 \tag{2.216}$$

This equation has a time-invariant static solution and we describe its potential as

$$\Phi = \phi_{\mathrm{m}} \tag{2.217}$$

And the other Bardeen variables are

$$\Phi = \phi_{\mathrm{m}}, \qquad \Delta = -\frac{\phi_{\mathrm{m}}}{6}k^2\tau^2, \qquad V = -\frac{\phi_{\mathrm{m}}}{3}\tau \tag{2.218}$$

The curvature fluctuations in the long wavelength limit, which are conserved beyond the Hubble scale, allow us to link the unique potential values of the radiation-dominated and matter-dominated phases, respectively.

$$\phi_{\mathrm{m}} = \frac{9}{10}\phi_{\mathrm{ini}} \tag{2.219}$$

Finally, consider the dark Λ-dominant era, which is later than the matter-dominant era. Assuming that the speed of sound is negligible,

$$w = {c_s}^2 = 0 \tag{2.220}$$

The Bardeen equation, which includes the cosmological constant and curvature, is

$$\Phi'' + 3\mathscr{H}\Phi' + \left(\Lambda a^2 - 2K\right)\Phi = 0 \tag{2.221}$$

The Bardeen variables for density fluctuations and velocity are

$$\Delta = -\frac{k^2 - 3K}{4\pi G\bar{\rho}_0} a\Phi, \qquad V = -\frac{(a\Phi)'}{4\pi G\bar{\rho}_0} \tag{2.222}$$

Using the cosmological constant and curvature, the expansion rate can be written as

$$\mathscr{H}^2 = \frac{8\pi G\bar{\rho}_0}{3a} + \frac{\Lambda}{3}a^2 - K, \qquad \mathscr{H}' = -\frac{4\pi G\bar{\rho}_0}{3a} + \frac{\Lambda}{3}a^2, \qquad \frac{\mathscr{H}''}{\mathscr{H}} = \frac{4\pi G\bar{\rho}_0}{3a} + \frac{2}{3}\Lambda a^2 \tag{2.223}$$

Using these equations to solve the Bardeen equation, we obtain

$$\Phi = \frac{20\pi G\bar{\rho}_0}{3}\phi_{\mathrm{m}}\frac{\mathscr{H}}{a^2}\int_0^a \frac{da}{\mathscr{H}^3} \tag{2.224}$$

The time evolution part of this solution in the Λ-dominant period is defined as a linear growth factor.

$$D_+(\tau) \equiv \frac{20\pi G\bar{\rho}_0}{3}\frac{\mathscr{H}}{a}\int_0^a \frac{da}{\mathscr{H}^3} \tag{2.225}$$

Using this to write the Bardeen variable, the potential is

$$\Phi = \frac{D_+}{a}\phi_{\mathrm{m}} \tag{2.226}$$

The other variables are

$$\Delta = -\frac{k^2 - 3K}{4\pi G\bar{\rho}_0} D_+\phi_{\mathrm{m}}, \qquad V = -\frac{\mathscr{H}D_+\frac{D_+'}{\mathscr{H}D_+}\phi_{\mathrm{m}}}{4\pi G\bar{\rho}_0} \tag{2.227}$$

The linear growth factor can also be expressed using an energy density parameter.

$$D_+ = \frac{5}{2}a\Omega_{\mathrm{m}}\int_0^1 \frac{dx}{(\Omega_{\mathrm{m}}/x + \Omega_\Lambda x^2 + \Omega_K)^{3/2}} \tag{2.228}$$

Chapter 3

Remote quadrupole from galaxy clusters

3.1 Correlation remote quadrupole

$T = T_{\rm CMB} + \Delta T$ is the temperature of the CMB radiation looking in the direction $\hat{n}$ from coordinate $\vec{x}$ at conformal time τ. The deviation of the CMB from the average temperature, normalized by the average temperature, is written as

$$\Delta(\vec{x}, \hat{n}, \tau) \equiv \frac{\Delta T(\vec{x}, \hat{n}, \tau)}{T_{\rm CMB}} \tag{3.1}$$

Given that the CMB surface was expanded using spherical harmonic functions

$$\Delta(\vec{x}, \hat{n}, \tau) = \sum_{l=0}^{\infty} \sum_{m=-l}^{l} a_{lm}(\vec{x}, \tau) Y_{lm}(\hat{n}) \tag{3.2}$$

The two-point correlation function of the temperature fluctuation at arbitrary points is written as

$$\left\langle \Delta(\vec{x}, \hat{n}, \tau) \Delta(\vec{x}', \hat{n}', \tau') \right\rangle = \sum_{lm} \sum_{l'm'} C_{lml'm'}(\vec{x}, \tau, \vec{x}', \tau') Y_{lm}(\hat{n}) Y^*_{l'm'}(\hat{n}') \tag{3.3}$$

The commonly used CMB correlation function is used here.

$$C_{lml'm'}(\vec{x}, \tau, \vec{x}', \tau') \equiv \left\langle a_{lm}(\vec{x}, \tau) a^*_{l'm'}(\vec{x}', \tau') \right\rangle \tag{3.4}$$

This correlation function has some symmetries due to the properties of spherical harmonic functions.

$$C_{l,-m,l',-m'}(\vec{x}, \vec{x}') = (-1)^{m+m'} C^*_{lml'm'}(\vec{x}, \vec{x}') \tag{3.5}$$

$$C_{lml'm'}(\vec{x}', \vec{x}) = C^*_{l'm'lm}(\vec{x}, \vec{x}') \tag{3.6}$$

What we observe is linearly polarized light resulting from the scattering of CMB photons by clusters of galaxies. CMB photons scattered by a galaxy cluster at position $\vec{x}$ propagate to the observer $t = |\vec{x}|$ after scattering. Therefore, the last scattering surface, which is the source of linearly polarized light, is the last scattering surface observed by the galaxy cluster at time $\tau = \tau_0 - |\vec{x}|$, with the last scattering time as τ_0 as shown in Fig.3.1. Since the last scattering time τ_0 is constant, in the following, we consider only the $\tau = \tau_0 - |\vec{x}|$ case and don't denote τ. We now check the properties of the expansion coefficients a_{lm}, which of the spherical harmonic function expansion. At any given point, different components are uncorrelated and independent. However, when considering combinations at different points, some of the combinations are correlated. This can be understood

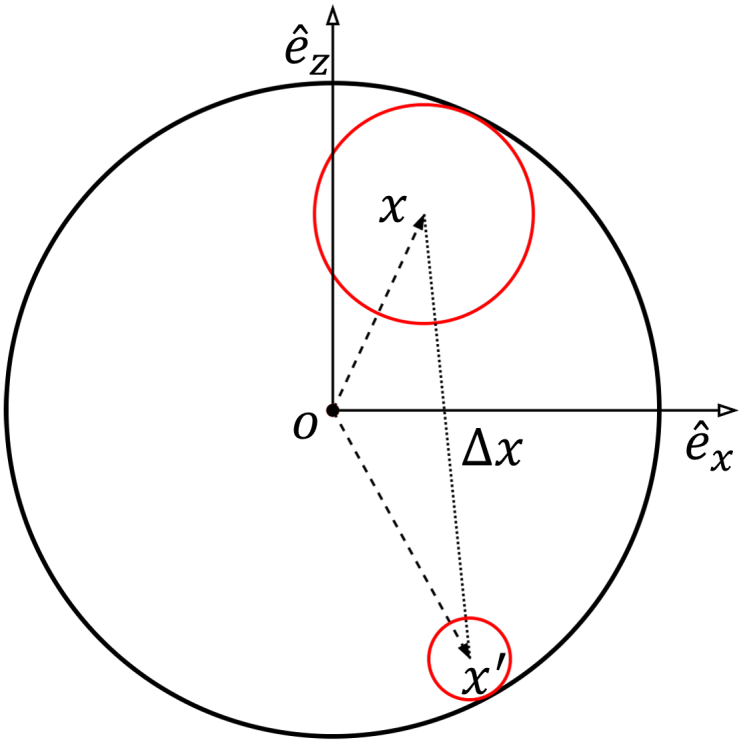

Figure 3.1: Cluster of galaxies and last scattering surface in the co-moving coordinate system. The origin is the observer, the circle enclosing the whole system is the last scattering surface, which is the CMB directly observed by the observer, and the inner region is the interior of the light cone. x and x' indicate the positions of the galaxy clusters, and since each cluster is on the light cone of the observer, their conformal times are $\tau = \tau_0 - |\vec{x}|$ and $\tau' = \tau_0 - |\vec{x}'|$, respectively. The small red circles indicate the last scattering surface of the clusters, which is always inscribed on the observer's last scattering surface.

from the fact that the last scattering surfaces at different points overlap. The covariance matrix of the coefficients a_{lm} is

$$R_{ij} = \left\langle a_{l_i m_i}(\vec{x}_i) a^*_{l_j m_j}(\vec{x}_j) \right\rangle = C_{l_i m_i l_j m_j}(\vec{x}_i, \vec{x}_j) \tag{3.7}$$

Now consider the relationship between the correlation function and the transfer function of the CMB. The temperature anisotropy can be Fourier expanded in comoving wave number $\vec{k}$ on the three-dimensional hyper-surface of conformal time τ, Σ_τ

$$\Delta(\vec{x}, \hat{n}, \tau) = \int d^3k e^{i\vec{k}\cdot\vec{x}} \Delta(\vec{k}, \hat{n}; \Sigma_\tau) \tag{3.8}$$

where left side $\Delta(\vec{x}, \hat{n}, \tau)$ indicates temperature anisotropy in real space and right side $\Delta(\vec{k}, \hat{n}; \Sigma_\tau)$ is the Fourier transform. Using the Legendre polynomial, we expand the temperature anisotropy in Fourier form.

$$\Delta(\vec{k}, \hat{n}; \Sigma_\tau) = \sum_{l=0}^{\infty} (-i)^l (2l+1) \Delta_l(\vec{k}, \tau) P_l(\hat{k}, \hat{n}) \tag{3.9}$$

Here, it can be divided into a CMB anisotropy part $\Delta(\vec{k}, \tau)$, which is a function of wavenumber and time, and a Lejandre polynomial, which has direction $\hat{k} \cdot \hat{n}$

as an argument. Using these functions, we can write the temperature anisotropy of real space as

$$\Delta(\vec{x},\hat{n},\tau) = 4\pi \int d^3k e^{i\vec{k}\cdot\vec{x}} \sum_{l=0}^{\infty} (-i)^l \Delta_l(\vec{k},\tau) \sum_{m=-l}^{l} Y^*_{lm}(\hat{k}) Y_{lm}(\hat{n}) \tag{3.10}$$

With the orthogonality of the spherical harmonic Y_{lm}, the coefficient of temperature anisotropy a_{lm} is

$$a_{lm}(\vec{x},\tau) = \int d\Omega \Delta(\vec{x},\hat{n},\tau) Y^*_{lm}(\hat{n}) \tag{3.11}$$

$$= (-i)^l 4\pi \int d^3k e^{i\vec{k}\cdot\vec{x}} \Delta_l(\vec{k},\tau) Y^*_{lm}(\hat{k}) \tag{3.12}$$

Using this form, the correlation function is

$$C_{lml'm'}(\vec{x},\vec{x}') = (-i)^{l-l'}(4\pi)^2 \int d^3k \int d^3k' e^{i\vec{k}\cdot\vec{x}} e^{-ik'\cdot x'} \tag{3.13}$$

$$\times \left\langle \Delta_l(\vec{k},\tau) \Delta^*_{l'}(\vec{k}',\tau') \right\rangle Y^*_{lm}(\hat{k}) Y_{l'm'}(\hat{k}') \tag{3.14}$$

In linear perturbation theory, the time evolution of the CMB temperature anisotropy is independent of the direction $\hat{k}$ and depends only on its scale $|\vec{k}|$. Therefore, the CMB temperature anisotropy can be divided into a transfer function with k corresponding to the scale and an initial potential fluctuation $\phi_{\rm ini}(\vec{k})$.

$$\Delta_l(\vec{k},\tau) = \phi_{\rm ini}(\vec{k}) \Delta_l(k,\tau) \tag{3.15}$$

If the initial potential perturbation is described by a Gaussian, then its correlation function is

$$\left\langle \phi_{\rm ini}(\vec{k}) \phi^*_{\rm ini}(\vec{k}') \right\rangle = P_\phi(k) \delta^3(\vec{k}-\vec{k}') \tag{3.16}$$

where $P_\phi(k)$ is the power spectrum of the initial potential fluctuations. From these, the correlation function for temperature anisotropy is

$$\left\langle \Delta_l(\vec{k},\tau) \Delta^*_{l'}(\vec{k}',\tau') \right\rangle = \Delta_l(k,\tau) \Delta_{l'}(k'\tau') P_\phi(k) \delta^3(\vec{k}-\vec{k}') \tag{3.17}$$

The correlation function at the same point is

$$C_{lml'm'}(\vec{x},\vec{x}) = (4\pi)^2 \delta_{l'l} \delta_{m'm} \int k^2 dk \Delta^2_l(k,\tau) P_\phi(k)$$

$$\equiv \delta_{l'l} \delta_{m'm} C_l(\tau) \tag{3.18}$$

where $C_l(\tau) \equiv \left\langle |a_{lm}(\vec{x},\tau)|^2 \right\rangle$ shows the emsemble average of CMB power spectrum with l harmonic at conformal time τ. In general case $\vec{x} \neq \vec{x}'$, the correlation function is wrriten as

$$C_{lml'm'}(\vec{x},\vec{x}') = (-i)^{l-l'}(4\pi)^2 \int d^3k e^{i\vec{k}\cdot\vec{x}} \Delta_l(k,\tau)$$

$$\times \Delta_{l'}(k,\tau') P_\phi(k) Y^*_{lm}(\hat{k}) Y_{l'm'}(\hat{k}) \tag{3.19}$$

The angular part included in the integral is expanded by the spherical Bessel function.

$$\exp(i\vec{k}\cdot\Delta\vec{x}) = \sum_{l''=0}^{\infty} (2l''+1) i^{l''} P_{l''}(\hat{k}\cdot\Delta\hat{x}) j_{l''}(k\,|\Delta\vec{x}|)$$

$$= 4\pi \sum_{l''}^{\infty} i^{l''} j_{l''}(k\,|\Delta\vec{x}|) \sum_{m''=-l''}^{l''} Y^*_{l''m''}(\hat{k}) Y_{l''m''}(\Delta\hat{x}) \tag{3.20}$$

where we define the difference between points $\Delta x \equiv \vec{x} - \vec{x}'$ and their angular $\Delta\hat{x} \equiv (\vec{x} - \vec{x}')/|\vec{x} - \vec{x}'|$. The correlation function becomes

$$C_{lml'm'}(\vec{x}, \vec{x}') = (4\pi)^3 \int k^2 dk \Delta_l(k,\tau)\Delta_{l'}(k,\tau')P_\phi(k)(-i)^{l-l'}(-1)^m \times \sum_{l''m''} i^{l''} j_{l''}(k\,|\Delta\vec{x}|) \int d\Omega_k Y_{l,-m}(\hat{k}) Y_{l'm'}(\hat{k}) Y^*_{l''m''}(\hat{k}) \quad (3.21)$$

The part including three spherical harmonics can be written with the Wigner 3j symbols.

$$\int d\Omega_k Y_{lm}(\hat{k}) Y_{l'm'}(\hat{k}) Y^*_{l''m''}(\hat{k}) = \sqrt{\frac{(2l+1)(2l'+1)(2l''+1)}{4\pi}} \begin{pmatrix} l & l' & l'' \\ 0 & 0 & 0 \end{pmatrix} \begin{pmatrix} l & l' & l'' \\ m & m' & m'' \end{pmatrix} \quad (3.22)$$

the Wigner 3j symbols has to satisfy two conditions for having a non-zero value. One is $m + m' = m''$, which determines m''. The other is triangle condition $|l - l'| \leq l'' \leq l + l'$. Thus the correlation function is

$$C_{lml'm'}(\vec{x}, \vec{x}') = (-i)^{l-l'}(-1)^m(4\pi)^3 \sum_{l''=|l-l'|}^{l+l'} \sqrt{\frac{(2l+1)(2l'+1)(2l''+1)}{4\pi}} \times \begin{pmatrix} l & l' & l'' \\ 0 & 0 & 0 \end{pmatrix} \begin{pmatrix} l & l' & l'' \\ m & m' & m'-m \end{pmatrix} \frac{i^{l''}}{\sqrt{2l''+1}} \times \int k^2 dk \Delta_l(k,\tau')P_\phi(k) j_{l''}(k\,|\Delta\vec{x}|) Y^*_{l'',m'-m}(\Delta\hat{x}) \quad (3.23)$$

In summary, at the same point $\vec{x} = \vec{x}'$, the correlation function is zero with different l, m cases, but at two different points $\vec{x} \neq \vec{x}'$, the correlation function has a value.

3.2 Transfer function of temperature anisotropy

In this section, we will look at the propagation function to specifically calculate CMB temperature anisotropy. The quadrupole, which is the source of polarization of the galaxy cluster, is sufficiently large in scale that the main effects are Sachs-Wolfe (SW) and Integrated Sachs-Wolfe (ISW) effects. Both are caused by the gravitational redshift, but the processes they focus on are different. The SW effect is due to the anisotropy of the fluctuations of the gravitational potential at the last scattering surface. Similarly, the gravitational potential at the observation point is also affected, but in this case there is no direction-dependent anisotropy. The ISW effect occurs when fluctuations in the gravitational potential evolve with redshift. As photons fall into and out of this time-varying potential, they gain and lose energy. That is observed as temperature anisotropy. Consider the transfer function of the SW effect on a large scale. In this case, anisotropy is caused by the potential across the last scattering surface and changes in photon density. With the line-of-sight integration method, the SW temperature anisotropy is calculated

$$\Delta(\vec{x}, \vec{n}, \tau) = \int_0^\tau d\chi' \dot{\zeta}(\tau - \chi') \left[\frac{1}{4}\delta_\gamma(\chi'\hat{n}) + \phi(\chi'\hat{n})\right] \quad (3.24)$$

where χ' is the comoving distance. Also, we use the visibility function defined by $\zeta(\tau) \equiv e^{-\tau_C(\tau)}$, and optical depth of Thomson scattering $\tau_C(\tau) =$

$\int_0^\tau d\chi' a(\tau-\chi')n_e(\tau-\chi')\sigma_T$.
On a large scale the Sachs-Wolfe approximation can be applied, the density fluctuations of photons are $\delta_\gamma = -\frac{8}{3}\phi$, and the potential in Fourier space is $\phi(\vec{k},\tau) = \frac{9}{10}\phi_{\rm ini}(\vec{k})$. In Fourier space

$$\Delta_l(k,\tau) = \frac{3}{10}\int_0^\tau d\chi'\dot{\zeta}(\tau-\chi')j_l(k\chi') \tag{3.25}$$

The visibility function depends on the property of recombination. Assuming recombination occurred instantaneously,

$$\Delta_l(k,\tau) = \frac{3}{10}j_l\left[k(\tau-\tau_r)\right] \tag{3.26}$$

The CMB transfer function with the ISW effect is

$$\begin{aligned}\Delta(\vec{x},\vec{n},\tau) = &\int_0^\tau d\chi'\dot{\zeta}(\tau-\chi')\left[\frac{1}{4}\delta_\gamma(\chi'\hat{n}) + \phi(\chi'\hat{n})\right] \\ &+ \int_0^\tau d\chi'\zeta(\tau-\chi')2\dot{\phi}(\chi'\hat{n})\end{aligned} \tag{3.27}$$

The growth rate of the potential perturbations is described with the growth function $D_+(\tau)$ in the linear theory. In the adiabatic case, the potential becomes $\phi(\vec{k},\tau) = \frac{9}{10}\phi_{\rm ini}(\vec{k})D_+(\tau)/a(\tau)$. When there is only non-relativistic matter and dark energy, the growth function is of the simple form

$$D_+(\tau) = \frac{5}{2}\Omega_m\frac{\sqrt{\Omega_m + \Omega_{\rm DE}a(\tau)^3}}{a(\tau)^{3/2}}\int_0^{a(\tau)}\left[\frac{a'}{\Omega_m + \Omega_{\rm DE}a'^3}\right]^{3/2}da' \tag{3.28}$$

Assuming recombination occurred instantaneously, the CMB transfer function including the ISW effect can be

$$\Delta_l(k,\tau) = \frac{3}{10}j_l\left[k(\tau-\tau_r)\right] + \frac{9}{5}\int_0^{\tau-\tau_r}d\chi' j_l(k\chi')\left.\frac{\partial}{\partial\tau}\frac{D_+}{a}\right|_{\tau-\chi'} \tag{3.29}$$

3.3 Stokes parameter by Thomson scattering

The Stokes parameters are defined as time averages of quadratic products of the amplitudes of the electric field E_i. The electromagnetic wave propagating from the z direction is characterized by the 2×2 matrix $\langle E_i E_j^*\rangle$ with i, j in x-y plane. To generalize for three-dimensional space, we use 3×3 matrix associated with direction $\hat{n}$.

$$Q_{ij}(\vec{n}) = \left\langle E_i E_j^*\right\rangle, \qquad (i,j)\in\{x,y,z\} \tag{3.30}$$

The electric field this polarization matrix shows is always vertical to the propagating direction $\hat{n}$

$$n^i Q_{ij}(\vec{n}) = 0 \tag{3.31}$$

The polarization matrix Q_{ij} is expressed with a superposition of beams with various momenta $\vec{p}$ from various directions n. Using specific intensity matrices I_{ij} as the elements,

$$Q_{ij} = \int dpd\Omega I_{ij}(\vec{p}) \tag{3.32}$$

The Stokes parameter depends on the polarization basis vector. Therefore write the parameters with specific intensity matrices I_{ij} and polarization basis vectors

$$\begin{aligned} \frac{I+Q}{2} &= \epsilon_i^{(1)}\epsilon_j^{(1)}I_{ij}, & \frac{I-Q}{2} &= \epsilon_i^{(2)}\epsilon_j^{(2)}I_{ij} \\ \frac{U+iV}{2} &= \epsilon_i^{(1)}\epsilon_j^{(2)}I_{ij}, & \frac{U-iV}{2} &= \epsilon_i^{(2)}\epsilon_j^{(1)}I_{ij} \end{aligned} \tag{3.33}$$

Conversely, the Stokes parameters can also be used to represent the intensity matrix. In a case $\epsilon^{(1)=x}$, $\epsilon^{(2)=y}$,

$$I_{ij} = \frac{1}{2}\begin{pmatrix} I+Q & U+iV & 0 \\ U-iV & I-Q & 0 \\ 0 & 0 & 0 \end{pmatrix} \tag{3.34}$$

Similarly, if we consider unpolarized light, it has only diagonal components, and only the direction $\hat{n}$ in which it propagates is a special direction. The form of the matrix is

$$I_{ij}(\hat{n}) = A\delta_{ij} + Bn_i - n_j \tag{3.35}$$

For light along the z direction, the matrix is clearly

$$I_{ij} = \frac{I}{2}\begin{pmatrix} 1 & 0 & 0 \\ 0 & 1 & 0 \\ 0 & 0 & 0 \end{pmatrix} \tag{3.36}$$

From these, it follows that for unpolarized light from the direction $\hat{n}$

$$I_{ij}(\hat{n}) = \frac{1}{2}(\delta_{ij} - n_i n_j) \tag{3.37}$$

On the general matrix I_{ij}, the magnitude of polarization is

$$\Pi^2 = 2\mathrm{T_r}\left[\vec{I}^2\right] / \left(\mathrm{T_r}\left[\vec{I}\right]\right)^2 - 1 \tag{3.38}$$

Consider a perfectly linearly polarized incident light and the polarization matrix produced by Thomson scattering on a stationary electron. Then $Q_{ij}\epsilon_i^*\epsilon_j$ is the energy density of the electromagnetic wave. Let the polarization vector of the incident light be ϵ and the momentum be $\vec{p}$. The differential cross section of Thomson scattering in the Thomson limit, where the final momentum is $\vec{p'} = p'\vec{n}'$ and the polarization is ϵ', is

$$\frac{d\sigma}{d\Omega'} = \frac{3\sigma_T}{8\pi}\left|\vec{\epsilon}^* \cdot \vec{\epsilon}'\right|^2 \tag{3.39}$$

where $d\Omega'$ is the solid angle element for the direction $\vec{n}'$ of the scattered photons. From this, the power per solid angle is

$$\frac{dP'}{d\Omega'} = \frac{3\sigma_T}{8\pi}\left|\vec{\epsilon}^* \cdot \vec{\epsilon}'\right|^2 \tag{3.40}$$

Consider a set of stationary electrons of number density ne in a galaxy cluster. The temperature of the galaxy cluster is sufficiently low relative to the mass of the electrons that the thermal motion of the electrons can be neglected. Assuming that multiple scattering does not occur, we can convert the scattered power per electron to a change in energy density.

$$\frac{dQ'_{ij}}{d\Omega'} = \frac{3\sigma_T}{8\pi}n_e Q_{ij}\epsilon_i'^*\epsilon'_j d\Omega' \tag{3.41}$$

where Q'_{ij} is the polarization matrix after scattering. Assuming that photon momentum is conserved $p = p'$

$$\frac{dI_{ij}}{dt}\epsilon_i'^*\epsilon'_j = \frac{3\sigma_T}{8\pi}n_e\epsilon_i'^*\epsilon'_j\int d\Omega I_{ij} \tag{3.42}$$

Because the polarization of the incident wave and the polarization of the scattered wave are not in the same plane, we can't make the relation $dI'_{ij} \propto \Omega I_{ij}$ The momentum vector p' of the scattered light and the polarization basis vector ϵ'_1, ϵ'_2 are orthogonal, and only the components on the polarization basis vector $\epsilon'_1 - \epsilon'_2$ plane after this scattering are projected from the incident light. The matrix representing the projection is

$$P_{ij}(\vec{n}') \equiv \delta_{ij} - n'_i n'_j \tag{3.43}$$

The projection vector$P_{ij}(n')$ does not change the polarization vector. By operating on Eq.(3.42)

$$\frac{dI'_{ij}(\vec{n}')}{dt} = \frac{3\sigma_T}{8\pi}n_e P_{ik}(\vec{n}')P_{jl}(\vec{n}')\int d\Omega I_{kl}(\vec{n}) \tag{3.44}$$

This equation shows that the scattered light is proportional to the incident light minus the component in the n' direction. By the time integral, we obtain the polarization matrix of the scattering

$$I'_{ij}(\vec{n}') = \frac{3\sigma_T}{8\pi}P_{ik}(\vec{n}')P_{jl}(\vec{n}')\int d\Omega I_{kl}(\vec{n}) \tag{3.45}$$

where we replace $\sigma_T n_e$ to the optical depth of Thomson scattering. In case the incident light is unpolarized, using the matrix in Eq.(3.37)

$$I'_{ij}(\vec{n}') = \frac{3\sigma_T}{16\pi}P_{ik}(\vec{n}')P_{jl}(\vec{n}')\int d\Omega I(\vec{n})P_{kl}(\vec{n}) \tag{3.46}$$

3.4 Polarization of galaxy clusters

Here we consider the process of polarization generation by Thomson scattering CMB quadrupole on a galaxy cluster in an ideal case such as galaxy clusters are regarded as point objects with optical depth τ_C. The Stokes parameters of the radiation scattered by the cluster depend on the quadrupole anisotropy in the local CMB radiation at the cluster. The quadrupole is written in the coefficients $a_{2m}(\vec{x})$ of the spherical harmonic expansion of the temperature anisotropy, which are functions of the cluster position $\vec{x}$. The brightness temperature of the CMB radiation from the direction vector $\hat{n}$ at the cluster position $\vec{x}$ can be written in terms of the spherical harmonic expansion coefficients $a_{lm}(\vec{x})$.

$$I(\hat{n}, \vec{x}) = T_{\rm CMB}(\tau)\sum_{l=0}^{\infty}\sum_{m=-l}^{l} a_{lm}(\vec{x})Y_{lm}(\hat{n}) \tag{3.47}$$

Here we assume that the CMB radiation observed at the cluster position is unpolarized. In the Thomson limit, the brightness temperature polarization matrix $I_{ij} \sim \langle E_i E_j \rangle$ is described as

$$I_{ij}(\vec{x}) = \frac{3\tau_C}{16\pi}(\delta ik - \hat{x}_i\hat{x}_k)(\delta_{jl} - \hat{x}_j\hat{x}_l)\int d\Omega' I(\hat{n}, \vec{x})(\delta_{kl} - \hat{n}_k\hat{n}_l) \tag{3.48}$$

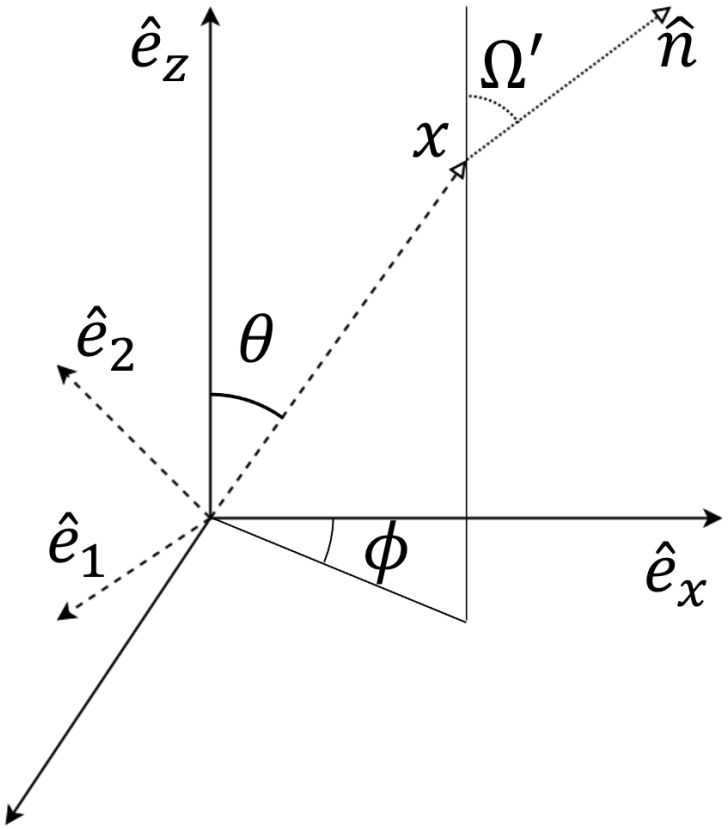

Figure 3.2: Coordinate system for the process of polarization generation by Thomson scattering. The observer is taken as the origin, and there is a galaxy cluster causing scattering at position x. Furthermore, before the galaxy cluster scattering, CMB photons are propagating from any direction, denoted by $\hat{n}$ and its solid angle is Ω. The incident light here is assumed to be unpolarized, and only the l=2 component in the spherical harmonic decomposition contributes to polarization. The radiation scattered by the free electrons in the galaxy cluster is observed by the observer in the direction of the cluster $\hat{x}$. The polarization basis vector is defined as $\hat{e}_1$, $\hat{e}_2$ on the plane perpendicular to the cluster position vector χ^2 and is used in the Stokes parameters.

where Ω' is the solid angle about the $\hat{n}$. To define the Stokes parameters at the observer, we define a polarization basis $\hat{e}_1$, $\hat{e}_2$. The Stokes parameters are

$$\begin{aligned} I(\vec{x}) + Q(\vec{x}) &= 2I_{ij}(\vec{x})\hat{e}_{1,i}\hat{e}_{1,j} \\ I(\vec{x}) - Q(\vec{x}) &= 2I_{ij}(\vec{x})\hat{e}_{2,i}\hat{e}_{2,j} \\ U(\vec{x}) &= 2I_{ij}(\vec{x})\hat{e}_{1,i}\hat{e}_{1,j} \end{aligned} \tag{3.49}$$

The linearly polarized component $Q(\vec{x})$, $U(\vec{x})$ is written as

$$Q(\vec{x}) = \frac{3\tau_C}{16\pi} T_{\mathrm{CMB}}(\tau) \sum_{lm} a_{lm}(\vec{x}) \int d\Omega' Y_{lm}(\hat{n}) \left[(\hat{e}_2 \cdot \hat{n})^2 - (\hat{e}_1 \cdot \hat{n})^2 \right] \tag{3.50}$$

$$U(\vec{x}) = -\frac{3\tau_C}{8\pi} T_{\mathrm{CMB}}(\tau) \sum_{lm} a_{lm}(\vec{x}) \int d\Omega' Y_{lm}(\hat{n}) (\hat{e}_1 \cdot \hat{n})(\hat{e}_2 \cdot \hat{n}) \tag{3.51}$$

The direction vectors $\hat{n}$, $\hat{x}$ in the Cartesian coordinate are written as

$$\hat{n} = (\hat{n}_x, \hat{n}_y, \hat{n}_z) = (\sin\theta'\cos\phi', \sin\theta'\sin\phi', \cos\theta') \tag{3.52}$$

$$\hat{x} = (\hat{x}_x, \hat{x}_y, \hat{x}_z) = (\sin\theta, \cos\phi, \sin\theta\sin\phi, \cos\theta) \tag{3.53}$$

For convenience, we use $(z_1, z_2, z_3) = (\sin\theta' e^{i\phi'}, \sin\theta' e^{-i\phi'}, \cos\theta')$. In this form, $\hat{n} = [(z_1 + z_2)/2, (z_1 + z_2)i/2, z_3]$. Also we define

$$\hat{e}_+ \equiv \hat{e}_x + i\hat{e}_y \tag{3.54}$$

$$\hat{e}_- \equiv \hat{e}_x - i\hat{e}_y \tag{3.55}$$

The inner products can be calculated as

$$\hat{e}_1 \cdot \hat{n} = \frac{z_1}{2}\hat{e}_1 \cdot \hat{e}_- + \frac{z_2}{2}\hat{e}_1 \cdot \hat{e}_+ + z_3\hat{e}_1 \cdot \hat{e}_z \tag{3.56}$$

On the other hand, the spherical harmonic functions for quadrupole components are

$$\begin{aligned} Y_{2,0}\sqrt{\frac{5}{4\pi}}\left(\frac{3}{2}z_3^2 - \frac{1}{2}\right) \\ Y_{2,1} = -\sqrt{\frac{15}{8\pi}}z_1 z_3, \qquad Y_{2,-1} = \sqrt{\frac{15}{8\pi}}z_2 z_3 \\ Y_{2,2} = \frac{1}{4}\sqrt{\frac{15}{2\pi}}z_1^2, \qquad Y_{2,-2} = \frac{1}{4}\sqrt{\frac{15}{2\pi}}z_2^2 \end{aligned} \tag{3.57}$$

Expressing the inner product in Eq.(3.51) using the spherical harmonic function

$$(\hat{e}_2 \cdot \hat{n})^2 - (\hat{e}_1 \cdot \hat{n})^2 = \sqrt{\frac{8\pi}{5}} \sum_{m=-2}^{2} Q_m(\hat{x}) Y_{2,m}(\hat{n}) \tag{3.58}$$

$$-2(\hat{e}_1 \cdot \hat{n})(\hat{e}_2 \cdot \hat{n}) = \sqrt{\frac{8\pi}{5}} \sum_{m=-2}^{2} U_m(\hat{x}) Y_{2,m}(\hat{n}) \tag{3.59}$$

Where the coefficients Q_m, U_m are functions of polarization basis vectors. Therefore, it has the position of the galaxy cluster as an argument.

$$\begin{aligned} Q_0(\hat{x}) = -\frac{1}{\sqrt{2}}\left[(\hat{e}_1 \cdot \hat{e}_z)^2 - (\hat{e}_2 \cdot \hat{e}_z)^2\right] \\ Q_1(\hat{x}) = \frac{1}{\sqrt{3}}\left[(\hat{e}_- \cdot \hat{e}_1)(\hat{e}_z \cdot \hat{e}_1) - (\hat{e}_- \cdot \hat{e}_2)(\hat{e}_z \cdot \hat{e}_2)\right] \\ Q_2(\hat{x}) = \frac{1}{2\sqrt{3}}\left[(\hat{e}_- \cdot \hat{e}_2)^2 - (\hat{e}_- \cdot \hat{e}_1)^2\right] \end{aligned} \tag{3.60}$$

$$\begin{aligned} U_0(\hat{x}) = -\sqrt{2}(\hat{e}_1 \cdot \hat{e}_z)(\hat{e}_2 \cdot \hat{e}_z) \\ U_1(\hat{x}) = \frac{1}{\sqrt{3}}\left[(\hat{e}_- \cdot \hat{e}_1)(\hat{e}_z \cdot \hat{e}_2) + (\hat{e}_- \cdot \hat{e}_2)(\hat{e}_z \cdot \hat{e}_1)\right] \\ U_2(\hat{x}) = -\frac{1}{\sqrt{3}}(\hat{e}_- \cdot \hat{e}_1)(\hat{e}_- \cdot \hat{e}_2) \end{aligned} \tag{3.61}$$

With negative m, the coefficients have relations

$$Q_{-m}(\hat{x}) \equiv (-1)^m Q_m^*(\hat{x}), \qquad U_{-m}(\hat{x}) \equiv (-1)^m U_m^*(\hat{x}) \tag{3.62}$$

Here we choose particular polarization basis vectors defined as

$$\hat{e}_1 = \frac{\hat{x} \times \hat{e}_z}{\sqrt{1-\mu^2}}, \qquad \hat{e}_2 = \frac{\hat{e}_z - \mu\hat{x}}{\sqrt{1-\mu^2}} \tag{3.63}$$

where we define $\mu \equiv \hat{x} \cdot \hat{e}_z = \cos\theta$. On this basis, each component of the coefficients is written with polar coordinates

$$Q_0(\hat{x}) = \frac{1}{\sqrt{2}}\sin^2\theta, \qquad Q_1(\hat{x}) = \frac{1}{\sqrt{3}}\cos\theta\sin\theta e^{-i\phi}$$
$$Q_2(\hat{x}) = \frac{1}{2\sqrt{3}}(1+\cos^2\theta)e^{-2i\phi} \tag{3.64}$$

$$U_0(\hat{x}) = 0, \qquad U_1(\hat{x}) = \frac{i}{\sqrt{3}}\sin\theta e^{-i\phi}$$
$$U_2(\hat{x}) = \frac{i}{\sqrt{3}}\cos\theta e^{-2i\phi} \tag{3.65}$$

where θ is the angle between $\hat{x}$ and $\hat{e}_z$ and ϕ is the angle between the projected $\hat{x} : (\hat{e}_x, \hat{e}_y)$ and $\hat{e}_x$. Also, Q_m and U_m are associated using spherical harmonic functions

$$Q_m + iU_m = \frac{4}{3}\sqrt{\frac{3\pi}{5}}{}_2Y^*_{2m}(\theta,\phi) \tag{3.66}$$

From Eq.(3.51), the Stokes parameter of the observed polarization is the sum of all m-modes.

$$Q(\vec{x}) = \tau_C P_0 \sum_{m=-2}^{2} Q_m(\hat{x}) a_{2m}(\vec{x}) \tag{3.67}$$

$$U(\vec{x}) = \tau_C P_0 \sum_{m=-2}^{2} U_m(\hat{x}) a_{2m}(\vec{x}) \tag{3.68}$$

where $P_0 \equiv 3/(4\sqrt{10\pi})T_{\rm CMB}(\tau)$. Summarizing as Eq.(3.66).

$$Q(\vec{x}) \pm iU(\vec{x}) = -\frac{\sqrt{6}}{10}\tau_C T_{\rm CMB}(\tau) \sum_{m=-2}^{2} {}_{\pm2}Y_{2m}(\hat{x}) a_{2m}(\vec{x}) \tag{3.69}$$

Chapter 4

Validation method for dark energy models using CMB

4.1 Galaxy cluster polarization simulation

The following is the procedure for simulation and analysis in this method. In this simulation, we use transfer functions generated by the publicly available code CAMB. We use Λ-CDM model with $\Omega_b h^2 = 0.0226$, $\Omega_c h^2 = 0.112$, $\Omega_\nu h^2 = 0.00064$, $h = 0.7$, $A_s = 2.1$ and $n_s = 0.96$ as the reference correct cosmological models.

The first step is to generate the initial fluctuation field $\phi_{\rm ini}(k_i)$. Here, polar coordinates are employed in Fourier space, and a Gaussian is used to reproduce the initial fluctuations so that they fit the power spectrum $P_\phi(k)$.

$$P_\phi(k) = A_s \left(\frac{k}{k_*}\right)^{n_s - 1} \tag{4.1}$$

The direction is divided by Healpix with $N_{\rm side} = 8$, and this means that the whole sky is divided into 768 sections. The line-of-sight direction is also expressed in 60 wavenumber modes, with a range from $k = 10^{-5}$ to 10^{-1}. Thus, the overall independent Fourier moden_k for this simulation is 46080.
Second, we simulate the polarization $Q_{\rm fiducial}(x_i)$, $U_{\rm fiducial}(x_i)$ produced by each galaxy cluster from the initial fluctuations $\phi_{\rm ini}(k_i)$. In this process, we use the transfer function $\Delta(k, \tau)$ with the correct cosmological parameters as a reference. Fig.4.1 4.3 shows the Q and U maps in a realization.

Here we use randomly placed clusters of galaxies $N_{\rm cluster} = 6000$, distributed uniformly in the angular direction and with redshifts ranging from $z = 0$ to 2. Fig.4.4 shows the region that construct the polarization of these galaxy clusters.

Similarly, we simulate the CMB directly observed at the origin, which is the observation point from the initial fluctuation. Both the temperature fluctuation and the polarization component, E-mode, are calculated from $l = 2$ to 9. Only the l=2 component of the temperature fluctuation ${a_{2m}^T}^{\rm true}$ is used to measure the statistical power at the end.
Next, the initial fluctuations are reconstructed. Specifically, we fit the polarization $Q(x_i)$, $U(x_i)$ produced by the cluster of galaxies and the CMB a_{lm}^T, a_{lm}^E directly observed at the origin. The minimize function is given as

$$f_{\rm tot} = f_{\rm pol} + f_T + f_E + f_{\rm prior} \tag{4.2}$$

This function has four components, in order: the chi-square minimizations for the polarization of the galaxy cluster $Q(x_i)$, $U(x_i)$, the temperature anisotropy of the

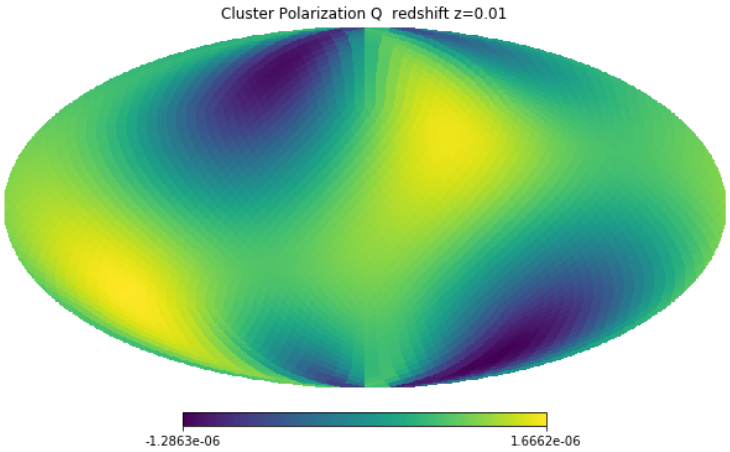

Figure 4.1: Q polarization map observed from a galaxy cluster at redshift 0.01. Because they are produced by quadrupoles that are nearly identical to the quadrupoles we observe, they have a pattern similar to that of quadrupoles.

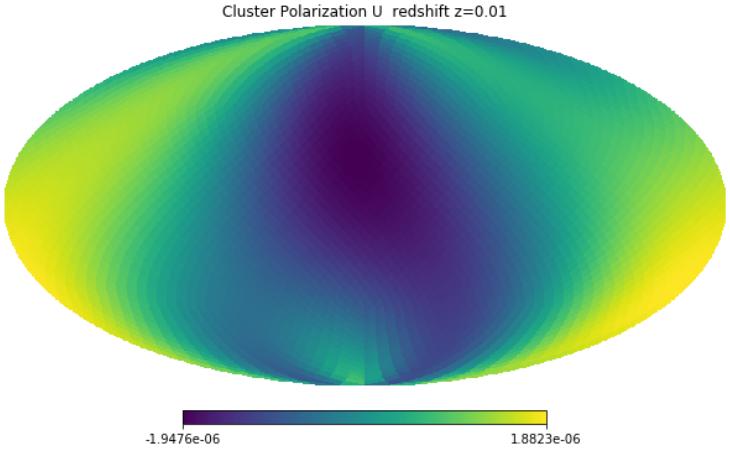

Figure 4.2: U polarization map observed from a galaxy cluster at redshift 0.01

CMB a^T_{lm} and the polarization anisotropy of the CMB a^E_{lm}, and the prior. The fiducial value in the function represents the observable obtained in the previous step with Gaussian noise, which is equivalent to errors in the observation.

$$f_{\rm pol} = \sum_{i}^{N_{\rm cluster}} \left[\frac{(Q(x_i) - Q_{\rm fiducial}(x_i))^2}{2{\sigma^2}_{\rm pol}} + \frac{(U(x_i) - U_{\rm fiducial}(x_i))^2}{2{\sigma^2}_{\rm pol}} \right] \tag{4.3}$$

where $\sigma_{\rm pol}$ is the uncertainty of the polarization observation.
We use CMB temperature anisotropy from $l = 3$ to 9 for fitting

$$f_T = \sum_{l=3} \sum_{m=-l}^{l} \frac{(a^T_{lm} - a^T_{lm\,\rm fiducial})^2}{\sigma^2_T} \tag{4.4}$$

For E mode, $l = 2$ mode is also added to the fitting function

$$f_E = \sum_{l=2} \sum_{m=-l}^{l} \frac{(a^E_{lm} - a^E_{lm\,\rm fiducial})^2}{\sigma^2_E} \tag{4.5}$$

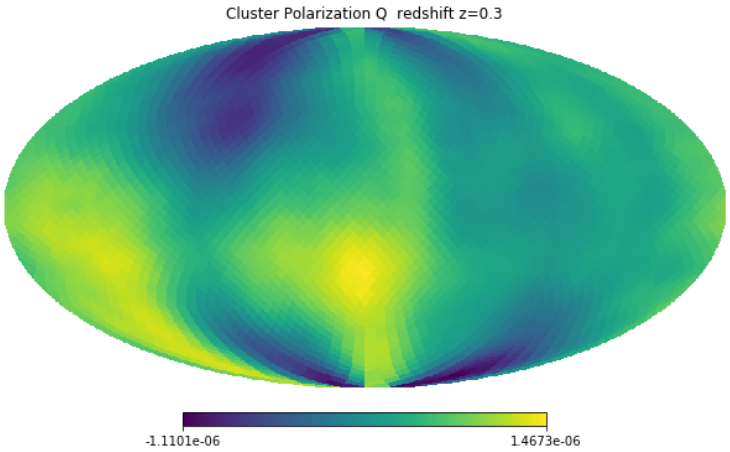

Figure 4.3: Q polarization map observed from a galaxy cluster at redshift 0.1. While maintaining features similar to the map at $z = 0.3$, smaller patterns develop.

All these components are calculated from the initial fluctuations $\phi_{\rm ini}(k_i)$. Therefore, in actual observations, $Q_{\rm fiducial}(x_i)$, $U_{\rm fiducial}(x_i)$, $a^T_{lm\rm fiducial}$ and $a^E_{lm\rm fiducial}$ is the observed quantity, and we can search for the initial fluctuations$\phi_{\rm ini}(k_i)$ in the actual universe by reproducing $Q(x_i)$, $U(x_i)$, a^T_{lm} and a^E_{lm} that fits to fiducial observable.
To improve the accuracy of the reconstruction we also adopt a Gaussian prior based on power spectrum $P_\phi(k)$.

$$f_{\rm prior} = \sum_j^{n_k} \frac{R^2_{\rm ini}(k_j)}{2P(k_j)} \tag{4.6}$$

In this process, the transfer functions are used to calculate the observable from the initial fluctuations $\phi_{\rm ini}(k_i)$. Since the transfer function depends on the cosmological parameters, different cosmologies lead to different estimates of the initial fluctuations. In this work, we estimate the initial fluctuations with several dark energy state parameters w in order to verify the statistical power for the dark energy state parameter. Fig.4.5 shows the quadrupole transfer functions with different dark energy state parameters.
We calculate the $l = 2$ mode temperature anisotropy ${a^T_{2m}}^{\rm est}(0)$ observed at the origin using the estimated initial fluctuations and compare it to the true value ${a^T_{2m}}^{\rm true}(0)$ calculated before. Up to this point, the method has been applied to a single universe. The sequence of steps is repeated one hundred times from the generation of the initial fluctuations and makes one hundred pairs of ${a^T_{2m}}^{\rm true}(0)$ and ${a^T_{2m}}^{\rm est}(0)$.
The generated ${a^T_{2m}}^{\rm true}(0)$ and ${a^T_{2m}}^{\rm est}(0)$ pairs should agree within statistical error if they are generated using the same transfer function. In application to actual observations, the cosmological parameters of the transfer function used in the estimation process should match those of the actual universe. Thus, the larger the difference between pairs generated using different transfer functions, the more effective the method is able to constrain the cosmological parameters.

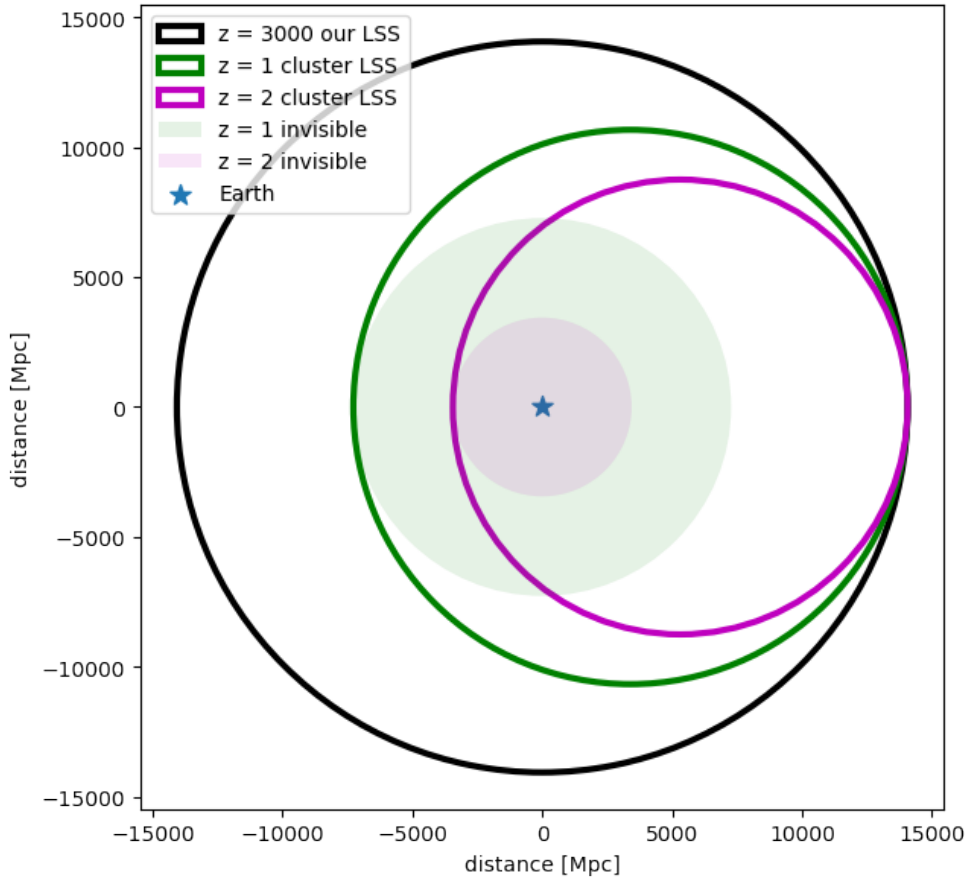

Figure 4.4: This figure shows the observable region in the co-moving coordinate. The largest solid circle shows the last scattering surface that we can directly observe. The other two solid circles show the last scattering surfaces seen from clusters at redshifts $z = 1$ and $z = 2$ on our light cone. Since we observe the polarization produced by the scattering of the CMB from these last scattering surfaces by the galaxy clusters, we can obtain information about the interior of the light cone through polarization that we cannot observe directly. At a given redshift, the last scattering surface is a spherical shell, assuming that there are clusters of galaxies in all directions. The shaded region is the interior of the spherical shell and represents the region that cannot be surveyed only by clusters at each redshift. To survey the entire Universe down to our nearest neighbor, a cluster of galaxies at redshift $z \sim 3$ would be required.

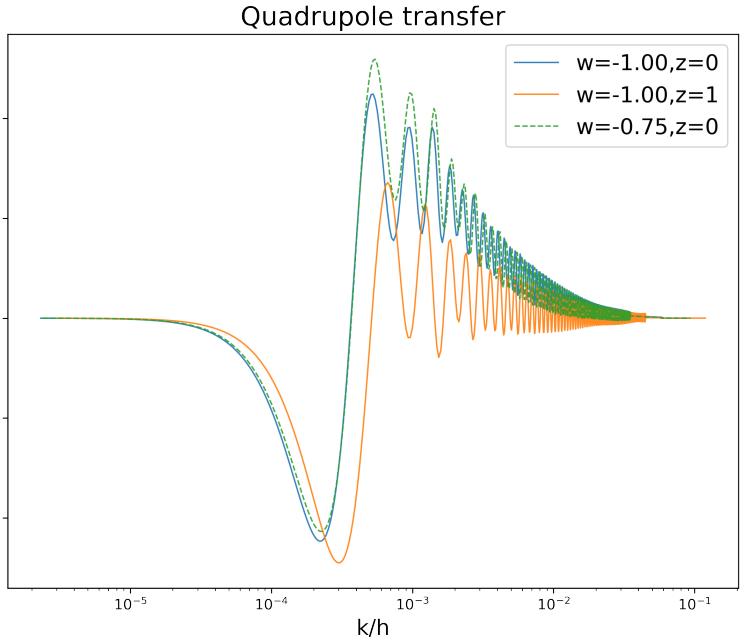

Figure 4.5: The quadrupole transition function of the CMB temperature anisotropy. The solid line shows the quadrupole transfer function for the correct dark energy equation of state parameters, and the dashed line shows it for the wrong $w = -0.75$ parameters. The horizontal axis is the wavenumber of the initial fluctuation, and the right side is the smaller scale.The solid orange line also shows the transfer function at redshift $z = 1$ with the correct parameters, reflecting the overall smaller-scale fluctuations. This corresponds to the fact that high-redshift clusters have smaller last scattering surfaces. The dashed lines with larger equation of state parameters for dark energy have larger values than the solid blue lines at the same redshift. This is due to the fact that the dark energy dominated era begins at higher redshifts and is more strongly affected by ISW effects. However, to make it easier to see, the dashed lines have even larger values of the parameters than those used in the simulation.

4.2 Cosmic variance

In linear perturbation theory, large scale fluctuations can be expressed as the product of initial fluctuations and transfer functions in each scale. Since there is no statistical uncertainty in the transfer function $\Delta_l(k, \tau)$, the power spectrum of the CMB temperature fluctuation is proportional to the square of the initial fluctuation. Suppose that the initial fluctuations $\phi_{\rm ini}(\vec{k})$ are given by a normal distribution (gaussian) with mean 0 and variance σ^2. Since the power spectrum follows a chi-square distribution, the expected value is $n\sigma^2$ and the variance is $2n\sigma^4$ with a degree of freedom n (n independent samples). Since the degrees of freedom at the angular scale l is $2l + 1$, its expected value and variance are $(2l + 1)\sigma^2$, $2(2l + 1)\sigma^4$, respectively. This variance is called the cosmic variance, and its standard deviation is proportional to $\sqrt{2(2l + 1)}\sigma^2$. Dividing the expected value by the standard deviation gives the signal-to-noise ratio $\sqrt{(2l + 1)/2}$. Observational noise is not considered here, this considers only statistical uncertainty.

$$\frac{C_l}{\Delta C_{l\ \text{(cosmic variance)}}} = \sqrt{\frac{(2l+1)}{2}} \tag{4.7}$$

At large scales, this signal-to-noise ratio becomes very small. In the case of $l = 2$, it is just 2.5, which can not provide a strong constraint on cosmology.

In this method using galaxy cluster polarization, there is no statistical uncertainty in the process of connecting initial fluctuations and observables. Therefore, unlike the power spectrum, the initial fluctuation can be obtained directly and is not disturbed by the cosmic variance arising from the statistical uncertainty.

4.3 Statistical power for dark energy equation of state parameters

The accuracy of this method depends on factors such as errors in polarization measurements, the number of galaxy clusters, the optical depth of the clusters, and the redshift errors of the clusters. In this study, we assume the most ideal conditions, where the polarization measurement error and optical depth of the clusters are uniformly $\sigma_{\rm pol}/\tau = 10^{-2}$ μK, and the redshift error is negligible. The number of clusters used is assumed to be 6000 and randomly distributed. The error for the CMB all-sky observation also uses $\sigma_T = \sigma_E = 10^{-2}$ μK. The methodological statistical uncertainty in this method is a complex mixture of factors and is calculated from the reconstruction error in the pair when the correct transfer function is used in the simulation.

$$\sigma^2_{\rm method} = \frac{1}{N}\sum_{i=1}^{N}\frac{1}{5}\left[|\Delta a^T_{20\ i}|^2 + 2|\Delta a^T_{21\ i}|^2 + 2|\Delta a^T_{22\ i}|^2\right] \tag{4.8}$$

where N refers to the number of simulations used, and each Δa_{2m} are difference of pairs ${a^T_{2m}}^{\rm true}(w=-1) - {a^T_{2m}}^{\rm est}(w=-1)$ In the setting of this simulation with $N_{\rm cluster} = 6000,\ \sigma_{\rm pol} = 10^{-2}$ μK, $\mathrm{N_{side}} = 8\mathrm{and}\mathrm{n_{kmode}} = 60$, the methodological statistical uncertainty is

$$\sigma_{\rm mehthod} \simeq 4.0 \times 10^{-8} \tag{4.9}$$

Almost the same values were obtained even when not including all-sky CMB observations of temperature fluctuations and polarization. As shown in Fig.4.6, the quadrupole temperature fluctuations are almost perfectly recovered, and the residuals in each mode are distributed without bias as Fig.4.7.

In future observations, LiteBIRD, the next-generation CMB satellite observation, is planned. In future observations, LiteBIRD, the next-generation CMB satellite observation, is planned. Its detection sensitivity is ~ 2.0 μK arcmin, and the sensitivity for the quadrupole component used in this verification is

$$\sigma^{\rm LiteBIRD}_{l=2} \simeq \frac{2.0}{5700} \simeq 3.7 \times 10^{-4}\ \mu{\rm K} \tag{4.10}$$

where we treat a quadrupole size as $90^\circ = 5400$ arcmin. When made dimensionless by CMB temperature 2.725×10^6 μK, the sensitivity is 1.4×10^{-10}. Thus, the variance in the quadrupole observations of the CMB is sufficiently smaller than the methodological statistical uncertainty to not directly limit this method. This means that the accuracy of the observation of the polarization and optical depth of the galaxy clusters is a limitation of this method.

4.4 Constraints on the dark energy parameter w

The chi-square statistic for the quadrupole is defined as

$$\chi^2(w) = \frac{1}{\sigma^2_{\rm method}}\left(|\Delta a^T_{20}|^2 + 2|\Delta a^T_{21}|^2 + 2|\Delta a^T_{22}|^2\right) \tag{4.11}$$

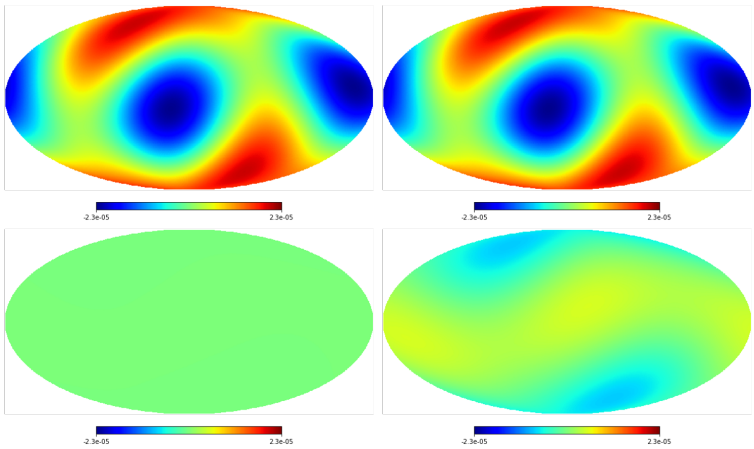

Figure 4.6: Restoration of quadrupole temperature fluctuation. The upper left represents the correct quadrupole temperature fluctuation, and the upper right represents the quadrupole temperature fluctuation reconstructed using fiducial cosmology. The lower left figure shows the residual, and the lower right figure is multiplied by 100 for clarity.

where $\Delta a_{2m} = a_{2m}^{T\,\mathrm{est}}(w) - a_{2m}^{T\,\mathrm{true}}(w=-1)$. While the $m=0$ component is a real number, the $m=1,2$ components are complex numbers, so the independent components are doubled, requiring a factor of 2 on the right side.
The chi-square is a measure of the goodness of fit between the correct cosmological model and the model used for estimation. If the correct model is used in the estimation as well, it ideally follows the chi-square distribution with a degree of freedom of five. The chi-square values are larger when different models are used in the estimation process. In other words, the cosmological parameters can be varied and the cosmology can be restricted by comparing the differences in the chi-square values $\Delta\chi^2(w) = \chi^2(w) - \chi^2(w=-1)$. In the previous study, only the polarization of the galaxy clusters was used in the fitting process to reconstruct the initial fluctuations. In this study, we investigate the change in statistical power for the dark energy equation of state parameter by adding temperature anisotropy and polarization in the all-sky CMB observations. Fig.4.8 shows the $l=2$ and $l=3$ transfer functions and Fig.4.9 compares the transfer functions for E-mode and temperature anisotropy.

We set the true equation-of-state parameters of dark energy $w=-1$. Correlation coefficients between the true and estimated quadrupoles for each realization of the simulation are shown in Fig.4.10. For almost all realizations, the quadrupole with the correct parameters recovers a quadrupole closer to the true quadrupole, and this shows that the parameters can be verified from a comparison of the observed and estimated quadrupoles.
Also, their errors for each realization of the simulation are shown in Fig.4.11. The case ($w=-1$) corresponds to the methodological statistical uncertainty used in the analysis. This difference is the statistical power in the validation of the parameters.

The histograms of the residuals of the temperature fluctuations when w = -0.99 was verified are shown in Fig.4.12 and Fig.4.13. The residual of w = -0.99 is slightly larger than in the fiducial case. This trend is stronger when all-sky CMB observations are added, indicating an improvement in the method.

The difference in chi-square values for $w=-0.99$ is $\langle\chi^2(w=-0.99)\rangle = 1.14, 1.16$, and 1.33 respectively only galaxy clusters polarization case, plus E-

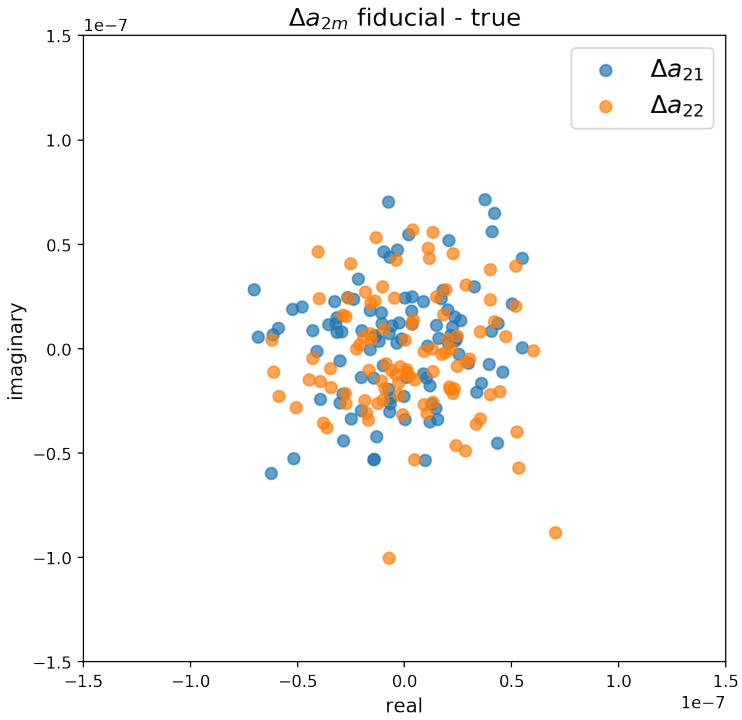

Figure 4.7: The residuals of the recovery with fiducial cosmology in each component of the quadrupole. The horizontal axis indicates the real part and the vertical axis is the imaginary part.

mode polarization, and plus E-mode polarization and temperature anisotropy. As shown in Table.4.1, σmehthod changes little, but $\Delta\chi^2$ improve 16.7%. The histogram of $\Delta\chi^2$ for each realization is shown in Fig.4.14.

Observable	σ_{mehthod}	$\Delta\chi^2$
Only cluster polarization	4.060×10^{-08}	1.137
Cluster polarization + E-mode	4.039×10^{-08}	1.163
Cluster polarization + E&T-mode	4.014×10^{-08}	1.327

Table 4.1: $\Delta\chi^2$ for parameters with $w = -0.99$.

In the case that is a little easier to verify, the histograms of the residuals of the temperature fluctuations when w = -0.95 was verified are shown in Fig.4.15 and Fig.4.16. Compared to w=-099, the residuals are also clearly split, indicating that the assumed cosmological model is incorrect. Also, the increase in the residual of w=-0.95 with the addition of the all-sky CMB observations is also clear.

The difference in chi-square values for $w = -0.95$ is $\langle\chi^2(w = -0.95)\rangle = 16.90, 17.85$, and 19.93 respectively only galaxy clusters polarization case, plus E-mode polarization, and plus E-mode polarization and temperature anisotropy. $\Delta\chi^2$ improves 17.9% with temperature and polarization anisotropy. To summarize the results, for both dark energy equation of state parameters, we obtained larger chi-square values when adding E-mode polarization and temperature anisotropy. This is due to the fact that E-mode polarization and temperature anisotropy in all-sky observations are associated with the polarization produced by galaxy clusters. Thus, combining all-sky CMB observations with the remote quadrupole technique using the polarization of galaxy clusters can more strongly constrain the cosmology.

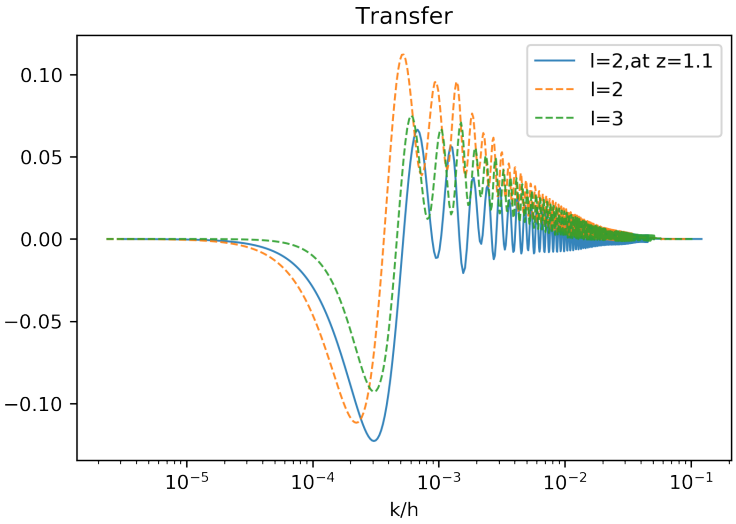

Figure 4.8: Transfer functions for temperature anisotropy at current time z=0 and redshift z=1.1. The dashed lines show the l=2 and 3 components of the transition function at the current time. The octupole l=3, which has more divisions in the whole sky, consists of smaller-scale fluctuations. The past quadrupole l=2, shown by the solid line, depends on smaller scales, which corresponds to a smaller projected universe. Even the same multipole component depends on smaller-scale fluctuations at higher redshifts, and its characteristic scale is closer to the higher-order poles.

Observable	σ_{mehthod}	$\Delta\chi^2$
Only cluster polarization	4.060×10^{-08}	16.90
Cluster polarization + E-mode	4.039×10^{-08}	17.85
Cluster polarization + E&T-mode	4.014×10^{-08}	19.93

Table 4.2: $\Delta\chi^2$ for parameters with $w = -0.95$

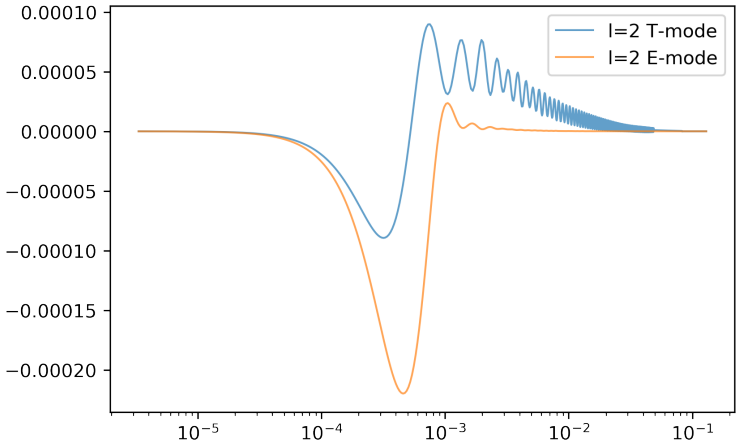

Figure 4.9: Transfer functions in the l=2 component of temperature anisotropy and polarization E-mode. Polarized E-mode requires ionized hydrogen for its generation process, so a characteristic scale appears on a smaller scale than that of temperature anisotropy.

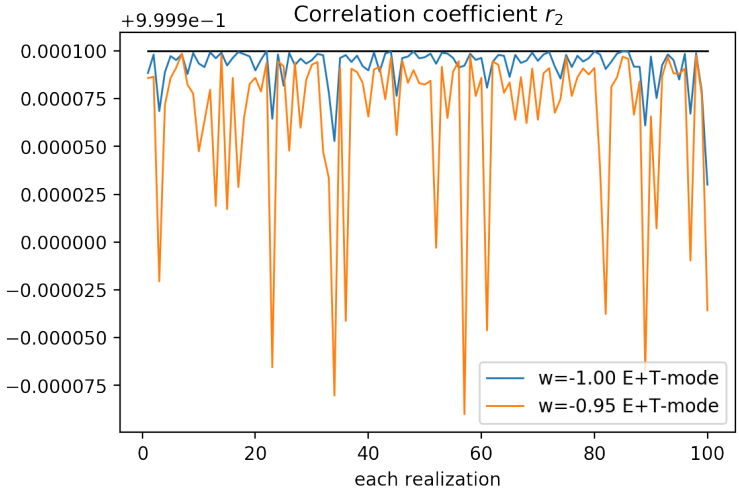

Figure 4.10: Correlation coefficient r_2 between the true quadrupole a2m and the reconstructed quadrupole. $r_2 = \sum_{m=-l}^{l}(a_{2m}^{T\ \mathrm{est}} a_{2m}^{T\ \mathrm{true}})/(\sum(a_{2m}^{T\ \mathrm{est}})^2 \sum(a_{2m}^{T\ \mathrm{true}})^2)^{1/2}$.The horizontal axis represents independent simulations with different distributions of initial fluctuations and galaxy clusters, respectively, and the vertical axis represents dimensionless correlation coefficients with the true quadrupole. The solid blue line shows the correlation coefficients for the realizations with the true dark energy equation of state parameters, while the solid orange line shows the case with the wrong parameters.

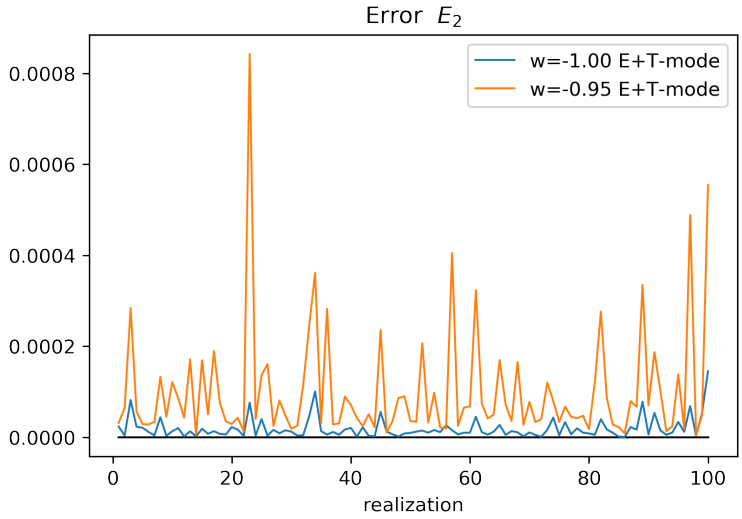

Figure 4.11: Variance of the reconstructed quadrupole. $E_2 = \sum_{m=-l}^{l}(a_{2m}^{T\ \mathrm{est}} - a_{2m}^{T\ \mathrm{true}})^2 / \sum(a_{2m}^{T\ \mathrm{true}})^2$ The horizontal axis represents different independent simulations of the initial fluctuations and the distribution of galaxy clusters, respectively, and the vertical axis represents the dispersion from the true quadrupole at each realization. The solid blue line shows the variance when reconstructed using the true dark energy equation of state parameters. The solid orange line shows the case with the wrong parameters.

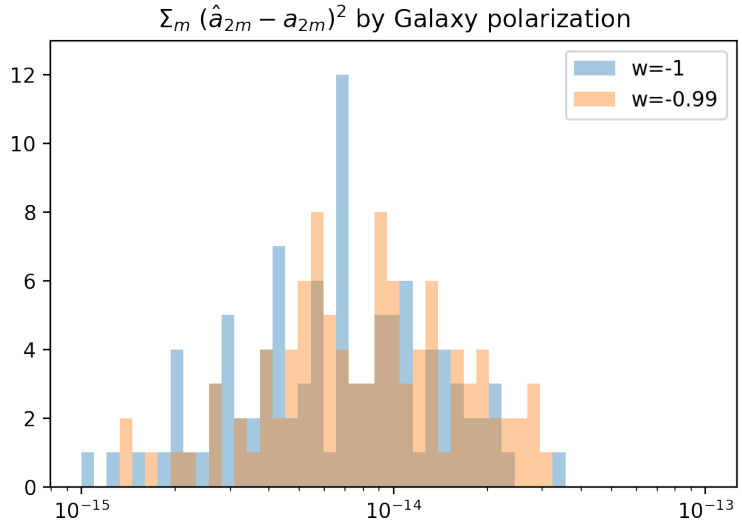

Figure 4.12: Histogram of residuals with respect to the true quadrupole temperature fluctuations for the case with galaxy cluster polarization, temperature fluctuation higher-order multipoles and E-mode polarization fluctuation multipoles. Blue and orange represent the fiducial cosmological model ($w = -1$) and $w = -0.99$, respectively.

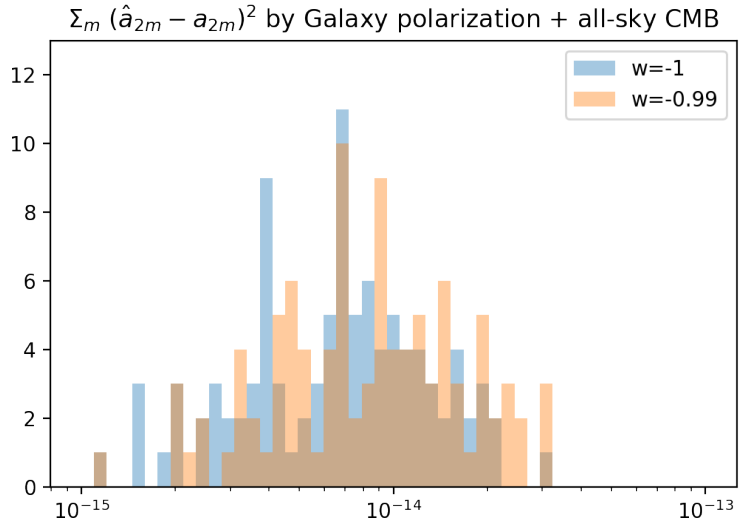

Figure 4.13: Histogram of residuals with respect to the true quadrupole temperature fluctuations for the case with galaxy cluster polarization and . Blue and orange represent the fiducial cosmological model ($w = -1$) and $w = -0.99$, respectively.

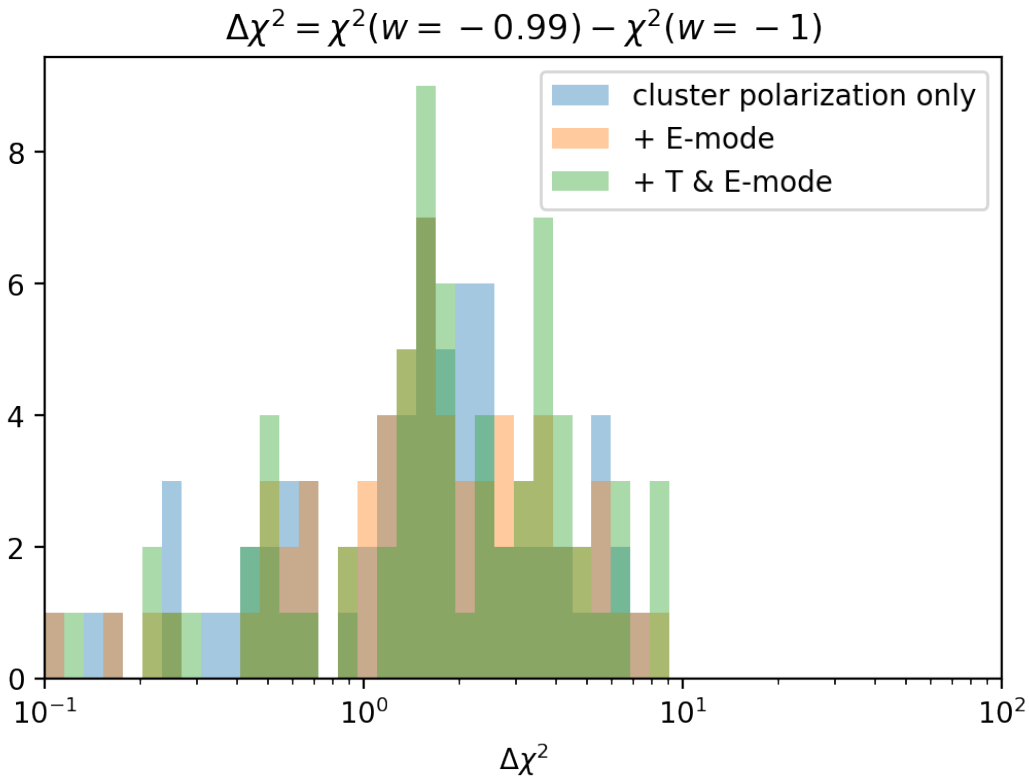

Figure 4.14: Distribution of the difference of the chi-square statistic for the 100 simulations at w = -0.99. Each color shows the case of fitting using only the polarization of the galaxy cluster, the case of fitting adding the E-mode of the all-sky CMB observations, and the case of also adding temperature anisotropy.

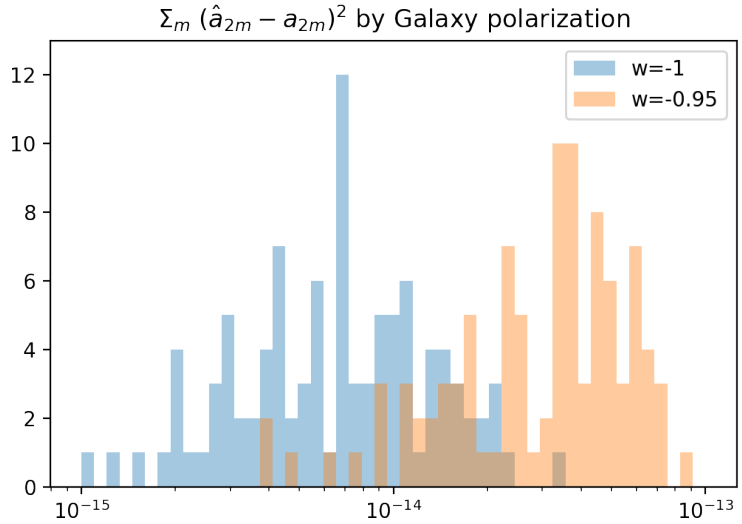

Figure 4.15: Histogram of residuals with respect to the true quadrupole temperature fluctuations for the case with galaxy cluster polarization, temperature fluctuation higher-order multipoles and E-mode polarization fluctuation multipoles. Blue and orange represent the fiducial cosmological model ($w = -1$) and $w = -0.95$, respectively.

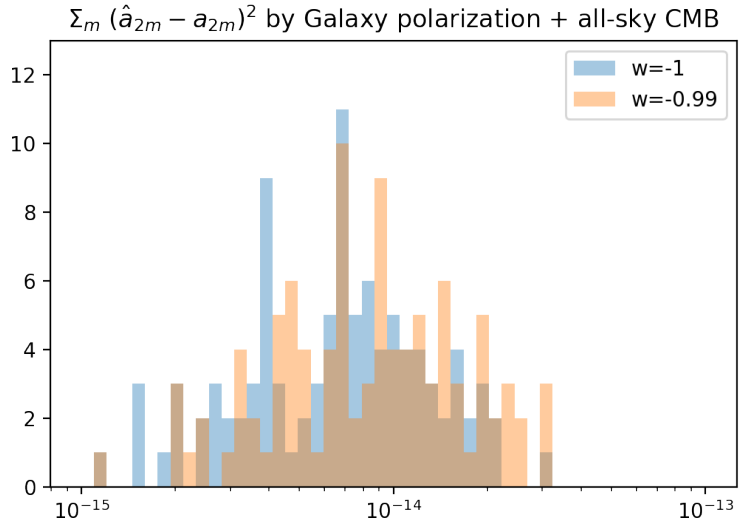

Figure 4.16: Histogram of residuals with respect to the true quadrupole temperature fluctuations for the case with galaxy cluster polarization and . Blue and orange represent the fiducial cosmological model ($w = -1$) and $w = -0.99$, respectively.

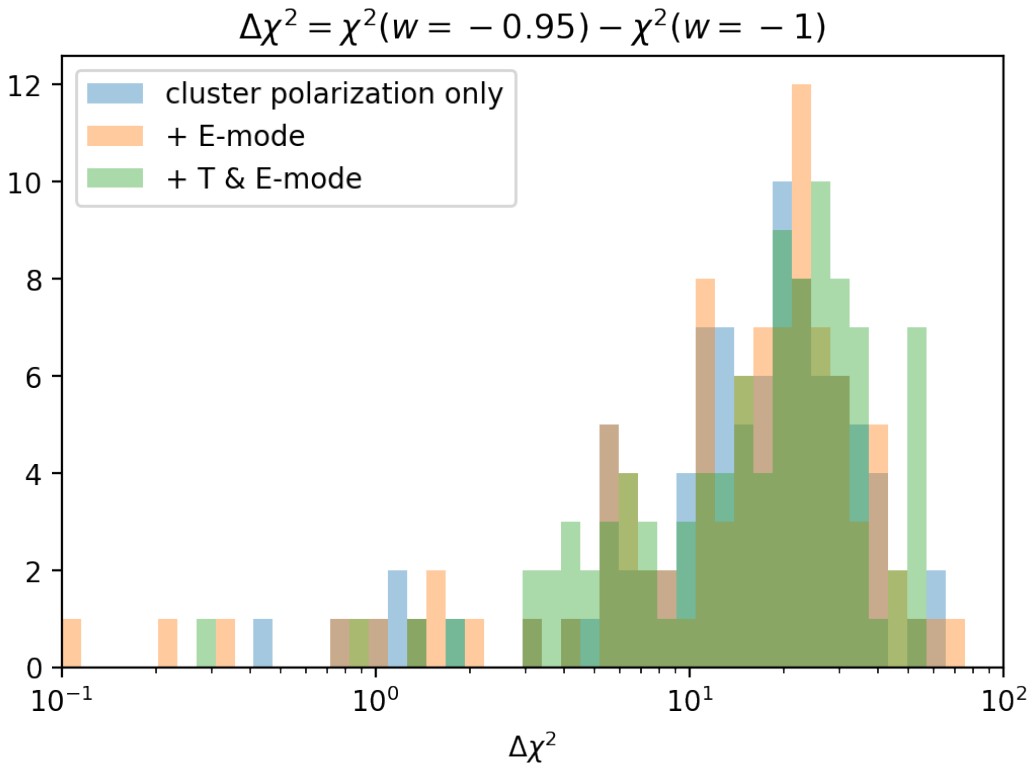

Figure 4.17: Distribution of the difference of the chi-square statistic for the 100 simulations at w = -0.95. Each color shows the case of fitting using only the polarization of the galaxy cluster, the case of fitting adding the E-mode of the all-sky CMB observations, and the case of also adding temperature anisotropy.

4.5 Reconstructed initial fluctuations

In this section, we consider the initial fluctuations reconstructed in the simulation process.
In the first step of the simulation, the initial fluctuations are given using Gaussians to fit the power spectrum. Since the spectrum is almost flat, it shows a wavenumber-independent feature as shown in Fig.4.18. Ideally, the reconstruction of the initial fluctuations would result in fluctuations with similar flat features. However, the reconstructed fluctuations in the current simulation are shown in Fig.4.19. As the amount of observations used in the reconstruction increases, the range of wave numbers reconstructed also increases. In addition, using the wrong parameters in the reconstruction results in excessively large amplitudes on some scales, while the amplitudes around them are suppressed, and stripe patterns float. When the reconstructed fluctuation amplitudes are converted to the same dimension as the transfer function, the distribution is very similar to that of the transfer function, as shown in Fig. 4.20. The reconstructed initial fluctuations are limited to the range of these transition functions, and their distribution is similar to the behavior of the transition functions. The scale of the initial fluctuations that can be reconstructed is naturally limited to the scale at which the observables are sensitive. Therefore, it is suitable to test the statistical power with the quadrupole at $z = 0$ in this method using the polarization of the galaxy clusters that reflect the remote quadrupole.

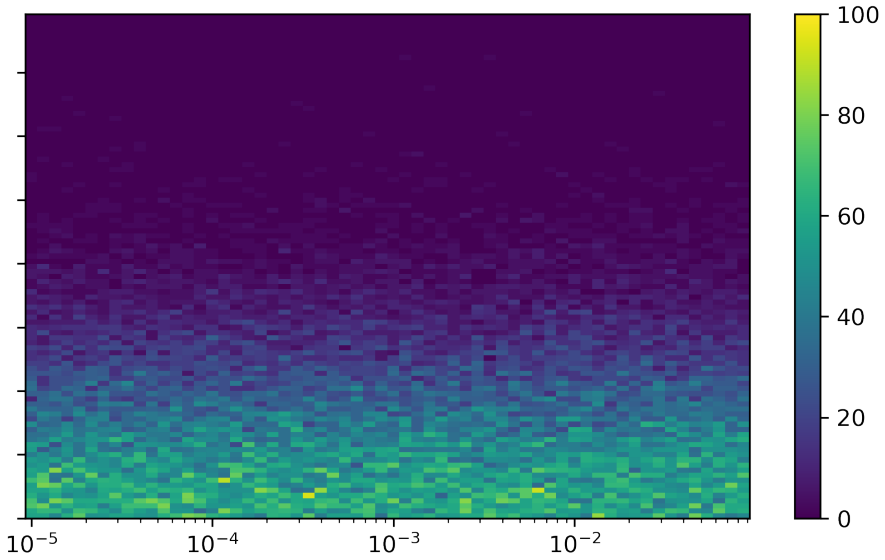

Figure 4.18: Initial fluctuations generated in the first stage of the simulation. The initial fluctuations in one simulation are given by 46080 independent values from 768 sky directions and 60 scales. The horizontal axis is the wavenumber and the vertical axis is the intensity, and the color of each pixel represents the number of initial fluctuations applicable Since the initial fluctuations in this study are scale-independent, the features do not change along the horizontal axis.

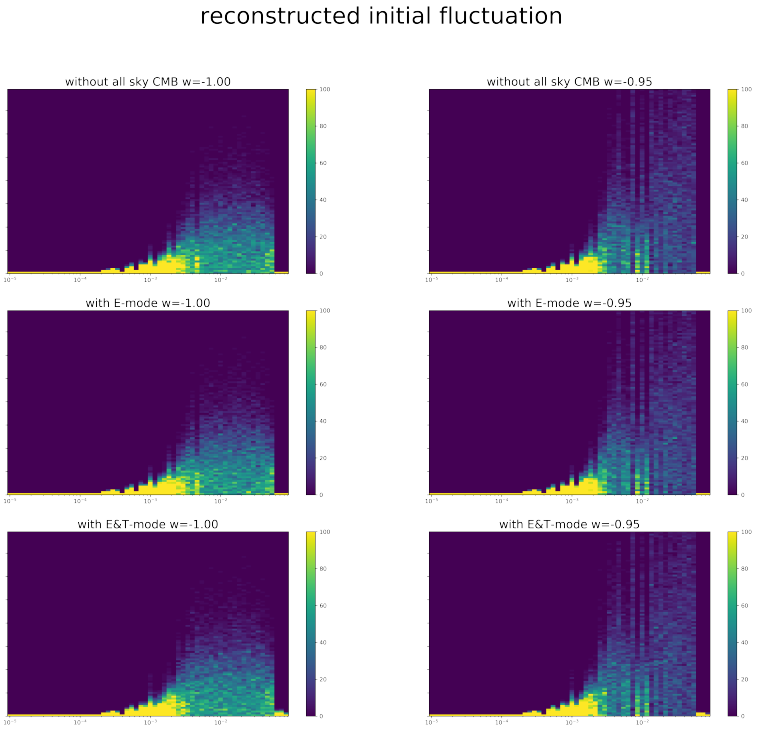

Figure 4.19: Reconstructed initial fluctuations in a simulation. The initial fluctuations in a simulation are given by 46080 independent values from 768 sky directions and 60 scales. The horizontal axis is the wavenumber and the vertical axis is the intensity. The color of each pixel represents the number of initial fluctuations corresponding to that region. The figures on the left show the initial fluctuations recovered using the correct dark energy equation of state parameters, and the figures on the right show the initial fluctuations recovered using the wrong dark energy equation of state parameters of w = -0.95. The upper figures also use only the polarization of the galaxy cluster in the fitting for the restoration. The middle panels additionally use the E-mode of the all-sky CMB observations, and the lower panels also use the temperature anisotropy T-mode.

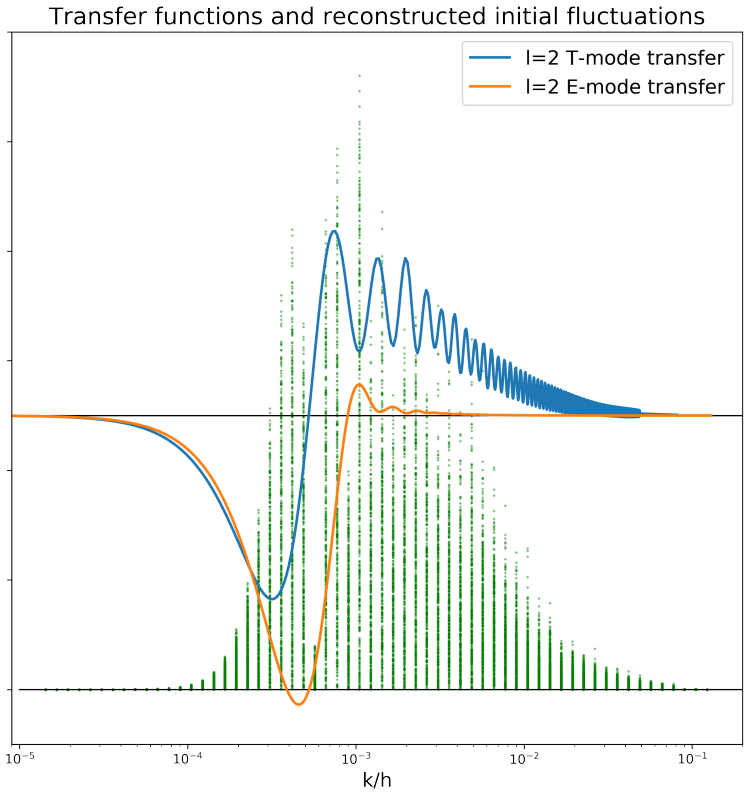

Figure 4.20: Quadrupole transfer function and reconstructed initial fluctuations. The horizontal axis shows the wavenumber of the initial fluctuations, and the reconstructed initial fluctuations for each scale are plotted in a scatter plot. Overlaid blue and orange solid lines plot the quadrupole transition functions, which are temperature anisotropy and E-mode polarization, respectively.

Chapter 5

Discussion

In this study, the improvement in statistical power with the addition of E-mode deflection fluctuations was more limited than previously assumed. E-mode polarization fluctuations, which have the same scattering process as the galaxy cluster polarization and occur at higher redshifts, are expected to correlate well with the galaxy cluster polarization. However, if sufficient information on the SW effect was available in the distant galaxy clusters, the E-mode polarization would not have information on the ISW effect due to its higher redshift, and its effect would have been limited. On the other hand, the higher-order multipoles of the temperature fluctuations provide information on the ISW effect at small scales, which could have provided a good contrast to distant clusters of galaxies with only the SW effect.

In this thesis, a priors that minimizes when the amplitude of the fluctuation is zero is incorporated in the fitting function of the process of reconstructing the initial fluctuations. However, such a priors interfere with the reproduction of the power spectrum, so it is necessary to find an alternative priors. Complex priors, however, significantly increase the computational cost and make the method difficult to compute, so they must be simple and allow for positive and negative reversal of the initial fluctuations during the fitting.
Transfer functions used in simulations must be precise to small scales. When the transfer function is obtained analytically, it may not converge sufficiently on the small-scale side due to the limitation of computational cost. If such a function is used, the reconstruction process of the initial fluctuation will cause large fluctuations on the small scale, which will affect the validation of the method.
The distribution of the electric gas inside the galaxy cluster is another factor that needs to be verified. The intrinsic density changes the optical depth [22], and deviations from the spherical shape produce polarization independent of quadrupole temperature fluctuations.
The peculiar velocity of a galaxy cluster also generates quadrupole temperature fluctuations [4][52]. Therefore, it is necessary to treat the velocity of galaxy clusters if more detailed analysis is to be realized.

[22]

Chapter 6

Summary and future prospects

In this thesis, in order to constrain the nature of dark energy, we present a method to combine information on the CMB quadrupole temperature anisotropy at the redshift of a galaxy cluster obtained from the CMB polarization produced by the Thomson scattering in the cluster with the quadrupole anisotropy of the CMB temperature and E-mode polarization directly observed at $z = 0$. Conventional analysis methods using the ISW effect have large variances due to initial density fluctuations at recombination (SW effect), which disturb the statistical detection of the ISW effect [14]. However, in this method, the initial fluctuations are reconstructed to fit the CMB observables including the galaxy cluster polarization, thus suppressing the effect of variance from the initial fluctuations and allowing us to verify the nature of the dark energy by the ISW effect. In the previous study [33], only the quadrupole of temperature anisotropy at redshift z = 0, which is clearly expected to have a correlation with the polarization of CMB photons scattered by galaxy clusters, is used to constrain the equation of state parameters of dark energy. However, the quadrupole components of the CMB scattered by galaxy clusters are quadrupoles at different locations in the same universe. Therefore, it correlates not only with quadrupoles but also with higher multipoles at $z = 0$, which is shown in [41]. Compared to the constraints for galaxy cluster polarization alone, the constraint on the dark energy parameter w when including E-mode polarization ($l \geq 2$) and temperature anisotropy ($l \geq 3$), with 6000 clusters and assuming a polarization sensitivity $\sigma_{\rm pol}/\tau = 10^{-2}$ μK, for $w = -1$ and $w = -0.95$ dark energy models, is improved by 18% as shown. The improvement is due to the fact that the information on E-mode polarization and temperature anisotropy at $z = 0$ allowed us to solve a part of the degeneracy between the 3D density fluctuation Fourier modes inferred from the polarization produced in galaxy clusters.

6.1 future prospects

The polarization of a galaxy cluster produced by Thomson scattering is typically about $10^{-2}\mu$K. Since the expected angle is about 2 arcmin ($z \sim 1$), the sensitivity required for detection is about 2×10^{-2} μK·arcmin. The sensitivity of the Simons Observatory, the most advanced ground-based CMB polarization observation currently ongoing, is about 3μK, which is not enough to detect the polarization of each galaxy cluster [23]. In addition, CMB S4, which is planned for the future, will increase the number of 6-meter large aperture telescopes to three and improve the sensitivity to about 1μK. Even at this stage, it is difficult to observe the polarization of individual clusters of galaxies, but As shown in Fig.6.1. Using the full cluster object, the cluster polarization signal can be

detected.

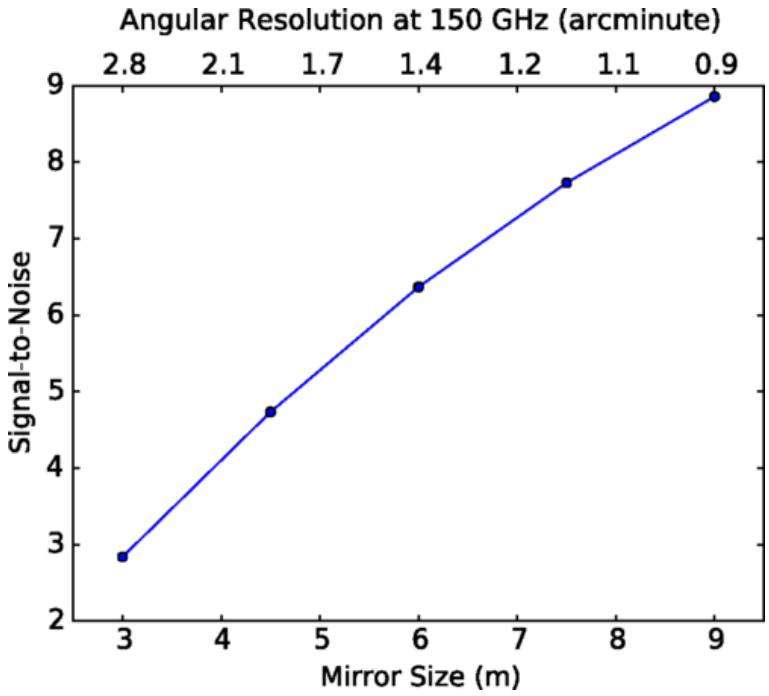

Figure 6.1: Aggregate S/N on the measurement of the cluster polarized emission for a future CMB S4 experiment. The S/N scales roughly linearly with mirror size.(figure taken from ref [41]).

Not only sensitivity but also contamination by foreground radiation is an important issue. The main sources are synchrotron radiation and thermal dust emission, and the removal of foreground radiation using their frequency dependencies is also necessary to improve detection [60][61].

The simulations in this thesis used galaxy clusters up to redshift 2. There are various methods to identify galaxy clusters, including galaxy density, weak-weight lensing effects, SZ effects, and x-ray emission in the Intracluster medium. Each method has different redshifts and masses of galaxy clusters that can be detected, and the predictions for the current observations are shown in Fig.6.2. The depest observations are the SZ effect in CMB observations [8] [29], and CMB S4 can detect galaxy clusters at $z \sim 2$ [51].
Although the simulations in this thesis were performed only for the dark energy equation of state parameter, the method allows the user to arbitrarily choose the cosmological parameters to be assumed and verified.
If the present method can be used to precisely reconstruct the initial fluctuations inside the optical cone, it will allow direct comparison with the large-scale structure of the low redshift. This shows the possibility of examining the evolution of the universe without using statistics, which is not possible with other methods.
If it can also be shown that the dark energy equation of state parameter w is not -1, this could be a turning point in physics, as dark energy becomes a completely unknown energy, not vacuum energy.

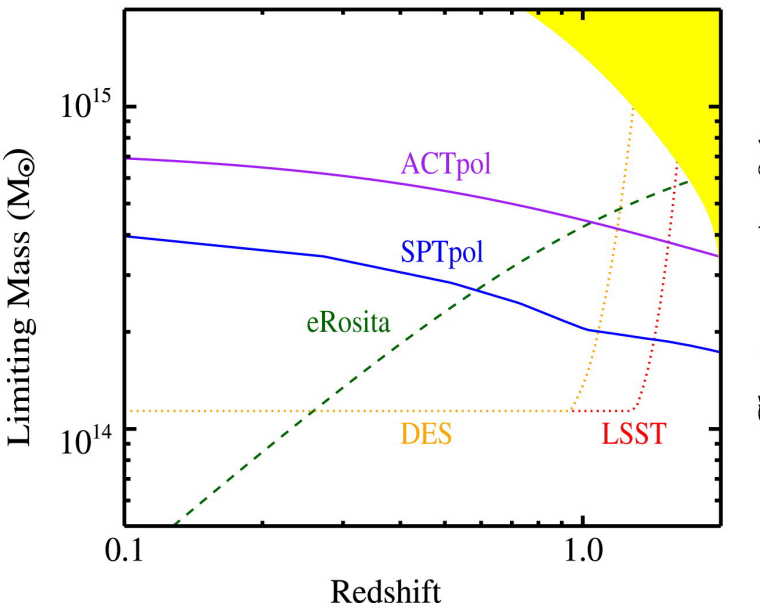

Figure 6.2: Predictions of detectable masses and redshifts of galaxy clusters in the major observations. (figure taken from ref [62]).

References

[1] T. Abbott, F. B. Abdalla, S. Allam, A. Amara, J. Annis, R. Armstrong, D. Bacon, M. Banerji, A. H. Bauer, E. Baxter, M. R. Becker, A. Benoit-Lévy, R. A. Bernstein, G. M. Bernstein, E. Bertin, J. Blazek, C. Bonnett, S. L. Bridle, D. Brooks, C. Bruderer, E. Buckley-Geer, D. L. Burke, M. T. Busha, D. Capozzi, A. Carnero Rosell, M. Carrasco Kind, J. Carretero, F. J. Castander, C. Chang, J. Clampitt, M. Crocce, C. E. Cunha, C. B. D'Andrea, L. N. da Costa, R. Das, D. L. DePoy, S. Desai, H. T. Diehl, J. P. Dietrich, S. Dodelson, P. Doel, A. Drlica-Wagner, G. Efstathiou, T. F. Eifler, B. Erickson, J. Estrada, A. E. Evrard, A. Fausti Neto, E. Fernandez, D. A. Finley, B. Flaugher, P. Fosalba, O. Friedrich, J. Frieman, C. Gangkofner, J. Garcia-Bellido, E. Gaztanaga, D. W. Gerdes, D. Gruen, R. A. Gruendl, G. Gutierrez, W. Hartley, M. Hirsch, K. Honscheid, E. M. Huff, B. Jain, D. J. James, M. Jarvis, T. Kacprzak, S. Kent, D. Kirk, E. Krause, A. Kravtsov, K. Kuehn, N. Kuropatkin, J. Kwan, O. Lahav, B. Leistedt, T. S. Li, M. Lima, H. Lin, N. MacCrann, M. March, J. L. Marshall, P. Martini, R. G. McMahon, P. Melchior, C. J. Miller, R. Miquel, J. J. Mohr, E. Neilsen, R. C. Nichol, A. Nicola, B. Nord, R. Ogando, A. Palmese, H. V. Peiris, A. A. Plazas, A. Refregier, N. Roe, A. K. Romer, A. Roodman, B. Rowe, E. S. Rykoff, C. Sabiu, I. Sadeh, M. Sako, S. Samuroff, E. Sanchez, C. Sánchez, H. Seo, I. Sevilla-Noarbe, E. Sheldon, R. C. Smith, M. Soares-Santos, F. Sobreira, E. Suchyta, M. E. C. Swanson, G. Tarle, J. Thaler, D. Thomas, M. A. Troxel, V. Vikram, A. R. Walker, R. H. Wechsler, J. Weller, Y. Zhang, J. Zuntz, and Dark Energy Survey Collaboration. Cosmology from cosmic shear with Dark Energy Survey Science Verification data. *Phys. Rev. D*, 94(2):022001, July 2016.

[2] T. M. C. Abbott, S. Allam, P. Andersen, C. Angus, J. Asorey, A. Avelino, S. Avila, B. A. Bassett, K. Bechtol, G. M. Bernstein, E. Bertin, D. Brooks, D. Brout, P. Brown, D. L. Burke, J. Calcino, A. Carnero Rosell, D. Carollo, M. Carrasco Kind, J. Carretero, R. Casas, F. J. Castander, R. Cawthon, P. Challis, M. Childress, A. Clocchiatti, C. E. Cunha, C. B. D'Andrea, L. N. da Costa, C. Davis, T. M. Davis, J. De Vicente, D. L. DePoy, S. Desai, H. T. Diehl, P. Doel, A. Drlica-Wagner, T. F. Eifler, A. E. Evrard, E. Fernandez, A. V. Filippenko, D. A. Finley, B. Flaugher, R. J. Foley, P. Fosalba, J. Frieman, L. Galbany, J. García-Bellido, E. Gaztanaga, T. Giannantonio, K. Glazebrook, D. A. Goldstein, S. González-Gaitán, D. Gruen, R. A. Gruendl, J. Gschwend, R. R. Gupta, G. Gutierrez, W. G. Hartley, S. R. Hinton, D. L. Hollowood, K. Honscheid, J. K. Hoormann, B. Hoyle, D. J. James, T. Jeltema, M. W. G. Johnson, M. D. Johnson, E. Kasai, S. Kent, R. Kessler, A. G. Kim, R. P. Kirshner, E. Kovacs, E. Krause, R. Kron, K. Kuehn, S. Kuhlmann, N. Kuropatkin, O. Lahav, J. Lasker, G. F. Lewis, T. S. Li, C. Lidman, M. Lima, H. Lin, E. Macaulay, M. A. G. Maia, K. S. Mandel, M. March, J. Marriner, J. L. Marshall, P. Martini, F. Menanteau, C. J.

Miller, R. Miquel, V. Miranda, J. J. Mohr, E. Morganson, D. Muthukrishna, A. Möller, E. Neilsen, R. C. Nichol, B. Nord, P. Nugent, R. L. C. Ogando, A. Palmese, Y. C. Pan, A. A. Plazas, M. Pursiainen, A. K. Romer, A. Roodman, E. Rozo, E. S. Rykoff, M. Sako, E. Sanchez, V. Scarpine, R. Schindler, M. Schubnell, D. Scolnic, S. Serrano, I. Sevilla-Noarbe, R. Sharp, M. Smith, M. Soares-Santos, F. Sobreira, N. E. Sommer, H. Spinka, E. Suchyta, M. Sullivan, E. Swann, G. Tarle, D. Thomas, R. C. Thomas, M. A. Troxel, B. E. Tucker, S. A. Uddin, A. R. Walker, W. Wester, P. Wiseman, R. C. Wolf, B. Yanny, B. Zhang, Y. Zhang, and DES Collaboration. First Cosmology Results using Type Ia Supernovae from the Dark Energy Survey: Constraints on Cosmological Parameters. *ApJ*, 872(2):L30, February 2019.

[3] L. Raul Abramo and Henrique S. Xavier. Real space tomography of the primordial Universe with cluster polarization. *Phys. Rev. D*, 75(10):101302, May 2007.

[4] Edouard Audit and John F. L. Simmons. The kinematic Sunyaev-Zel'dovich effect and transverse cluster velocities. *MNRAS*, 305(1):L27–L30, May 1999.

[5] Benjamin Audren, Julien Lesgourgues, Gianpiero Mangano, Pasquale Dario Serpico, and Thomas Tram. Strongest model-independent bound on the lifetime of Dark Matter. *JCAP*, 2014(12):028–028, December 2014.

[6] Julian E. Bautista, Romain Paviot, Mariana Vargas Magaña, Sylvain de la Torre, Sebastien Fromenteau, Hector Gil-Marín, Ashley J. Ross, Etienne Burtin, Kyle S. Dawson, Jiamin Hou, Jean-Paul Kneib, Arnaud de Mattia, Will J. Percival, Graziano Rossi, Rita Tojeiro, Cheng Zhao, Gong-Bo Zhao, Shadab Alam, Joel Brownstein, Michael J. Chapman, Peter D. Choi, Chia-Hsun Chuang, Stéphanie Escoffier, Axel de la Macorra, Hélion du Mas des Bourboux, Faizan G. Mohammad, Jeongin Moon, Eva-Maria Müller, Seshadri Nadathur, Jeffrey A. Newman, Donald Schneider, Hee-Jong Seo, and Yuting Wang. The completed SDSS-IV extended Baryon Oscillation Spectroscopic Survey: measurement of the BAO and growth rate of structure of the luminous red galaxy sample from the anisotropic correlation function between redshifts 0.6 and 1. *MNRAS*, 500(1):736–762, January 2021.

[7] C. L. Bennett, M. Halpern, G. Hinshaw, N. Jarosik, A. Kogut, M. Limon, S. S. Meyer, L. Page, D. N. Spergel, G. S. Tucker, E. Wollack, E. L. Wright, C. Barnes, M. R. Greason, R. S. Hill, E. Komatsu, M. R. Nolta, N. Odegard, H. V. Peiris, L. Verde, and J. L. Weiland. First-Year Wilkinson Microwave Anisotropy Probe (WMAP) Observations: Preliminary Maps and Basic Results. *ApJS*, 148(1):1–27, September 2003.

[8] L. E. Bleem, S. Bocquet, B. Stalder, M. D. Gladders, P. A. R. Ade, S. W. Allen, A. J. Anderson, J. Annis, M. L. N. Ashby, J. E. Austermann, S. Avila, J. S. Avva, M. Bayliss, J. A. Beall, K. Bechtol, A. N. Bender, B. A. Benson, E. Bertin, F. Bianchini, C. Blake, M. Brodwin, D. Brooks, E. Buckley-Geer, D. L. Burke, J. E. Carlstrom, A. Carnero Rosell, M. Carrasco Kind, J. Carretero, C. L. Chang, H. C. Chiang, R. Citron, C. Corbett Moran, M. Costanzi, T. M. Crawford, A. T. Crites, L. N. da Costa, T. de Haan, J. De Vicente, S. Desai, H. T. Diehl, J. P. Dietrich, M. A. Dobbs, T. F. Eifler, W. Everett, B. Flaugher, B. Floyd, J. Frieman, J. Gallicchio, J. García-Bellido, E. M. George, D. W. Gerdes, A. Gilbert, D. Gruen, R. A. Gruendl, J. Gschwend, N. Gupta, G. Gutierrez, N. W. Halverson, N. Harring-

ton, J. W. Henning, C. Heymans, G. P. Holder, D. L. Hollowood, W. L. Holzapfel, K. Honscheid, J. D. Hrubes, N. Huang, J. Hubmayr, K. D. Irwin, D. J. James, T. Jeltema, S. Joudaki, G. Khullar, M. Klein, L. Knox, N. Kuropatkin, A. T. Lee, D. Li, C. Lidman, A. Lowitz, N. MacCrann, G. Mahler, M. A. G. Maia, J. L. Marshall, M. McDonald, J. J. McMahon, P. Melchior, F. Menanteau, S. S. Meyer, R. Miquel, L. M. Mocanu, J. J. Mohr, J. Montgomery, A. Nadolski, T. Natoli, J. P. Nibarger, G. Noble, V. Novosad, S. Padin, A. Palmese, D. Parkinson, S. Patil, F. Paz-Chinchón, A. A. Plazas, C. Pryke, N. S. Ramachandra, C. L. Reichardt, J. D. Remolina González, A. K. Romer, A. Roodman, J. E. Ruhl, E. S. Rykoff, B. R. Saliwanchik, E. Sanchez, A. Saro, J. T. Sayre, K. K. Schaffer, T. Schrabback, S. Serrano, K. Sharon, C. Sievers, G. Smecher, M. Smith, M. Soares-Santos, A. A. Stark, K. T. Story, E. Suchyta, G. Tarle, C. Tucker, K. Vanderlinde, T. Veach, J. D. Vieira, G. Wang, J. Weller, N. Whitehorn, W. L. K. Wu, V. Yefremenko, and Y. Zhang. The SPTpol Extended Cluster Survey. *ApJS*, 247(1):25, March 2020.

[9] S. P. Boughn and R. G. Crittenden. Cross Correlation of the Cosmic Microwave Background with Radio Sources: Constraints on an Accelerating Universe. *Phys. Rev. Lett.*, 88(2):021302, December 2001.

[10] Stephen Boughn and Robert Crittenden. A correlation between the cosmic microwave background and large-scale structure in the Universe. *Nature*, 427(6969):45–47, January 2004.

[11] Emory F. Bunn. Probing the Universe on gigaparsec scales with remote cosmic microwave background quadrupole measurements. *Phys. Rev. D*, 73(12):123517, June 2006.

[12] Paul Carter, Florian Beutler, Will J. Percival, Chris Blake, Jun Koda, and Ashley J. Ross. Low redshift baryon acoustic oscillation measurement from the reconstructed 6-degree field galaxy survey. *MNRAS*, 481(2):2371–2383, December 2018.

[13] Asantha Cooray and Daniel Baumann. CMB polarization towards clusters as a probe of the integrated Sachs-Wolfe effect. *Phys. Rev. D*, 67(6):063505, March 2003.

[14] Asantha Cooray, Dragan Huterer, and Daniel Baumann. Growth rate of large-scale structure as a powerful probe of dark energy. *Phys. Rev. D*, 69(2):027301, January 2004.

[15] Robert G. Crittenden and Neil Turok. Looking for a Cosmological Constant with the Rees-Sciama Effect. *Phys. Rev. Lett.*, 76(4):575–578, January 1996.

[16] Anne-Sylvie Deutsch, Matthew C. Johnson, Moritz Münchmeyer, and Alexandra Terrana. Polarized Sunyaev Zel'dovich tomography. *JCAP*, 2018(4):034, April 2018.

[17] Scott Dodelson. Determining Cosmic Microwave Background Anisotropies in the Presence of Foregrounds. *ApJ*, 482(2):577–587, June 1997.

[18] F. X. Dupé, A. Rassat, J. L. Starck, and M. J. Fadili. Measuring the integrated Sachs-Wolfe effect. *A.&Ap.*, 534:A51, October 2011.

[19] Albert Einstein. Kosmologische Betrachtungen zur allgemeinen Relativitätstheorie. *Sitzungsberichte der Königlich Preussischen Akademie der Wissenschaften*, pages 142–152, January 1917.

[20] Daniel J. Eisenstein, Idit Zehavi, David W. Hogg, Roman Scoccimarro, Michael R. Blanton, Robert C. Nichol, Ryan Scranton, Hee-Jong Seo, Max Tegmark, Zheng Zheng, Scott F. Anderson, Jim Annis, Neta Bahcall, Jon Brinkmann, Scott Burles, Francisco J. Castander, Andrew Connolly, Istvan Csabai, Mamoru Doi, Masataka Fukugita, Joshua A. Frieman, Karl Glazebrook, James E. Gunn, John S. Hendry, Gregory Hennessy, Zeljko Ivezić, Stephen Kent, Gillian R. Knapp, Huan Lin, Yeong-Shang Loh, Robert H. Lupton, Bruce Margon, Timothy A. McKay, Avery Meiksin, Jeffery A. Munn, Adrian Pope, Michael W. Richmond, David Schlegel, Donald P. Schneider, Kazuhiro Shimasaku, Christopher Stoughton, Michael A. Strauss, Mark SubbaRao, Alexander S. Szalay, István Szapudi, Douglas L. Tucker, Brian Yanny, and Donald G. York. Detection of the Baryon Acoustic Peak in the Large-Scale Correlation Function of SDSS Luminous Red Galaxies. *ApJ*, 633(2):560–574, November 2005.

[21] D. J. Fixsen, E. S. Cheng, D. A. Cottingham, Jr. Eplee, R. E., R. B. Isaacman, J. C. Mather, S. S. Meyer, P. D. Noerdlinger, R. A. Shafer, R. Weiss, E. L. Wright, C. L. Bennett, N. W. Boggess, T. Kelsall, S. H. Moseley, R. F. Silverberg, G. F. Smoot, and D. T. Wilkinson. Cosmic Microwave Background Dipole Spectrum Measured by the COBE FIRAS Instrument. *ApJ*, 420:445, January 1994.

[22] Samuel Flender, Daisuke Nagai, and Michael McDonald. Constraints on the Optical Depth of Galaxy Groups and Clusters. *ApJ*, 837(2):124, March 2017.

[23] Patricio A. Gallardo, Jon Gudmundsson, Brian J. Koopman, Frederick T. Matsuda, Sara M. Simon, Aamir Ali, Sean Bryan, Yuji Chinone, Gabriele Coppi, Nicholas Cothard, Mark J. Devlin, Simon Dicker, Giulio Fabbian, Nicholas Galitzki, Charles A. Hill, Brian Keating, Akito Kusaka, Jacob Lashner, Adrian T. Lee, Michele Limon, Philip D. Mauskopf, Jeff McMahon, Federico Nati, Michael D. Niemack, John L. Orlowski-Scherer, Stephen C. Parshley, Giuseppe Puglisi, Christian L. Reichardt, Maria Salatino, Suzanne Staggs, Aritoki Suzuki, Eve M. Vavagiakis, Edward J. Wollack, Zhilei Xu, and Ningfeng Zhu. Systematic uncertainties in the Simons Observatory: optical effects and sensitivity considerations. In Jonas Zmuidzinas and Jian-Rong Gao, editors, *Millimeter, Submillimeter, and Far-Infrared Detectors and Instrumentation for Astronomy IX*, volume 10708 of *Society of Photo-Optical Instrumentation Engineers (SPIE) Conference Series*, page 107083Y, July 2018.

[24] Héctor Gil-Marín, Julián E. Bautista, Romain Paviot, Mariana Vargas-Magaña, Sylvain de la Torre, Sebastien Fromenteau, Shadab Alam, Santiago Ávila, Etienne Burtin, Chia-Hsun Chuang, Kyle S. Dawson, Jiamin Hou, Arnaud de Mattia, Faizan G. Mohammad, Eva-Maria Müller, Seshadri Nadathur, Richard Neveux, Will J. Percival, Anand Raichoor, Mehdi Rezaie, Ashley J. Ross, Graziano Rossi, Vanina Ruhlmann-Kleider, Alex Smith, Amélie Tamone, Jeremy L. Tinker, Rita Tojeiro, Yuting Wang, Gong-Bo Zhao, Cheng Zhao, Jonathan Brinkmann, Joel R. Brownstein, Peter D. Choi, Stephanie Escoffier, Axel de la Macorra, Jeongin Moon, Jeffrey A. Newman, Donald P. Schneider, Hee-Jong Seo, and Mariappan Vivek. The Completed

SDSS-IV extended Baryon Oscillation Spectroscopic Survey: measurement of the BAO and growth rate of structure of the luminous red galaxy sample from the anisotropic power spectrum between redshifts 0.6 and 1.0. *MNRAS*, 498(2):2492–2531, October 2020.

[25] E. Goto. The parametron, a digital computing element which utilizes parametric oscillation. *Proceedings of the IRE*, 47(8):1304–1316, 1959.

[26] Alex Hall and Anthony Challinor. Detecting the polarization induced by scattering of the microwave background quadrupole in galaxy clusters. *Phys. Rev. D*, 90(6):063518, September 2014.

[27] Takashi Hamana, Masato Shirasaki, Satoshi Miyazaki, Chiaki Hikage, Masamune Oguri, Surhud More, Robert Armstrong, Alexie Leauthaud, Rachel Mandelbaum, Hironao Miyatake, Atsushi J. Nishizawa, Melanie Simet, Masahiro Takada, Hiroaki Aihara, James Bosch, Yutaka Komiyama, Robert Lupton, Hitoshi Murayama, Michael A. Strauss, and Masayuki Tanaka. Cosmological constraints from cosmic shear two-point correlation functions with HSC survey first-year data. *PASJ*, 72(1):16, February 2020.

[28] M. Hazumi, P. A. R. Ade, A. Adler, E. Allys, K. Arnold, D. Auguste, J. Aumont, R. Aurlien, J. Austermann, C. Baccigalupi, A. J. Banday, R. Banjeri, R. B. Barreiro, S. Basak, J. Beall, D. Beck, S. Beckman, J. Bermejo, P. de Bernardis, M. Bersanelli, J. Bonis, J. Borrill, F. Boulanger, S. Bounissou, M. Brilenkov, M. Brown, M. Bucher, E. Calabrese, P. Campeti, A. Carones, F. J. Casas, A. Challinor, V. Chan, K. Cheung, Y. Chinone, J. F. Cliche, L. Colombo, F. Columbro, J. Cubas, A. Cukierman, D. Curtis, G. D'Alessandro, N. Dachlythra, M. De Petris, C. Dickinson, P. Diego-Palazuelos, M. Dobbs, T. Dotani, L. Duband, S. Duff, J. M. Duval, K. Ebisawa, T. Elleflot, H. K. Eriksen, J. Errard, T. Essinger-Hileman, F. Finelli, R. Flauger, C. Franceschet, U. Fuskeland, M. Galloway, K. Ganga, J. R. Gao, R. Genova-Santos, M. Gerbino, M. Gervasi, T. Ghigna, E. Gjerløw, M. L. Gradziel, J. Grain, F. Grupp, A. Gruppuso, J. E. Gudmundsson, T. de Haan, N. W. Halverson, P. Hargrave, T. Hasebe, M. Hasegawa, M. Hattori, S. Henrot-Versillé, D. Herman, D. Herranz, C. A. Hill, G. Hilton, Y. Hirota, E. Hivon, R. A. Hlozek, Y. Hoshino, E. de la Hoz, J. Hubmayr, K. Ichiki, T. Iida, H. Imada, K. Ishimura, H. Ishino, G. Jaehnig, T. Kaga, S. Kashima, N. Katayama, A. Kato, T. Kawasaki, R. Keskitalo, T. Kisner, Y. Kobayashi, N. Kogiso, A. Kogut, K. Kohri, E. Komatsu, K. Komatsu, K. Konishi, N. Krachmalnicoff, I. Kreykenbohm, C. L. Kuo, A. Kushino, L. Lamagna, J. V. Lanen, M. Lattanzi, A. T. Lee, C. Leloup, F. Levrier, E. Linder, T. Louis, G. Luzzi, T. Maciaszek, B. Maffei, D. Maino, M. Maki, S. Mandelli, E. Martinez-Gonzalez, S. Masi, T. Matsumura, A. Mennella, M. Migliaccio, Y. Minami, K. Mitsuda, J. Montgomery, L. Montier, G. Morgante, B. Mot, Y. Murata, J. A. Murphy, M. Nagai, Y. Nagano, T. Nagasaki, R. Nagata, S. Nakamura, T. Namikawa, P. Natoli, S. Nerval, T. Nishibori, H. Nishino, F. Noviello, C. O'Sullivan, H. Ogawa, H. Ogawa, S. Oguri, H. Ohsaki, I. S. Ohta, N. Okada, N. Okada, L. Pagano, A. Paiella, D. Paoletti, G. Patanchon, J. Peloton, F. Piacentini, G. Pisano, G. Polenta, D. Poletti, T. Prouvé, G. Puglisi, D. Rambaud, C. Raum, S. Realini, M. Reinecke, M. Remazeilles, A. Ritacco, G. Roudil, J. A. Rubino-Martin, M. Russell, H. Sakurai, Y. Sakurai, M. Sandri, M. Sasaki, G. Savini, D. Scott, J. Seibert, Y. Sekimoto, B. Sherwin, K. Shinozaki, M. Shiraishi, P. Shirron, G. Sig-

norelli, G. Smecher, S. Stever, R. Stompor, H. Sugai, S. Sugiyama, A. Suzuki, J. Suzuki, T. L. Svalheim, E. Switzer, R. Takaku, H. Takakura, S. Takakura, Y. Takase, Y. Takeda, A. Tartari, E. Taylor, Y. Terao, H. Thommesen, K. L. Thompson, B. Thorne, T. Toda, M. Tomasi, M. Tominaga, N. Trappe, M. Tristram, M. Tsuji, M. Tsujimoto, C. Tucker, J. Ullom, G. Vermeulen, P. Vielva, F. Villa, M. Vissers, N. Vittorio, I. Wehus, J. Weller, B. Westbrook, J. Wilms, B. Winter, E. J. Wollack, N. Y. Yamasaki, T. Yoshida, J. Yumoto, M. Zannoni, and A. Zonca. LiteBIRD satellite: JAXA's new strategic L-class mission for all-sky surveys of cosmic microwave background polarization. In *Society of Photo-Optical Instrumentation Engineers (SPIE) Conference Series*, volume 11443 of *Society of Photo-Optical Instrumentation Engineers (SPIE) Conference Series*, page 114432F, December 2020.

[29] Matt Hilton, Matthew Hasselfield, Cristóbal Sifón, Nicholas Battaglia, Simone Aiola, V. Bharadwaj, J. Richard Bond, Steve K. Choi, Devin Crichton, Rahul Datta, Mark J. Devlin, Joanna Dunkley, Rolando Dünner, Patricio A. Gallardo, Megan Gralla, Adam D. Hincks, Shuay-Pwu P. Ho, Johannes Hubmayr, Kevin M. Huffenberger, John P. Hughes, Brian J. Koopman, Arthur Kosowsky, Thibaut Louis, Mathew S. Madhavacheril, Tobias A. Marriage, Loïc Maurin, Jeff McMahon, Hironao Miyatake, Kavilan Moodley, Sigurd Næss, Federico Nati, Laura Newburgh, Michael D. Niemack, Masamune Oguri, Lyman A. Page, Bruce Partridge, Benjamin L. Schmitt, Jon Sievers, David N. Spergel, Suzanne T. Staggs, Hy Trac, Alexander van Engelen, Eve M. Vavagiakis, and Edward J. Wollack. The Atacama Cosmology Telescope: The Two-season ACTPol Sunyaev-Zel'dovich Effect Selected Cluster Catalog. *ApJS*, 235(1):20, March 2018.

[30] G. Hinshaw, D. Larson, E. Komatsu, D. N. Spergel, C. L. Bennett, J. Dunkley, M. R. Nolta, M. Halpern, R. S. Hill, N. Odegard, L. Page, K. M. Smith, J. L. Weiland, B. Gold, N. Jarosik, A. Kogut, M. Limon, S. S. Meyer, G. S. Tucker, E. Wollack, and E. L. Wright. Nine-year Wilkinson Microwave Anisotropy Probe (WMAP) Observations: Cosmological Parameter Results. *ApJS*, 208(2):19, October 2013.

[31] Edwin Hubble. A Relation between Distance and Radial Velocity among Extra-Galactic Nebulae. *Proceedings of the National Academy of Science*, 15(3):168–173, March 1929.

[32] Dragan Huterer and Michael S. Turner. Prospects for probing the dark energy via supernova distance measurements. *Phys. Rev. D*, 60:081301, Aug 1999.

[33] Kiyotomo Ichiki, Kento Sumiya, and Guo-Chin Liu. Measuring the cosmological density field twice: A novel test of dark energy using the CMB quadrupole. *Phys. Rev. D*, 105(6):063507, March 2022.

[34] Nick Kaiser. Clustering in real space and in redshift space. *MNRAS*, 227:1–21, July 1987.

[35] Marc Kamionkowski and Abraham Loeb. Getting around cosmic variance. *Phys. Rev. D*, 56(8):4511–4513, October 1997.

[36] Nanoom Lee, Selim C. Hotinli, and Marc Kamionkowski. Probing cosmic birefringence with polarized Sunyaev-Zel'dovich tomography. *Phys. Rev. D*, 106(8):083518, October 2022.

[37] G. Lemaître. Un Univers homogène de masse constante et de rayon croissant rendant compte de la vitesse radiale des nébuleuses extra-galactiques. *Annales de la Société Scientifique de Bruxelles*, 47:49–59, January 1927.

[38] Antony Lewis, Anthony Challinor, and Anthony Lasenby. Efficient computation of CMB anisotropies in closed FRW models. *ApJ*, 538:473–476, 2000.

[39] E. V. Linder and A. Jenkins. Cosmic structure growth and dark energy. *MNRAS*, 346(2):573–583, December 2003.

[40] Guo-Chin Liu, Kiyotomo Ichiki, Hiroyuki Tashiro, and Naoshi Sugiyama. Reconstruction of CMB temperature anisotropies with primordial CMB induced polarization in galaxy clusters. *MNRAS*, 460(1):L104–L108, Jul 2016.

[41] Thibaut Louis, Emory F. Bunn, Benjamin Wandelt, and Joseph Silk. Measuring polarized emission in clusters in the CMB S4 era. *Phys. Rev. D*, 96(12):123509, December 2017.

[42] J. C. Mather, E. S. Cheng, D. A. Cottingham, Jr. Eplee, R. E., D. J. Fixsen, T. Hewagama, R. B. Isaacman, K. A. Jensen, S. S. Meyer, P. D. Noerdlinger, S. M. Read, L. P. Rosen, R. A. Shafer, E. L. Wright, C. L. Bennett, N. W. Boggess, M. G. Hauser, T. Kelsall, Jr. Moseley, S. H., R. F. Silverberg, G. F. Smoot, R. Weiss, and D. T. Wilkinson. Measurement of the Cosmic Microwave Background Spectrum by the COBE FIRAS Instrument. *ApJ*, 420:439, January 1994.

[43] Arindam Mazumdar, Subhendra Mohanty, and Priyank Parashari. Evidence of dark energy in different cosmological observations. *European Physical Journal Special Topics*, 230(9):2055–2066, August 2021.

[44] Joel Meyers, P. Daniel Meerburg, Alexander van Engelen, and Nicholas Battaglia. Beyond CMB cosmic variance limits on reionization with the polarized Sunyaev-Zel'dovich effect. *Phys. Rev. D*, 97(10):103505, May 2018.

[45] Benjamin P. Moster, Rachel S. Somerville, Jeffrey A. Newman, and Hans-Walter Rix. A Cosmic Variance Cookbook. *ApJ*, 731(2):113, April 2011.

[46] P. J. E. Peebles and Bharat Ratra. The cosmological constant and dark energy. *Rev. Mod. Phys.*, 75:559–606, Apr 2003.

[47] S. Perlmutter, G. Aldering, G. Goldhaber, R. A. Knop, P. Nugent, P. G. Castro, S. Deustua, S. Fabbro, A. Goobar, D. E. Groom, I. M. Hook, A. G. Kim, M. Y. Kim, J. C. Lee, N. J. Nunes, R. Pain, C. R. Pennypacker, R. Quimby, C. Lidman, R. S. Ellis, M. Irwin, R. G. McMahon, P. Ruiz-Lapuente, N. Walton, B. Schaefer, B. J. Boyle, A. V. Filippenko, T. Matheson, A. S. Fruchter, N. Panagia, H. J. M. Newberg, W. J. Couch, and The Supernova Cosmology Project. Measurements of Ω and Λ from 42 High-Redshift Supernovae. *ApJ*, 517(2):565–586, June 1999.

[48] Planck Collaboration, N. Aghanim, Y. Akrami, F. Arroja, M. Ashdown, J. Aumont, C. Baccigalupi, M. Ballardini, A. J. Banday, R. B. Barreiro, N. Bartolo, S. Basak, R. Battye, K. Benabed, J. P. Bernard, M. Bersanelli, P. Bielewicz, J. J. Bock, J. R. Bond, J. Borrill, F. R. Bouchet, F. Boulanger,

M. Bucher, C. Burigana, R. C. Butler, E. Calabrese, J. F. Cardoso, J. Carron, B. Casaponsa, A. Challinor, H. C. Chiang, L. P. L. Colombo, C. Combet, D. Contreras, B. P. Crill, F. Cuttaia, P. de Bernardis, G. de Zotti, J. Delabrouille, J. M. Delouis, F. X. Désert, E. Di Valentino, C. Dickinson, J. M. Diego, S. Donzelli, O. Doré, M. Douspis, A. Ducout, X. Dupac, G. Efstathiou, F. Elsner, T. A. Enßlin, H. K. Eriksen, E. Falgarone, Y. Fantaye, J. Fergusson, R. Fernandez-Cobos, F. Finelli, F. Forastieri, M. Frailis, E. Franceschi, A. Frolov, S. Galeotta, S. Galli, K. Ganga, R. T. Génova-Santos, M. Gerbino, T. Ghosh, J. González-Nuevo, K. M. Górski, S. Gratton, A. Gruppuso, J. E. Gudmundsson, J. Hamann, W. Handley, F. K. Hansen, G. Helou, D. Herranz, S. R. Hildebrandt, E. Hivon, Z. Huang, A. H. Jaffe, W. C. Jones, A. Karakci, E. Keihänen, R. Keskitalo, K. Kiiveri, J. Kim, T. S. Kisner, L. Knox, N. Krachmalnicoff, M. Kunz, H. Kurki-Suonio, G. Lagache, J. M. Lamarre, M. Langer, A. Lasenby, M. Lattanzi, C. R. Lawrence, M. Le Jeune, J. P. Leahy, J. Lesgourgues, F. Levrier, A. Lewis, M. Liguori, P. B. Lilje, M. Lilley, V. Lindholm, M. López-Caniego, P. M. Lubin, Y. Z. Ma, J. F. Macías-Pérez, G. Maggio, D. Maino, N. Mandolesi, A. Mangilli, A. Marcos-Caballero, M. Maris, P. G. Martin, M. Martinelli, E. Martínez-González, S. Matarrese, N. Mauri, J. D. McEwen, P. D. Meerburg, P. R. Meinhold, A. Melchiorri, A. Mennella, M. Migliaccio, M. Millea, S. Mitra, M. A. Miville-Deschênes, D. Molinari, A. Moneti, L. Montier, G. Morgante, A. Moss, S. Mottet, M. Münchmeyer, P. Natoli, H. U. Nørgaard-Nielsen, C. A. Oxborrow, L. Pagano, D. Paoletti, B. Partridge, G. Patanchon, T. J. Pearson, M. Peel, H. V. Peiris, F. Perrotta, V. Pettorino, F. Piacentini, L. Polastri, G. Polenta, J. L. Puget, J. P. Rachen, M. Reinecke, M. Remazeilles, C. Renault, A. Renzi, G. Rocha, C. Rosset, G. Roudier, J. A. Rubiño-Martín, B. Ruiz-Granados, L. Salvati, M. Sandri, M. Savelainen, D. Scott, E. P. S. Shellard, M. Shiraishi, C. Sirignano, G. Sirri, L. D. Spencer, R. Sunyaev, A. S. Suur-Uski, J. A. Tauber, D. Tavagnacco, M. Tenti, L. Terenzi, L. Toffolatti, M. Tomasi, T. Trombetti, J. Valiviita, B. Van Tent, L. Vibert, P. Vielva, F. Villa, N. Vittorio, B. D. Wandelt, I. K. Wehus, M. White, S. D. M. White, A. Zacchei, and A. Zonca. Planck 2018 results. I. Overview and the cosmological legacy of Planck. *A.&Ap.*, 641:A1, September 2020.

[49] Planck Collaboration, N. Aghanim, Y. Akrami, M. Ashdown, J. Aumont, C. Baccigalupi, M. Ballardini, A. J. Banday, R. B. Barreiro, N. Bartolo, S. Basak, R. Battye, K. Benabed, J. P. Bernard, M. Bersanelli, P. Bielewicz, J. J. Bock, J. R. Bond, J. Borrill, F. R. Bouchet, F. Boulanger, M. Bucher, C. Burigana, R. C. Butler, E. Calabrese, J. F. Cardoso, J. Carron, A. Challinor, H. C. Chiang, J. Chluba, L. P. L. Colombo, C. Combet, D. Contreras, B. P. Crill, F. Cuttaia, P. de Bernardis, G. de Zotti, J. Delabrouille, J. M. Delouis, E. Di Valentino, J. M. Diego, O. Doré, M. Douspis, A. Ducout, X. Dupac, S. Dusini, G. Efstathiou, F. Elsner, T. A. Enßlin, H. K. Eriksen, Y. Fantaye, M. Farhang, J. Fergusson, R. Fernandez-Cobos, F. Finelli, F. Forastieri, M. Frailis, A. A. Fraisse, E. Franceschi, A. Frolov, S. Galeotta, S. Galli, K. Ganga, R. T. Génova-Santos, M. Gerbino, T. Ghosh, J. González-Nuevo, K. M. Górski, S. Gratton, A. Gruppuso, J. E. Gudmundsson, J. Hamann, W. Handley, F. K. Hansen, D. Herranz, S. R. Hildebrandt, E. Hivon, Z. Huang, A. H. Jaffe, W. C. Jones, A. Karakci, E. Keihänen, R. Keskitalo, K. Kiiveri, J. Kim, T. S. Kisner, L. Knox, N. Krachmalnicoff, M. Kunz, H. Kurki-Suonio, G. Lagache, J. M. Lamarre,

A. Lasenby, M. Lattanzi, C. R. Lawrence, M. Le Jeune, P. Lemos, J. Lesgourgues, F. Levrier, A. Lewis, M. Liguori, P. B. Lilje, M. Lilley, V. Lindholm, M. López-Caniego, P. M. Lubin, Y. Z. Ma, J. F. Macías-Pérez, G. Maggio, D. Maino, N. Mandolesi, A. Mangilli, A. Marcos-Caballero, M. Maris, P. G. Martin, M. Martinelli, E. Martínez-González, S. Matarrese, N. Mauri, J. D. McEwen, P. R. Meinhold, A. Melchiorri, A. Mennella, M. Migliaccio, M. Millea, S. Mitra, M. A. Miville-Deschênes, D. Molinari, L. Montier, G. Morgante, A. Moss, P. Natoli, H. U. Nørgaard-Nielsen, L. Pagano, D. Paoletti, B. Partridge, G. Patanchon, H. V. Peiris, F. Perrotta, V. Pettorino, F. Piacentini, L. Polastri, G. Polenta, J. L. Puget, J. P. Rachen, M. Reinecke, M. Remazeilles, A. Renzi, G. Rocha, C. Rosset, G. Roudier, J. A. Rubiño-Martín, B. Ruiz-Granados, L. Salvati, M. Sandri, M. Savelainen, D. Scott, E. P. S. Shellard, C. Sirignano, G. Sirri, L. D. Spencer, R. Sunyaev, A. S. Suur-Uski, J. A. Tauber, D. Tavagnacco, M. Tenti, L. Toffolatti, M. Tomasi, T. Trombetti, L. Valenziano, J. Valiviita, B. Van Tent, L. Vibert, P. Vielva, F. Villa, N. Vittorio, B. D. Wandelt, I. K. Wehus, M. White, S. D. M. White, A. Zacchei, and A. Zonca. Planck 2018 results. VI. Cosmological parameters. *A.&Ap.*, 641:A6, September 2020.

[50] Jamie Portsmouth. Analysis of the Kamionkowski-Loeb method of reducing cosmic variance with CMB polarization. *Phys. Rev. D*, 70(6):063504, Sep 2004.

[51] Srinivasan Raghunathan, Nathan Whitehorn, Marcelo A. Alvarez, Han Aung, Nicholas Battaglia, Gilbert P. Holder, Daisuke Nagai, Elena Pierpaoli, Christian L. Reichardt, and Joaquin D. Vieira. Constraining Cluster Virialization Mechanism and Cosmology Using Thermal-SZ-selected Clusters from Future CMB Surveys. *ApJ*, 926(2):172, February 2022.

[52] Elsa P. R. G. Ramos, António J. C. da Silva, and Guo-Chin Liu. Cosmic Microwave Background Induced Polarization from Single Scattering by Clusters of Galaxies and Filaments. *ApJ*, 757(1):44, September 2012.

[53] Adam G. Riess, Alexei V. Filippenko, Peter Challis, Alejandro Clocchiatti, Alan Diercks, Peter M. Garnavich, Ron L. Gilliland, Craig J. Hogan, Saurabh Jha, Robert P. Kirshner, B. Leibundgut, M. M. Phillips, David Reiss, Brian P. Schmidt, Robert A. Schommer, R. Chris Smith, J. Spyromilio, Christopher Stubbs, Nicholas B. Suntzeff, and John Tonry. Observational Evidence from Supernovae for an Accelerating Universe and a Cosmological Constant. *AJ*, 116(3):1009–1038, September 1998.

[54] R. K. Sachs and A. M. Wolfe. Perturbations of a Cosmological Model and Angular Variations of the Microwave Background. *ApJ*, 147:73, January 1967.

[55] S. Y. Sazonov and R. A. Sunyaev. Microwave polarization in the direction of galaxy clusters induced by the CMB quadrupole anisotropy. *MNRAS*, 310(3):765–772, December 1999.

[56] Brian P. Schmidt, Nicholas B. Suntzeff, M. M. Phillips, Robert A. Schommer, Alejandro Clocchiatti, Robert P. Kirshner, Peter Garnavich, Peter Challis, B. Leibundgut, J. Spyromilio, Adam G. Riess, Alexei V. Filippenko, Mario Hamuy, R. Chris Smith, Craig Hogan, Christopher Stubbs, Alan Diercks, David Reiss, Ron Gilliland, John Tonry, José Maza, A. Dressler, J. Walsh,

and R. Ciardullo. The High-Z Supernova Search: Measuring Cosmic Deceleration and Global Curvature of the Universe Using Type IA Supernovae. *ApJ*, 507(1):46–63, November 1998.

[57] D. M. Scolnic, D. O. Jones, A. Rest, Y. C. Pan, R. Chornock, R. J. Foley, M. E. Huber, R. Kessler, G. Narayan, A. G. Riess, S. Rodney, E. Berger, D. J. Brout, P. J. Challis, M. Drout, D. Finkbeiner, R. Lunnan, R. P. Kirshner, N. E. Sanders, E. Schlafly, S. Smartt, C. W. Stubbs, J. Tonry, W. M. Wood-Vasey, M. Foley, J. Hand, E. Johnson, W. S. Burgett, K. C. Chambers, P. W. Draper, K. W. Hodapp, N. Kaiser, R. P. Kudritzki, E. A. Magnier, N. Metcalfe, F. Bresolin, E. Gall, R. Kotak, M. McCrum, and K. W. Smith. The Complete Light-curve Sample of Spectroscopically Confirmed SNe Ia from Pan-STARRS1 and Cosmological Constraints from the Combined Pantheon Sample. *ApJ*, 859(2):101, June 2018.

[58] Naoki Seto and Elena Pierpaoli. Probing the Largest Scale Structure in the Universe with Polarization Map of Galaxy Clusters. *Phys. Rev. Lett.*, 95(10):101302, September 2005.

[59] Naoki Seto and Misao Sasaki. Polarization signal of distant clusters and reconstruction of primordial potential fluctuations. *Phys. Rev. D*, 62(12):123004, December 2000.

[60] S. M. Simon, J. A. Beall, N. F. Cothard, S. M. Duff, P. A. Gallardo, S. P. Ho, J. Hubmayr, B. J. Koopman, J. J. McMahon, F. Nati, M. D. Niemack, S. T. Staggs, E. M. Vavagiakis, and E. J. Wollack. The Advanced ACTPol 27/39 GHz Array. *Journal of Low Temperature Physics*, 193(5-6):1041–1047, December 2018.

[61] Ben Thorne, Jo Dunkley, David Alonso, Maximilian H. Abitbol, Josquin Errard, J. Colin Hill, Brian Keating, Grant Teply, and Edward J. Wollack. Removal of Galactic foregrounds for the Simons Observatory primordial gravitational wave search. *arXiv e-prints*, page arXiv:1905.08888, May 2019.

[62] David H. Weinberg, Michael J. Mortonson, Daniel J. Eisenstein, Christopher Hirata, Adam G. Riess, and Eduardo Rozo. Observational probes of cosmic acceleration. *Physics Report*, 530(2):87–255, September 2013.